行政院國家科學委員會專題研究計畫　成果報告

兼具偵測多波段紅外線及可見光的偵測器陣列模組之研發

(3/3)

計畫類別：個別型計畫
計畫編號：NSC93-2215-E-002-002-
執行期間：93 年 08 月 01 日至 94 年 07 月 31 日
執行單位：國立臺灣大學電子工程學研究所

計畫主持人：管傑雄

計畫參與人員：盧仁祥

報告類型：完整報告
報告附件：出席國際會議研究心得報告及發表論文
處理方式：本計畫可公開查詢

中　華　民　國 94 年 10 月 25 日

行政院國家科學委員會補助專題研究計畫 ■ 成 果 報 告
□期中進度報告

兼具偵測多波段紅外線及可見光的偵測器陣列模組之研發(3/3)

計畫類別：■ 個別型計畫　　□ 整合型計畫
計畫編號：NSC 93－2215－E －002－002－
執行期間：2004 年 08 月 01 日至 2005 年 07 月 31 日

計畫主持人：管傑雄
共同主持人：
計畫參與人員： 盧仁祥，蕭學鈞，黃逵謙，謝寬洲，吳坤政

成果報告類型(依經費核定清單規定繳交)：□精簡報告　■完整報告

本成果報告包括以下應繳交之附件：
□赴國外出差或研習心得報告一份
□赴大陸地區出差或研習心得報告一份
■出席國際學術會議心得報告及發表之論文各一份
□國際合作研究計畫國外研究報告書一份

處理方式：除產學合作研究計畫、提升產業技術及人才培育研究計畫、
列管計畫及下列情形者外，得立即公開查詢
■涉及專利或其他智慧財產權，□一年■二年後可公開查詢

執行單位： 台大電子所

中　華　民　國　2005　年　09　月　28　日

目錄

摘要 III

Abstract IV

一、計畫內容 1

1. Quantum Well Infrared Photodetector with V-groove Structure for Normal Incident Light Coupling 1

A. 前言 1

B. 研究方法 2

1. Coupling Efficiency Estimation 2

2. Anisotropic Wet Etching 6

C. 結果與討論 7

D. 結論與計畫自評 11

E. 參考文獻 11

2. Superlattice Infrared Photodetector and 1-D Detector Array 13

A. 前言 13

B. 研究方法 13

1. Fabrication Process of the Single Photodetector 13

2. Fabrication Process of the 1-D Detector Array 16

C. 結果與討論 20

1. SLIP with Doping Density 1×10^{17} in the Superlattice 20

2. SLIP with Doping Density 5×10^{16} in the Superlattice 27

3. Comparison of Sample A and Sample B 27

4. 1-D Detector Array 34
5. Comparison of Single Device and 1-D Detector Array 35

D. 結論與計畫自評 44

E. 參考文獻 44

3. Superlattice Infrared Photodetector with Grating Structure for Normal Incident Light Coupling 46

A. 前言 46

B. 研究方法 47

C. 結果與討論 50

1. Sample with 45-degree facet coupling 50
2. Samples with grating structure 51
3. Discussion 56

D. 結論與計畫自評 63

E. 參考文獻 63

二、參考文獻 63

三、計畫自評 63

摘要

紅外線在日常生活方面的應用越來越廣泛，包含了國防，天文，環保以及醫療等等。而現今世界各國都有許多公司與研究機構開始發展焦平面陣列的紅外線偵測器，以期能達到較大面積與較準確的應用。但量子井或超晶格紅外線偵測器因為受到電子躍遷的選擇律的限制，需要一個與長晶方向相同的電場來達成激發電子的目的，所以並不能吸收正向入射的光線。一般在做單顆元件的特性量測時，我們可以在樣品的側邊磨四十五度斜角，讓光線從斜面入射，使得紅外線有垂直方向的電場。但在大型的焦平面陣列，並不能利用此一概念，而需要其他的方式讓紅外線可以經由正向的入射來達成偵測的效果。在此計畫中，我們提出了數種方式，分別是 V 型谷結構來達成耦合垂直入射光的目標，並進而開發此結構的一維線性陣列，以及利用金屬層上的週期性排列的孔洞，達成正向入射的目的。

運用非等向性化學蝕刻在量子井偵測器上製作 V 型谷結構，可以耦合垂直入射之光線。我們利用幾何光學來估計具 V 型谷結構之量子井偵測器耦合垂直入射光的效率；並提出一套製作程序，用來製作具 V 型谷結構之量子井偵測器。由光電流響應的量測顯示，V 型谷結構耦合垂直入射光的能力可大致等效於 45° 角斜面角 TM 模式的入射。

若要將其應用在紅外線熱影像時，此偵測器除了要有較高的背景限制效率溫度之外，還必須以一維或二維的大型焦平面陣列來取代單一的偵測器元件。我們也介紹了一維偵測器陣列的製程步驟，將元件做成陣列的型式。實驗結果顯示雖然此一維偵測器陣列的響應峰值較單一偵測器元件要來的小，但是由於其暗電流也比單一偵測器元件要小的多，所以其偵測度反而比單一元件要來的好。由結果顯示，我們可以藉由增加環狀金屬的接觸面積，以及增加 V 型凹槽的傾斜角度，來提高偵測器陣列的響應度。在製做一維偵測器陣列時，此製程步驟是一項不錯的選擇。

在元件製程上，我們也可以在樣品表面設計一具有週期性結構的金屬孔洞，以類似光子晶體的概念，形成另類的光柵，而使得此偵測器可以達到頂面正向入射的目的，以避免底面入射必須磨薄的製程。

我們製作了三種不同週期的光柵結構，而光線由正面入射。我們可以利用各種不同週期的光柵結構來調變響應的波形。這是因為響應的波形會受到表面電漿共振的影響。而表面電漿共振的頻率可以用光柵的週期來控制。在本篇論文中，我們成功地利用光柵結構製作出可以正向入射的紅外線偵測器，而且響應的波形可以利用表面電將共振來調變。

關鍵詞：量子井紅外線偵測器，超晶格紅外線偵測器，線性陣列，正向入射光耦合，金屬條狀光柵

Abstract

Infrared detection has been used widely as the applications in military services, astronomy, environmental monitoring and medicine. In recent years, many companies and research institutes focused on the development of the infrared detector's focal plane array to achieve the large area and more accurate detection applications. For quantum well or superlattice infrared photodetector, because of the selection rule, the photodetector does not absorb radiation incident normal to the surface since the light polarization must have an electric field component parallel to the growth direction. In general, the single photodetector device has to be illuminated through a 45° polished facet. However, this illumination scheme limits the configuration of the detectors to linear array or large focal plane array. For imaging, it is necessary to be able to couple light uniformly to two-dimensional arrays of these detectors. In this paper, we will present several methods to achieve the goal of coupling the normal incident light, such as the photodetectors with V-groove structure for normal incident light coupling. Moreover, we fabricate the one-dimension linear array based on this structure. Besides, the periodic metal hole array is designed on the sample surface. This structure can act as the grating and make the detector achieve the goal of normal incidence.

V-groove structure can be fabricated on the QWIP by using anisotropic etching to couple the normally incident light. In this paper, the efficiency for the QWIPs with V-groove structure to couple the normally incident light is estimated by applying the ray optics. A feasible processing procedure for fabricating the V-groove structure is proposed. The responsivity measurement shows that the V-groove structure can couple the normal incident light with the same efficiency as the TM mode light incident into the 45° edge facet of the photodetector.

For thermal imaging application, the detectors must have high background limited performance temperature T_{BLIP} and 1-D or 2-D (Focal Plane) detector arrays have been used instead of the single detector. The process of the linear array fabrication is also introduced. The experimental results show that the response of the detector array is smaller than single device, but the dark current of detector array is much smaller than single device. It leads to the larger detectivity of detector array. By increasing the contact area of metal ring and tilted angle of V-grooves for larger responsivity, it will be a new method to fabricate 1-D detector array.

For device fabrication, we can design a metal hole array with periodicity on the sample surface. Analogous to the concept of photonic crystal, the metal hole array can act as the grating and make the detector achieve the goal of normal incidence. The traditional fabrication of detector with normal incidence is to thin down the substrate.

Using this new structure, we can omit the thin-down process.

We fabricate three devices with different period of gratings for topside-illumination. Base on this structure, the photoresponse of each spectral shape is tunable by the period of gratings. The response shape is affected by surface plasmon. The plasmon peak can be selected by period of gratings. In summary, the experimental results confirm the applicability of SLIPs with grating structure for coupling the normal incident light and tunable response shape by surface plasmon.

Keywords：quantum well infrared photodetector, superlattice infrared photodetector, linear array, normal incident light coupling, metal strip grating

一、計畫內容

1. Quantum Well Infrared Photodetector with V-groove Structure for Normal Incident Light Coupling

A. 前言

Quantum well infrared photodetectors (QWIPs) based on intersubband transition have been undergoing rapid development during the past several years. Infrared detectors made of $GaAs/Al_xGa_{1-x}As$ quantum well may be a potential alternative to those based on HgCdTe material system because of the relative maturity of GaAs-related materials and their processing technology [1,2]. For most detector applications, normally incident radiation absorption is required for convenience. However, due to the isotropic effective mass of the active Γ electrons, the QWIP detector can only absorb light with the electric field perpendicular to the multiple quantum well layers [3,4,5]. In order to couple the normal incident radiation, much work has been done, such as two-dimensional grating, and random scattering couplers. Recently, a coupling scheme based on total internal reflection (TIR) instead of diffraction was proposed by C.J. Chen et al [6,7,8]. Referring to Fig. 1, this coupling scheme utilizes an array of QWIP wires with slant sidewalls to reflect the normally incident light. These QWIP wires are created by etching V-grooves through the detector active region to the bottom contact. In the ideal case showed in Fig. 1, the reflected light will propagate parallel to the MQW layers, and hence half of the photons can be absorbed for unpolarized light. Besides, the light can also be illuminated from the topside of the sample. On this condition, the light is coupled into the QWIP by refraction as shown in Fig. 2 instead of TIR.

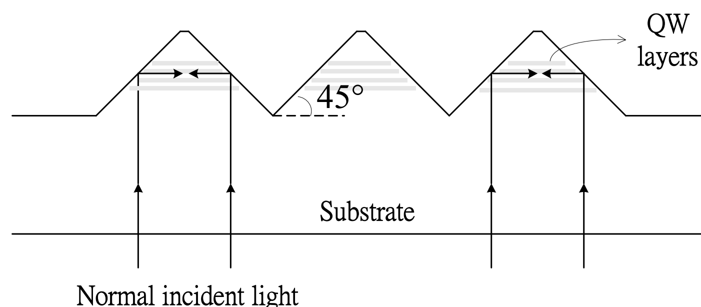

Fig. 1 Optical path for back-illuminated light.

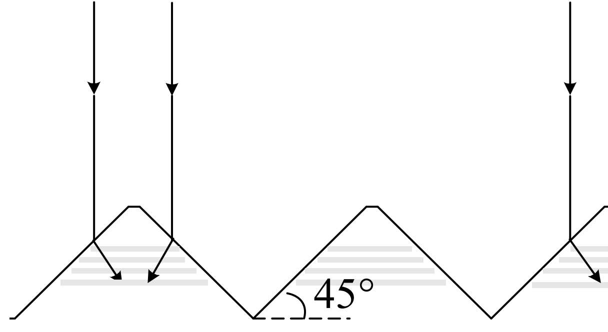

Fig. 2 Optical path for top-illuminated light.

Our work is to develop a method to estimate the coupling efficiency of V-groove structure and try to find the associated affecting factors. The processing steps to fabricate a QWIP with V-grooves are also proposed in this work for practical test. The responsivities of the QWIP with V-grooves are measured and compared with experimental results based on traditional edge coupling scheme. The IR absorpton spectrum and spectral response are also measured for comparison.

B. 研究方法

1. Coupling Efficiency Estimation

In this section, the responsivity of a QWIP with V-grooves is estimated and used as an index to evaluate the V-groove coupling scheme. The responsivity R of a detector, is defined as the ratio of the photocurrent I_p over the optical power P_i transmitted into the detector, i.e.

$$R \equiv \frac{I_p}{P_i} = \eta_d \frac{e}{h\nu} g \quad (1)$$

where $h\nu$ is the photon energy, g is the photoconductive gain, and η_d is the quantum efficiency of the detector [9]. Among them, η_d is defined as average number of optical transitions per photon incident into the sample, and is given by

$$\eta_d = \frac{1}{2}\frac{A_c}{A} M(1-R)[1-\exp(-\frac{e^2\hbar f_Q N_d W}{n_w \varepsilon_0 m^* c\Gamma} sN\sin^2\theta)], \quad (2)$$

where A is the area of the detector, A_c is the effective coupling area, M is the material removal factor, R is the reflection coefficient of the detector surface, s is the times that a photon passes the detector, N is the number of periods in a MQW structure, f_Q is the oscillator strength, N_d is the doping density in the well, θ is the angle of incidence, W is the width of the well, n_w and m^* are the refractive index and the effective mass of

the well respectively, and Γ is the absorption linewidth [1]. The term (1/2) is used to count in the fact that only the component with the TM polarization can be absorbed for the unpolarized light. During fabricating a QWIP with V-grooves, some part of the MQW is removed by wet etching. The removal of material will affect the responsivity of the detector. Therefore, a parameter M is used to count in this effect.

In order to evaluate the coupling efficiency of V-groove coupling scheme, the edge coupling scheme that couples the incident light through a 45° facet on the edge of the substrate is introduced first. The infrared light is back-illuminated onto the detector through the facet as illustrated in Fig. 3. Although the edge coupling is not useful for practical applications, it is still a standard to evaluate a QWIP's intrinsic performance by virtue of the simple processing steps and the readily known light intensity inside the sample. It can also be a standard to evaluate another coupling scheme by comparing its responsivity with that of the edge coupling [1]. For convenience, a quantity named responsivity ratio (abbreviated as R ratio) is defined as

$$\text{R ratio} = \frac{\eta_d \text{of a coupling scheme}}{\eta_d \text{of edge coupling scheme}}. \quad (3)$$

The R ratio is the figure of merit of a particular coupling scheme and is independent on the quantum well parameters [1].

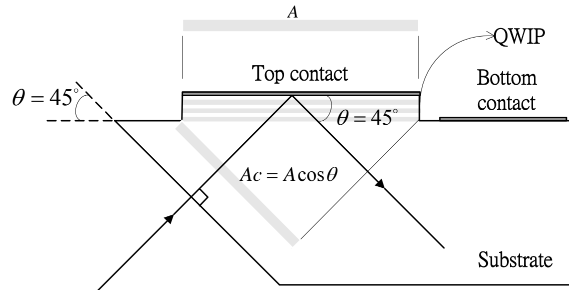

Fig. 3 The light incident geometry under 45° edge coupling. The light passes the QWIP two times.

With the definition of R ratio, the coupling efficiency of V-groove structure can be easily evaluated. All we need to do is plotting the optical path and substituting all related parameters into Eqs. (2) and (3) to calculate the R ratio. Since the light can be illuminated from backside or topside of the sample, we will discuss both conditions respectively.

When the light is back-illuminated onto a QWIP with V-grooves, the light is

coupled by the total internal reflection on the slant sidewall as shown in Fig. 4. The slope of the sidewall generated by wet etching is about 54° instead of 45° [10]. The light passes the detector by two times just the same as the edge coupling scheme. It is noted that the effective area A_c to couple the normal incident light is restricted by the area of sidewalls and varies with the geometry of the detector. The angle of incidence for TIR coupling scheme is 72° which is larger than 45° for the edge coupling scheme.

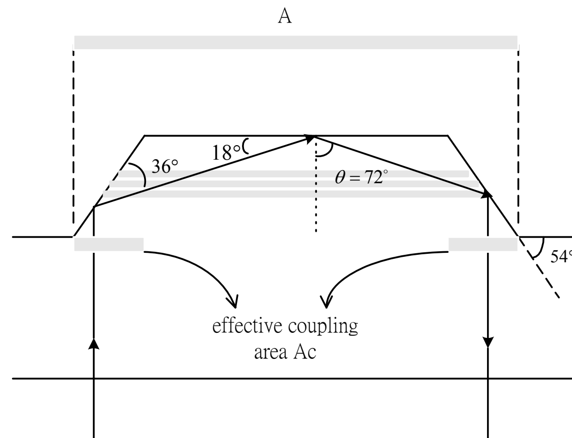

Fig. 4 The optical path for the TIR coupling scheme in the V-groove structure.

One may wish to reduce the width of QWIP wires in order to increase the number wires and hence the effective coupling area in a single detector pixel. When the sidewall separation is sufficiently narrowed, the optical path of the incident light will be different as shown in Fig. 5. This should be considered when designing the detector.

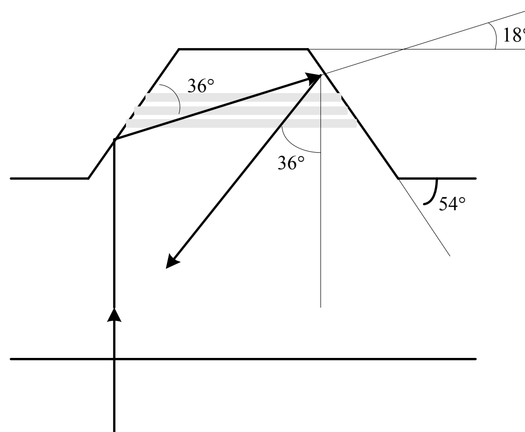

Fig.5 The optical path of TIR coupling scheme when the width of the QWIP wires are sufficiently narrowed.

The top-illuminated situation is considered now. Referring to Fig. 6, 90% of the incident photon (TM mode) will pass through the air-GaAs interface and turns into a new direction by the refraction effect. The remaining 10% of photons are reflected and have 75% opportunity to enter the QWIP through another interface. We can calculate the R ratio easily as for the backside-illumination case. The R ratio for this condition is expected to be smaller than that in the backside-illumination case

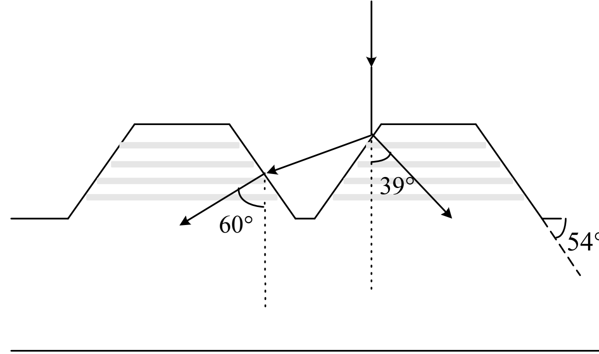

Fig. 6 The optical path when the light is incident from the topside of the QWIP with V-grooves.

To evaluate the efficiency and feasibility of the V-groove coupling scheme, we calculate the R ratio for a series of QWIPs with different number of V-grooves. The parameters of the MQW structure are assumed as N_d=1.2x10^{18}cm^{-3}, well width W=50 angstroms, oscillator strength f_Q=1, number of wells N=30, and absorption linewidth Γ=20 meV. For a given QWIP, we calculated R ratio vs. the number of V-grooves within the QWIP. The result is shown in Fig. 7. For sufficiently large number of V-grooves, the R ratio is greater than one. The R ratio on top-illuminated condition is given in Fig. 8. As expected, the R ratio on this condition is less than that on the back-illuminated condition.

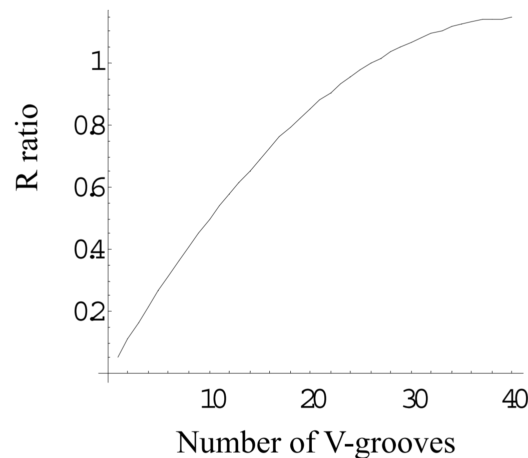

Fig. 7 The estimated value of R ratio versus the number of V-grooves in a QWIP for

the back-illuminated condition.

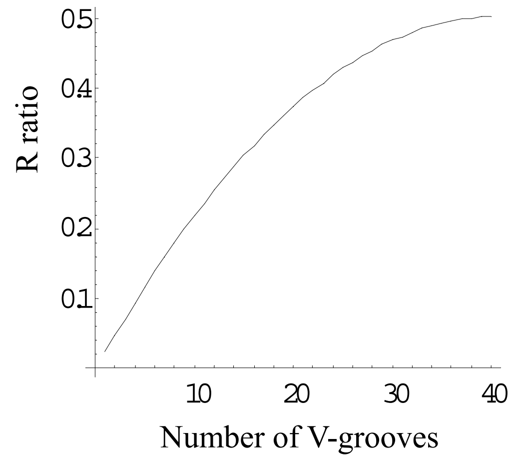

Fig. 8 The estimated value of R ratio versus the number of V-grooves in a QWIP for the top-illuminated condition.

2. Anisotropic Wet Etching

For anisotropic wet etching process, the slowest etching planes dictate the final shape of the etched profile. The [111] Ga planes therefore dominate the profile since the etching rate on [111] Ga is the slowest for most reaction-limited etchants. The etched profile generated by anisotropic etching is shown in Fig. 9. Typical reaction-rate-limited etchants yield outward sloping edges along $[01\bar{1}]$ direction and inward sloping edges, i.e. trenching effect, along [011] direction. As the microscopic photographs shown in Fig. 10, the QWIP wires parallel $[01\bar{1}]$ direction yield a perfect V-groove, while the wires parallel [011] direction almost disappeared due to the severe trenching effect. Thus, the wires on our mask should parallel $[01\bar{1}]$ direction to ensure the correct profile when fabricating the QWIP. On the other hand, the selection of the etchants is also important because the etching rate and angle of sidewall vary with etchants. After many tests on various etchants, the NH_4OH-H_2O_2-H_2O (3:1:50) etchant is selected to fabricate the QWIPs with V-grooves because it has proper etching rate and yields a proper slope of sidewall, about 50° .

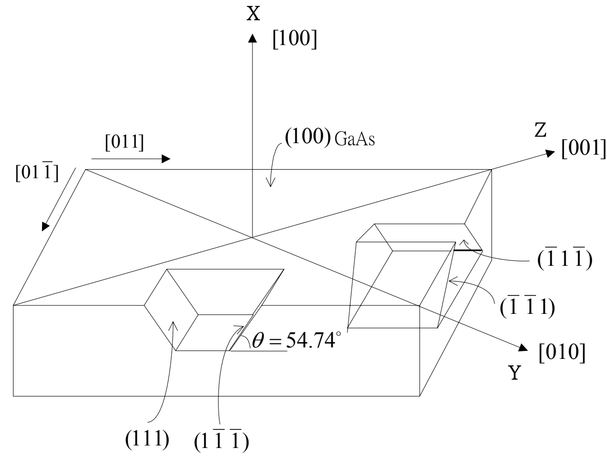

Fig. 9 The GaAs (100) wafer cleaved along $(01\bar{1})$ and (011) planes normal to the (100) surface. The etchants that etch the [111] Ga type planes as the slowest rates would yield anisotropic etch profile as shown.

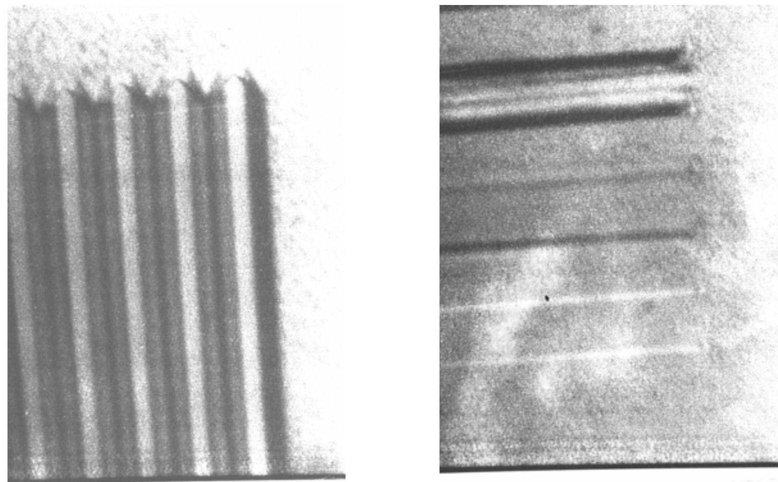

Fig. 10 The profile produced by the anisotropic etching process. The wires in the left photograph are parellel to the $[01\bar{1}]$ direction and those in the right photograph are parallel to [011] direction.

C. 結果與討論

The MQW used in our experiment consists of 30 periods of GaAs quantum wells and $Al_{0.25}Ga_{0.75}As$ barriers. The well width and the barrier width are 50 angstroms and 800 angstroms respectively. The doping density N_d is 1.2x10^{18} cm^{-3} in the wells and 1.5x10^{18} cm^{-3} in the contact layers. Its detection peak λp is supposed to be 8.7

μm. Using this QW structure, a QWIP with V-grooves is fabricated to verify the expectation aforementioned. The 3-dimensional perspective of the device is shown in Fig. 11. This perspective is just for illustration, so the number of wires and distance between wires is different to the real device. The dimensions of real device are given in Fig. 12. Besides, the scanning electron microscopy (SEM) photographs are shown in Fig. 13 and Fig.14. The estimated R ratios of this QWIP for back-illuminated and top-illuminated case are 0.68 and 0.40 respectively.

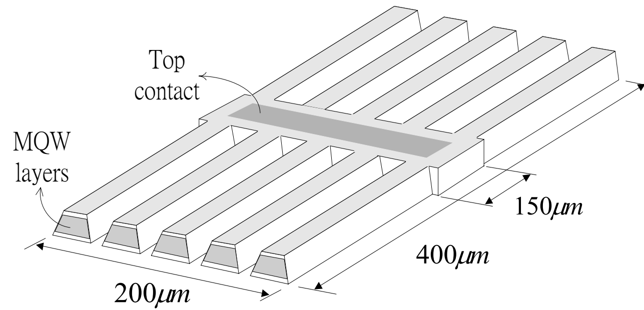

Fig. 11 3-dimensional perspective of the QWIP with V-grooves.

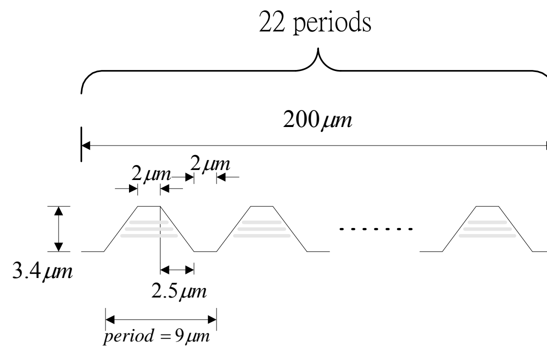

Fig.12 Dimension of the QWIP with V-groove structure.

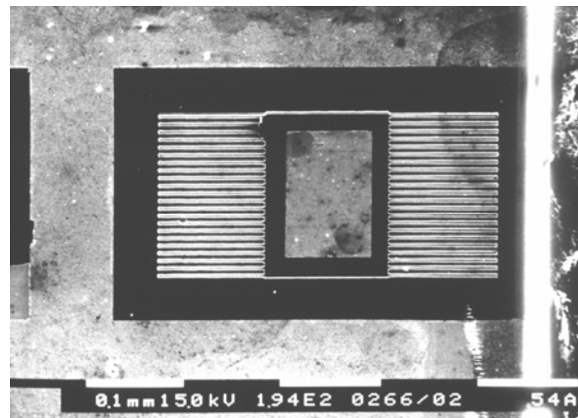

Fig. 13 SEM photograph of the QWIP with V-groove structure.

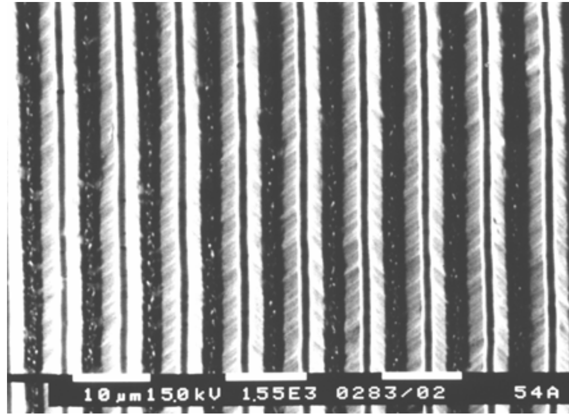

Fig. 14 SEM photograph the V-groove structure in our QWIP. The distance between each QWIP wires is 9 μm

To evaluate the V-groove coupling scheme, the responsivity of QWIP with 45° edge coupling scheme was firstly measured at various temperature and bias conditions. The structure of this QWIP is only a plane mesa without any V-grooves. The measured responsivity was shown in Fig. 15. Then, the QWIPs with V-grooves were measured for comparison. The QWIPs were illuminated by blackbody radiation from either backside and topside of the sample.

The responsivity with infrared radiation incident from backside of the sample was shown in Fig. 16. The responsivity is greater than 60% of that measured with 45° edge coupling scheme through the whole bias range. The results agree with our estimation in section 2. Fig. 17 shows the responsivity with infrared radiation incident from the topside of the sample. It is also greater than 60% of that measured with 45° edge coupling scheme through the whole bias range. The applicability of this coupling scheme is sure enough.

The responsivity ratios (R ratio) vs. bias voltage for both back-illuminated and top-illuminated condition are given in Fig. 18. The R ratio for the backside-illumination is always larger than that of the topside one. The real value of the R ratio is a little bit larger than our estimation. It may be attributed to the absorption due to the multiple reflection, which is not taken into account in our estimation. In particular, for the bias dependence, it is noted that the R ratios at low bios region increase rapidly. This may be resulted from the variation of refractive index at the low bias region since the crystal structure of GaAs is polar and the refractive index change with bias. The further study is necessary to understand the reason.

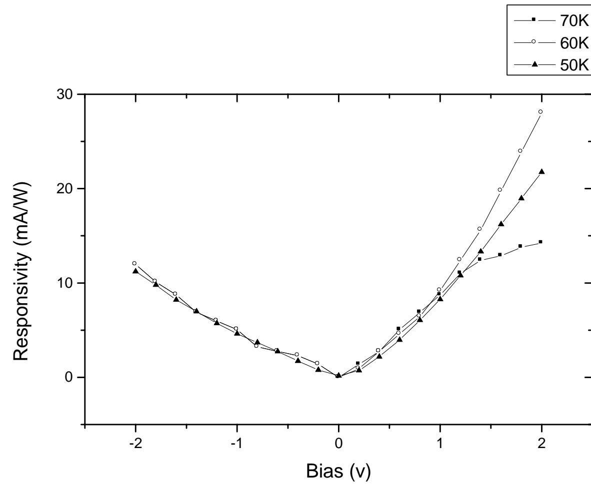

Fig. 15 Responsivity of the QWIP with edge coupling scheme.

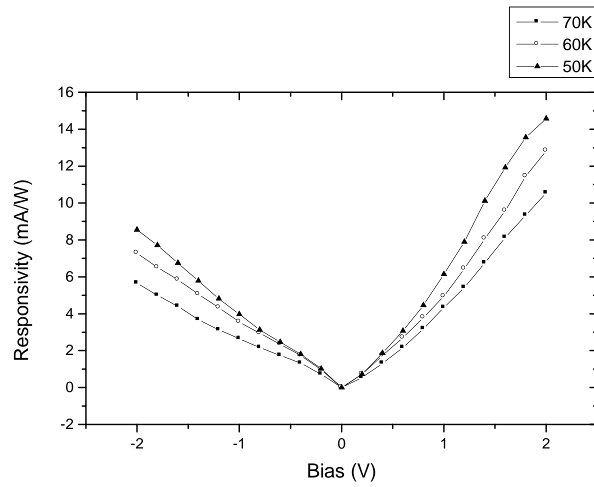

Fig. 16 Responsivity of the QWIP with V-groove on back-illuminated condition.

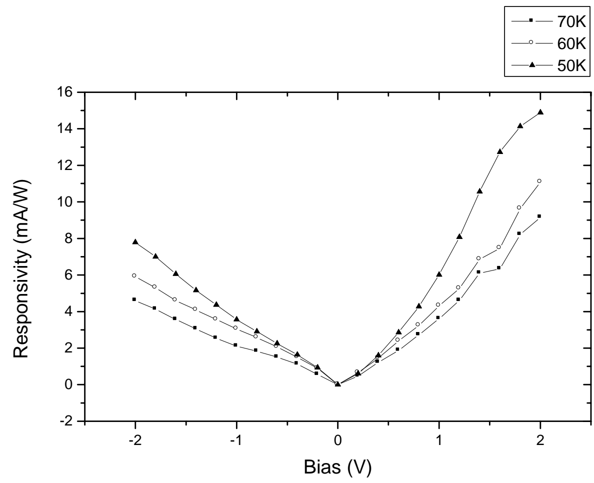

Fig. 17 Responsivity of the QWIP with V-grooves on top-illuminated condition.

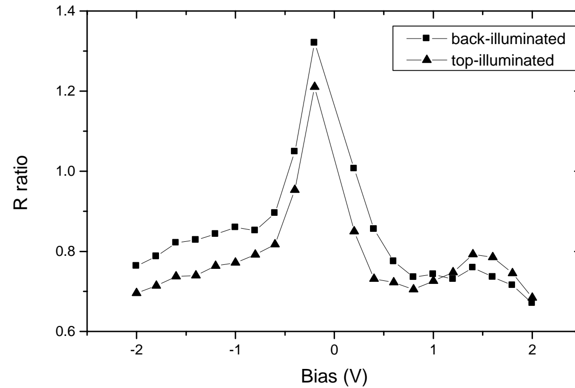

Fig. 18 Responsivity ratio (R ratio) of the QWIP with V-grooves at 50K. The R ratios on both top-illuminated and back-illuminated condition are calculated respectively.

D. 結論與計畫自評

The theoretical estimation model of the V-groove structure to couple the normally incident light with the quantum well infrared photodetector is proposed in this paper. A wet-etching process is given to fabricate the V-groove structure. The estimated R ratio is about 80% of the real value. The underestimation is attributed to the absorption due to the multiple reflection, which is not considered in our model. However, the experimental results show that the V-grooves can effectively couple the normal incident light for either backside-illumination or topside-illumination. The responsivities on both conditions are comparable to that of the QWIP with edge coupling scheme. Thus, the applicability of the V-groove coupling scheme is verified.

E. 參考文獻

[1] K.K. Choi "The Physics of Quantum Well Infrared Photodetectors ", Published by World Scientific, ISBN 9-810-22872-4, p.p. 155-167 and 189-199

[2] Shun Lien Chuang," Physics of Optoelectronic devices", Wiley Inter-science publication, p.p. 201-205 and 362-364

[3] Y. Fu, M. Willander "Optical coupling in quantum well infrared photodetector by diffraction grating" J. Appl. Phys., Vol. 84, No. 10, 1998, p.p. 5750-5755.

[4] G. Bastard and J.A. Brum "Electronic states in semiconductor heterostructures", IEEE J. Quantum electron. QE-22, 1986, p.p. 1625-1644

[5] G. Bastard "Wave Mechanics Applied to Heterostructures", Halsted, New York, 1988

[6] C.J. Chen, K.K. Choi, M.Z. Tidrow, D.C. Tsui "Corrugated quantum well Infrared photodetectors for normal incident light coupling" Appl. Phys. Lett. Vol. 68, No. 1, 1996, p.p. 1446-1448

[7] C.J. Chen, K.K. Choi, W.H. Chang, D.C. Tsui "Performance of corrugated quantum well Infrared photodetectors" Appl. Phys. Lett. Vol. 71, No. 21, 1997, p.p. 3045-3047

[8] C.J. Chen, K.K. Choi, W.H. Chang, D.C. Tsui "Corrugated Infrared hot-electron transistors" Appl. Phys. Lett. Vol. 73, No. 9, 1998, p.p. 1272-1274

[9] Jasprit Singh "Semiconductor optoelectronics physics and technology", Published by McGraw Hill, ISBN 0-07-057637-8

[10] M.J. Howes, D.V. Morgan "Gallium arsenide materials, devices, and circuits", Published by John Wiley & Sons, ISBN 0-471-90048-6

2. Superlattice Infrared Photodetector and 1-D Detector Array

A. 前言

The superlattice infrared photodetectors have drawn much attention since the observation of intersubband absorption in the far infrared region. For thermal imaging application, the detectors must have high background limited performance temperature T_{BLIP} and 1-D or 2-D (Focal Plane) detector arrays have been used instead of the single detector.

In the report, we first investigated the effect of the doping density in the superlattice. By the simple fabrication process of samples into devices, and the measurement setup, we can measure the electrical and optical properties of our devices. With comparison the characteristics of the SLIPs with high doping density ($1x10^{17}cm^{-3}$) and low doping density ($5x10^{16}cm^{-3}$), it shows that the SLIPs with low doping density has better background limited performance temperature T_{BLIP}, responsivity, quantum efficiency, and detectivity due to the decrease of the impurity scattering.

The new fabrication process of 1-D detector array is illustrated. The experimental results show that the response of the detector array is smaller than single device, but the dark current of detector array is much smaller than single device. It leads to the larger detectivity of detector array. By increasing the contact area of metal ring and tilted angle of V-grooves for larger responsivity, it will be a new method to fabricate 1-D detector array.

B. 研究方法

In order to analyze the characteristics of the photodetector, we have to make appropriate process to the device. First, we will introduce the fabrication process of single device and 1-D detector array.

1. Fabrication Process of the Single Photodetector

Figure 1 shows the flowchart of a complete process of single device [1,2,3]. Now, we go into details.

(1) Sample Cleaning

For improving the yield and reliability of the devices, the sample must be cleaned before processing. We sequentially rinse the sample in GP solution, acetone, methanol, and deionized water (DI water), each step for five minutes. After blown dry with nitrogen, the sample is then put in an oven at 90°C for one minute to bake out the mist.

(2) Lithography

Contact printing is a popular lithographic approach to GaAs device fabrication. In this technique, the sample is coated with photoresist by spin-coator. After coating, the photoresist-covered slice is baked at 90°C for five minutes in order to drive away the solvent of

the photoresist (soft- baking). Then the mask is placed in proximity to the slice for mask alignment and the photoresist is exposed by ultraviolet light. Next the slice is subjected to a development process that removes the exposed photoresist. Following step is the hard-baking which is used to further harden the photoresist and to improve adhesive force between slice and photoresist. Therefore, the pattern transfer is accomplished.

(3) Wet Etching

We use wet etching with the H_3PO_4-H_2O_2-H_2O solution system to form mesa structures for device isolation. The volume ratio of H_3PO_4-H_2O_2-H_2O is 2:1:8 and the etching rate is about 4000Å to 5000Å per minute in the room temperature. Finishing etching process, the photoresist is washed out in the acetone.

(4) Electrode Deposition and Liftoff

The pattern of metal contact is now transferred to the sample by the same lithography procedure as Step (2). Then we dip the sample in the NH_4OH: H_2O=1:10 mixed solution about 25 seconds for ousting oxide from the sample surface. Next, the metal is applied to GaAs slices by thermal evaporation, which is good for lift-off applications. The evaporated metals are 600Å alloyed Au/Ge/Ni layer and 2400Å Au layer. Then the photoresist mask is dissolved by acetone to lift away the metallic film formed on the photoresist and therefore we obtain the desired electrode configuration.

(5) Anneal

By the reason of obtaining an ohmic contact, the surface of the slice must be heated until the metalization alloys into the GaAs. As temperature rises, the AuGe alloy begins to melt and GaAs is dissolved in the melt. Thereby, the GaAs layer that merges with germanium acts as an n-type dopant which help conducting the electrons. This diffusion phenomena results in spikes between the interface of slice and metal. Nickel can act as a wetting agent for the Au-Ge, so we add nickel to the AuGe metallization to reduce balling.

(6) Polishing Facet and Bonding Wire

Due to the selection rule of intersubband transitions, the normal incident light will not affect the infrared photodetector. Hence, we make a backside-illuminated detector by polishing a 45° facet on a selective area of the fabricated device. Although the edge coupling is useful only for single detector or 1-D detector array, it is still a standard to evaluate a detector's intrinsic performance.

Fig. 2 shows an accomplished device. The detector is located on a ceramic plate to keep thermal contact well with the sample holder. The golden wire is used to connect the bottom and top contacts with the pads of the ceramic plate for measuring some electrical properties.

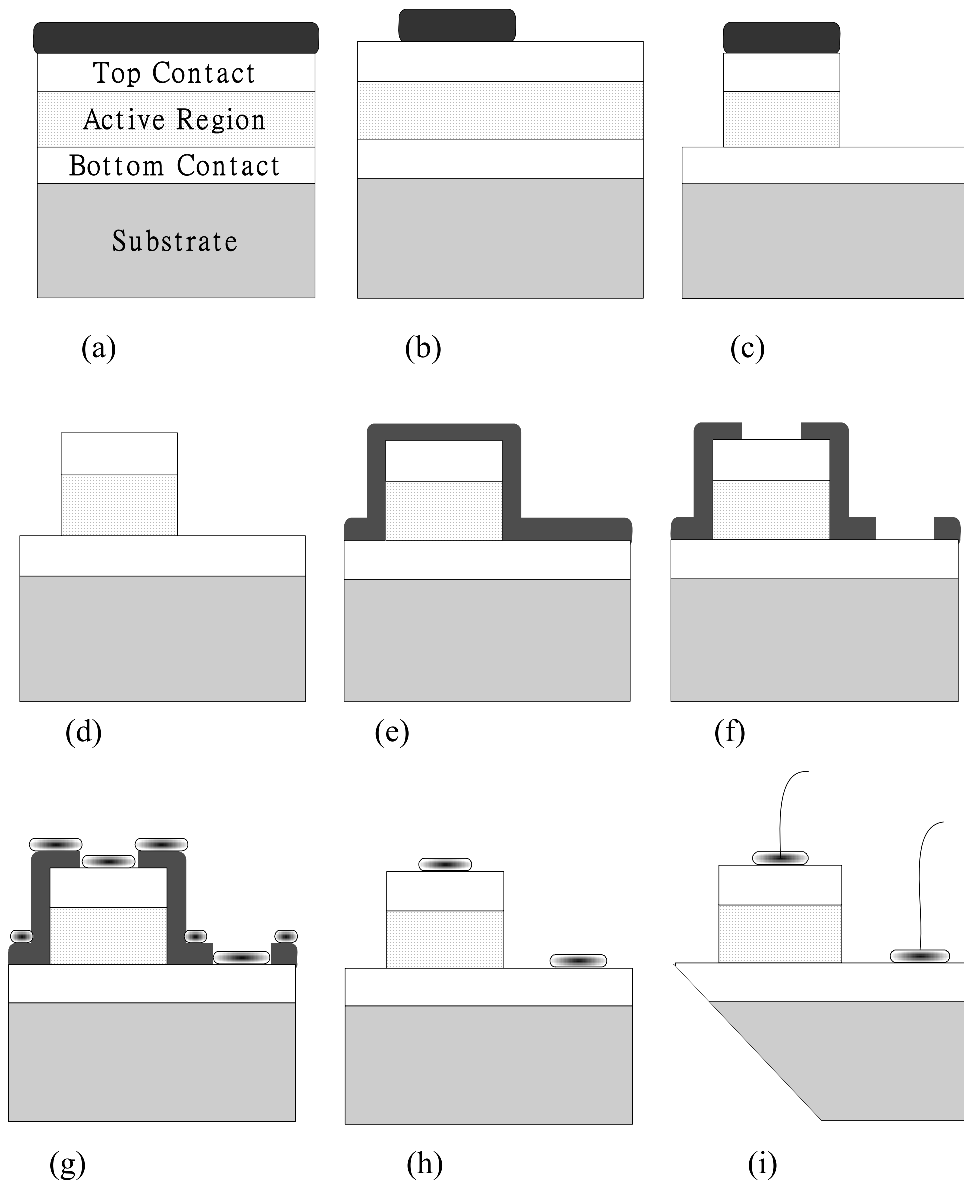

Fig. 1 The flowchart of single device fabrication : (a) first photoresist coating (b) pattern transfer by lithography (c) wet etching (d) first photoresist removal (e) second photoresist coating (f) pattern transfer by lithography (g) metal deposition by evaporation (h) lift-off (i) 45° facet polishing

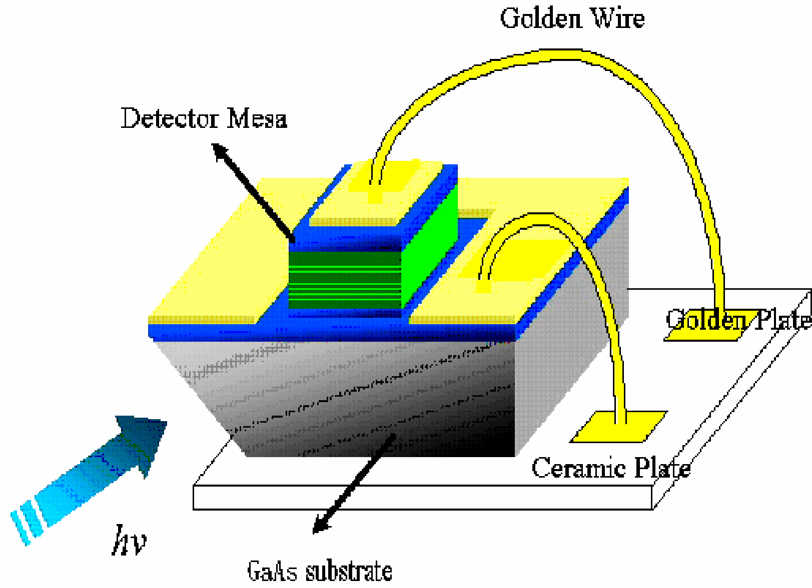

Fig. 2 The final package of the fabricated photodetector.

2. Fabrication Process of the 1-D Detector Array

As shown in Fig. 3 is the 3-D solid eyes of a 1×N linear detector array. One of the main goals of the 1-D detector array is to eliminate the crosstalk between two neighboring detection pixels with an optical isolation structure. A fabricating instance of the 1-D detector array is shown in Fig. 4 which corresponds to the vertical (AA' direction) and transverse (BB' direction) cross-section of the array bulk in Fig. 1, respectively. We will show the detail process in the following [4,5,6].

(1) Trench Etching

Refer to Fig. 4 (a), (b), we first transfer the pattern on the surface of the slice by lithography. It should be noted that the angle between the trench patterns and cleaved edge ($[01\bar{1}]$ or $[011]$) of the wafer should be 45° to ensure the V-groove coupling scheme being constructed in the later process step. We etch the photoresist-uncovered region of the slice with the H_3PO_4-H_2O_2-H_2O system. The etched region contains the mesh-like trench and the common ground region while the unetched region contains top contact region and numbers of detection pixels. The etched region must reach to the bottom contact layer, so that the electrical isolation among detection pixels can be achieved. Next, an optical isolation structure will be proposed.

(2) Optical Isolation Structure

Refer to Fig. 4 (c), an first insulating layer is deposited on the surface of the slice by sputtering silicon nitride (Si_3N_4). The insulator is used to avoid short problem between the top and bottom contact or between the detection pixels. Then, we deposit a reflecting metal layer of titanium (Ti) upon the insulator layer by sputtering. Because the insulating layer and the reflecting metal layer of several regions, such as the surface of each pixel, the top and bottom contact, have to be removed, we refill the second insulating layer of polyimide into the mesh-like trenches to protect

the region in which the insulator and metal reflector have to be preserved. Next, we utilize HF to etch the insulating layer and the reflecting metal layer of the slice except those protected by the polyimide on the trenches. Therefore, the optical isolation structure is formed by the metal-insulator-semiconductor (MIS) structure.

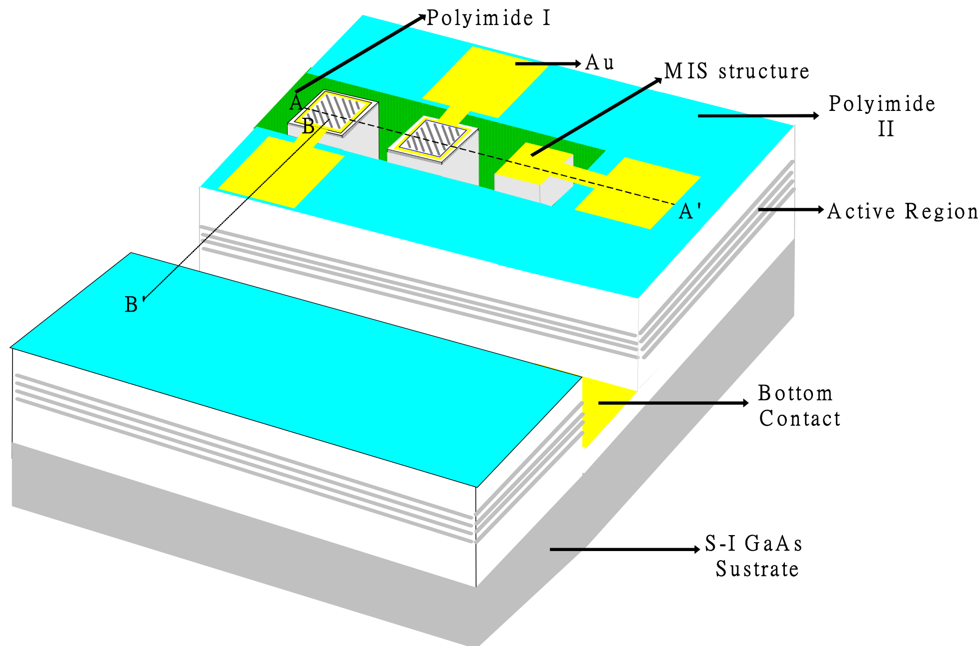

Fig. 3 The 3-D solid view of a 1×N linear detector array

(3) V-groove Couple Scheme

Refer to Fig. 4 (d), in order to couple the normal incident light, we construct several rectangular grooves on the surface of each detection pixel by anisotropically wet etching. As mentioned above, the longer side of each rectangular groove must be parallel to the $[01\bar{1}]$ direction to ensure the outward sloping structure. The etchant is composed of NH_4OH-H_2O_2-H_2O mixed with 3:1:50 volume ratio. After the etchant is prepared, one must begin the etching process immediately to avoid the etchant aging problem. That is, H_2O_2 will escape from the etchant and the composition will change.

(4) Field Passivation Layer

Refer to Fig. 4 (e), for making the metal on the top contact cross the trenches to the surface of each detection pixel, we coat the surface of the top contact with a field-passivation layer of polyimide.

(5) Electrode Deposition and Lift-off

Refer to Fig. 4 (f), the electrodes are created by the same process of single device. We deposit an alloy layer of Au/Ge/Ni and a layer of Au on the surface of the slice by evaporation. Then, the excess metal is removed by lift-off method and therefore we obtain the desired electrode configuration. Finally, the device is treated by rapid thermal annealing (RTA) to form the ohmic

contacts. The fabricated sample is then sliced into pieces of detector arrays, and is located on a ceramic plate to measure some electrical properties.

(a)

(b)

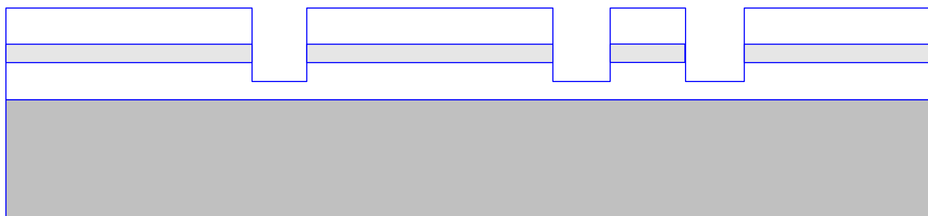

top cont

active

bottom c

S-I GaA

(c)

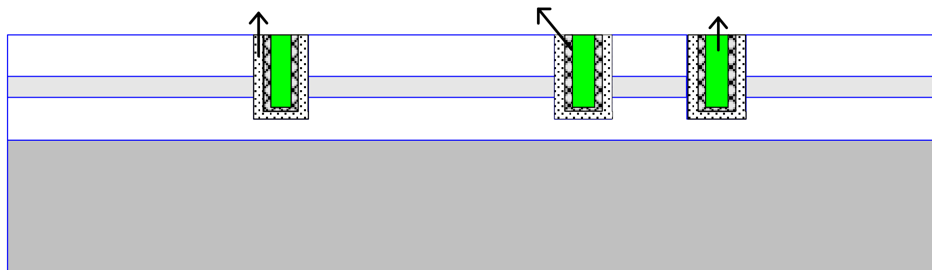

Detection

B

top contact

(d)

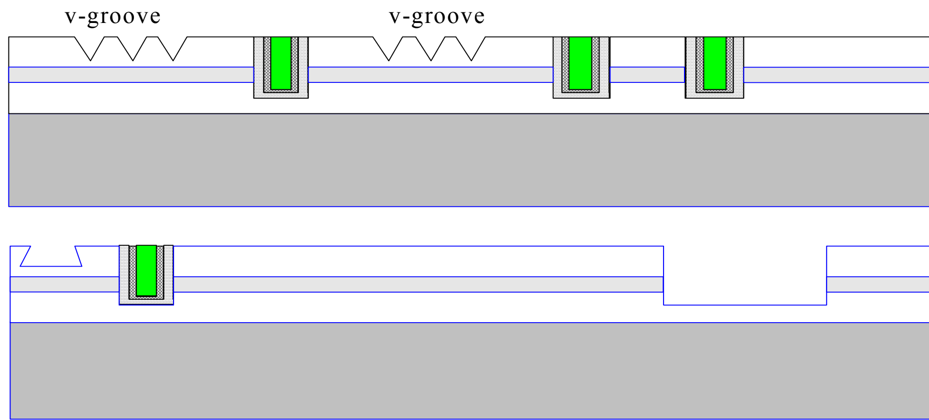

(e)

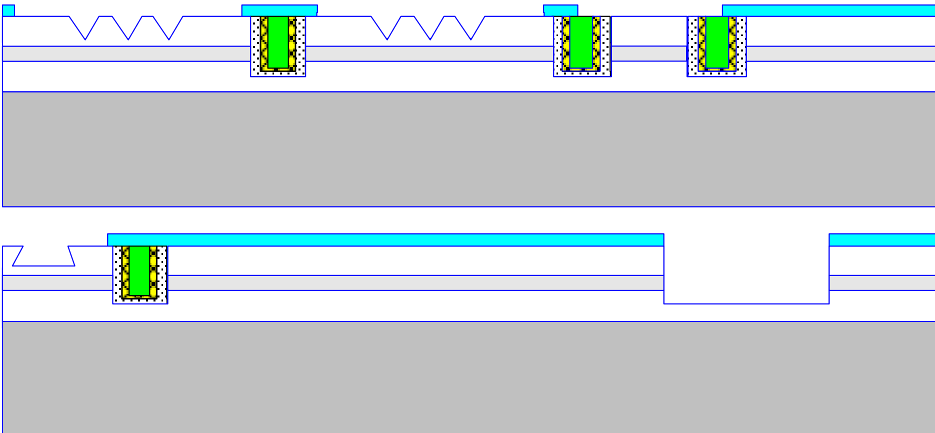

(f)

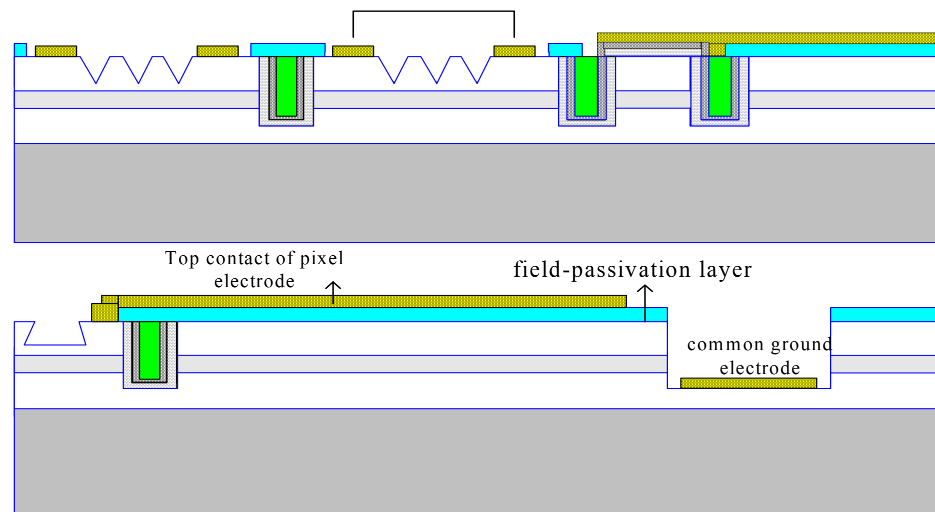

field-passivation

Fig. 4 The schematic process flow of the 1-D linear array, which corresponds to the vertical (AA' direction) and transverse (BB' direction) cross-section of the array bulk in Fig. 3.3, respectively.

C. 結果與討論

The sample structures and the experimental results are given in this chapter. With the current-voltage (I-V) curves and responsivity of our sample, the characteristics of the detectors can be observed. The influence of doping density in the well is discussed through these experiment results, and the fabricated 1-D detector array is also proposed.

1. SLIP with Doping Density 1×10^{17} in the Superlattice

(1) Sample Structure and Band Diagram

As shown in Fig. 5 (a), the **Sample A** is formed by sandwiching a superlattice structure between the front and rear blocking layers. The superlattice structure consists of 20-period 40Å undoped $Al_{0.32}Ga_{0.68}As$ and 60Å GaAs doped with $1x10^{17}$ cm^{-3}. The blocking layer is 500Å undoped $Al_{0.32}Ga_{0.68}As$, and the contact layer is doped with $1x10^{18}$ cm^{-3}.

Figure 5 (b) shows the energy band diagram of **Sample A** which is estimated by the transfer matrix method with taking into account the band-nonparabolicity [7]. The first miniband is estimated to range between 57.6meV and 66.6meV while the second miniband ranges between 209meV and 264meV. These energies refer to the contact layer. Therefore, the absorption wavelengths are located from 6.01um to 9.37um corresponding to the transitions at zone center and zone edge, respectively. The energy barrier height of the two blocking layers is about 256.3meV.

(2) Current-voltage (I-V) Characteristics

Figure 6 shows the I-V curves under different temperatures. The solid lines present the dark current at temperature 40K to 100K, while the dash line is the photocurrent at temperature 30K under the room temperature background radiation upon the detector. According to the I-V curves, when temperature is above 60K, the difference between the dark current and the background photocurrent becomes very small. Therefore, the background limited performance temperature T_{BLIP} is about 60K.

It is noted that the I-V curves are not symmetrical with the respect to the bias polarity. Larger current at positive biases may be attributed to the dopant migration [8].

(3) Spectral Response

Figure 7 shows the spectral response of **Sample A** under different positive and negative biases. The responsivity is increased with the applied bias, and the lineshape of the photo response is unchanged. Only one peak at the long wavelength 9.05um is observed. This result is consistent with the transition of electrons from the top of the first miniband to the bottom of the second miniband. The maximum responsivity is about 31mA/W at wavelength 9.05um under bias +2.0V, and 15mA/W at wavelength 9.03um under bias -2.0V. The short wavelength absorption corresponding to the electron transitions from the bottom of the first miniband to the top of the

second miniband is disappeared. This phenomenon is because the doping density in superlattice is quite low so that the superlattice is no longer a low resistance structure and voltage drops on it. Therefore, the minibands may not be formed due to the misalignment of the energy states in the adjacent wells. Therefore, the wave function is localized. and the spectral responsivity becomes sharper [9].

Figure 8 shows the spectral response of **Sample A** under biases +1.1V and +1.3V at several temperatures. When the temperature is increased, the carriers in the superlattice will increase by absorbing the thermal energy, and the superlattice becomes more conductive. Therefore, the external bias must be redistributed. The voltage drop on the superlattice is decreased, and more external bias drops on the blocking layers, as shown in Fig. 9. Under low bias, the responsivity is increased with the temperature because more voltage drops on the blocking barriers at high temperature. However, the response is disappeared under high bias at high temperature because the dark current is also increased with temperature. We also show the full width at the half maximum (FWHM) in Fig. 8. The FWHM increased with temperature because the impurity scattering in the superlattice is increased.

Furthermore, the responsivity can be expressed as

$$R(\lambda) = \frac{e\lambda}{hc}\eta g \quad , \tag{1}$$

where c is the velocity of light in the vacuum, g is the optical gain, and η is the quantum efficiency which is the number of photoelectrons generated by per incident photon. With the responsivity taken as 31mA/W under +2.0V, 15mA/W under -2.0V, and the optical gain taken as 1, we estimated the quantum efficiency to be 0.43% at the voltage +2.0V and 0.21% at the voltage -2.0V.

(4) Specific Detectivity

We assume that the shot noise is the main current noise source [10], and takes form as :

$$i_{rms} = 2eI_d\Delta f \ , \tag{2}$$

where I_d is the dark current. So, detectivity is derived as :

$$D^* = R_i\sqrt{\frac{A_d}{2eI_d}} \quad , \tag{3}$$

The peak detectivity D^* at 60K is 3.7×10^8cmHz$^{1/2}$/W under V=1.1V at wavelength 9.1μm and 1.5×10^8 cmHz$^{1/2}$/W under V=1V at wavelength 9.12μm at 80K. The detectivity will be descreased as the temperature increasing. This result is caused by the rapidly increasing dark current.

Layer
N+, GaAs, 1e18, 2000nm
SI, $Al_{0.32}GaAs$, 46nm
SI, $Al_{0.32}GaAs$, 4nm
SI, GaAs, 0.5nm
N+, GaAs, ( ), 5nm
SI, GaAs, 0.5nm
SI, $Al_{0.32}GaAs$, 50nm
N+, GaAs, 1e18, 800nm
SI, GaAs, substrate

×20

(a)

A : 1e17
B : 5e16

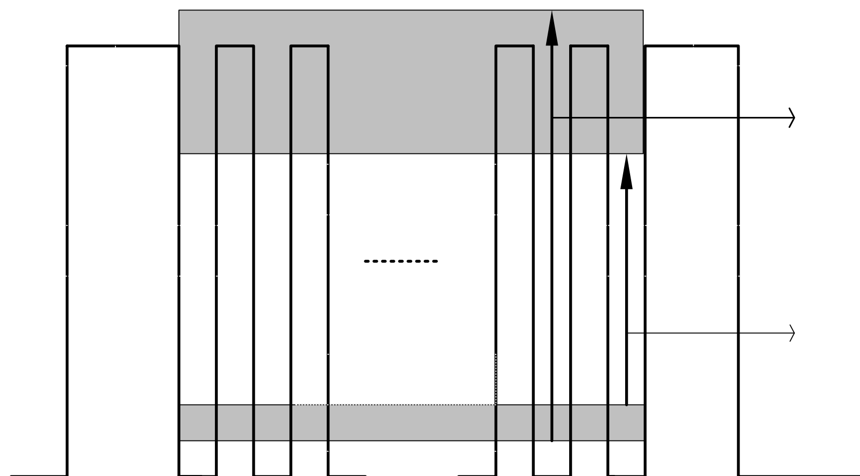

(b)

Fig. 5 (a) The structure of **Sample A** (high doping density 1×10^{17}) and **B** (low doping density 5×10^{16}) (b) Their schematic energy band diagrams.

264me

256.3meV

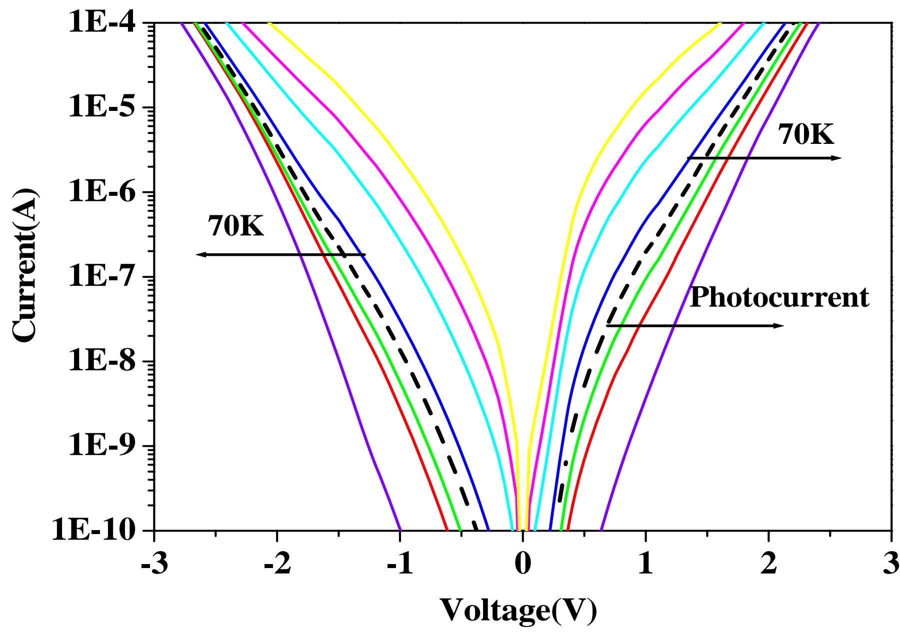

Fig. 6 The current-voltage curves of **Sample A**. The solid lines are the dark current at temperature 40K to 100K, while the dash line is the photocurrent at temperature 30K. The positive voltage means top contact is applied positive biases.

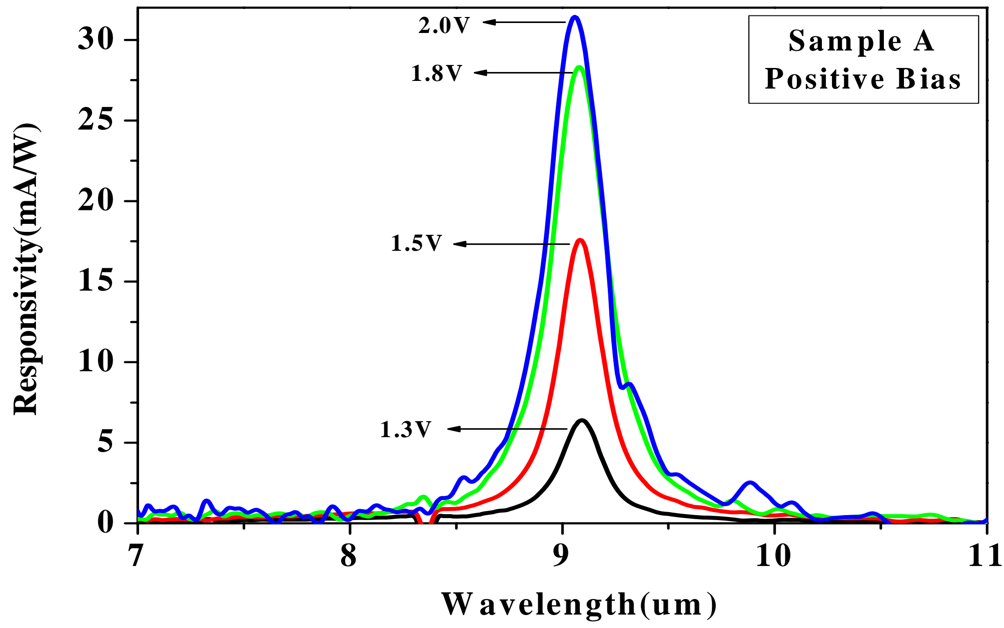

(a)

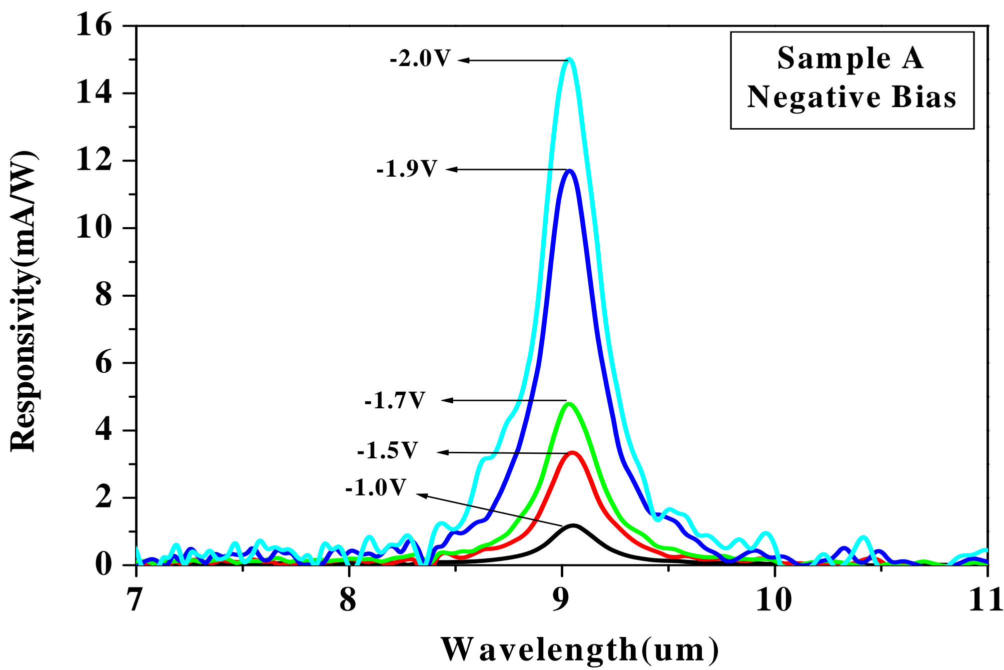

(b)

Fig. 7 The spectral response of **Sample A** measured (a) at several positive biases and (b) at several negative biases.

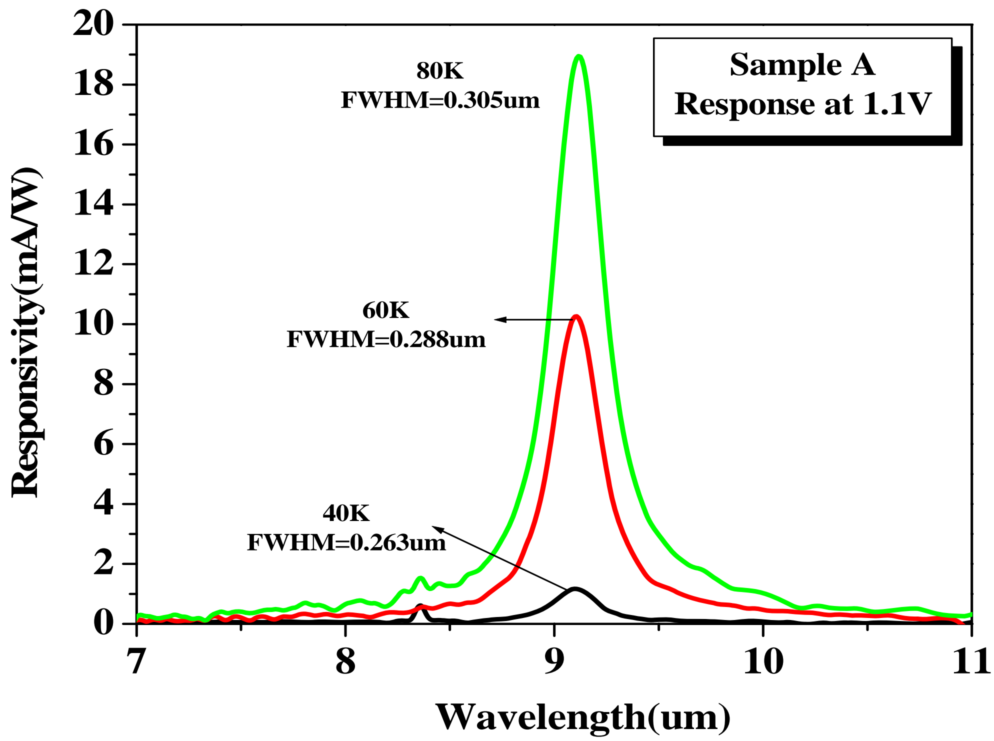

(a)

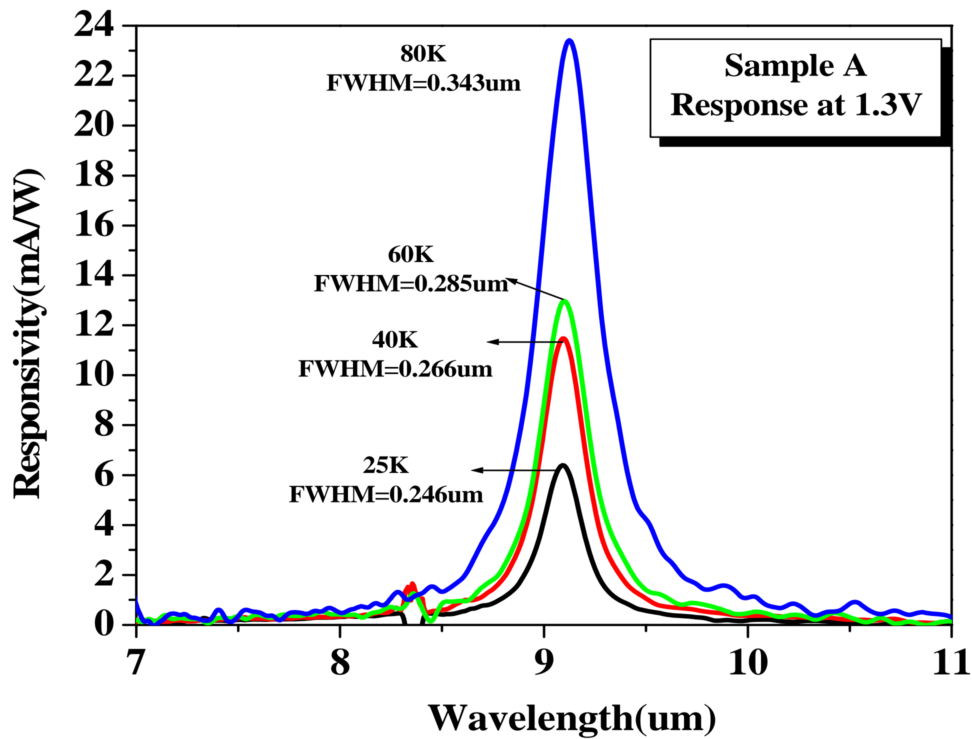

(b)

Fig. 8 The spectral response of **Sample A** (a) under bias +1.1V and (b) under bias +1.3V at several temperatures.

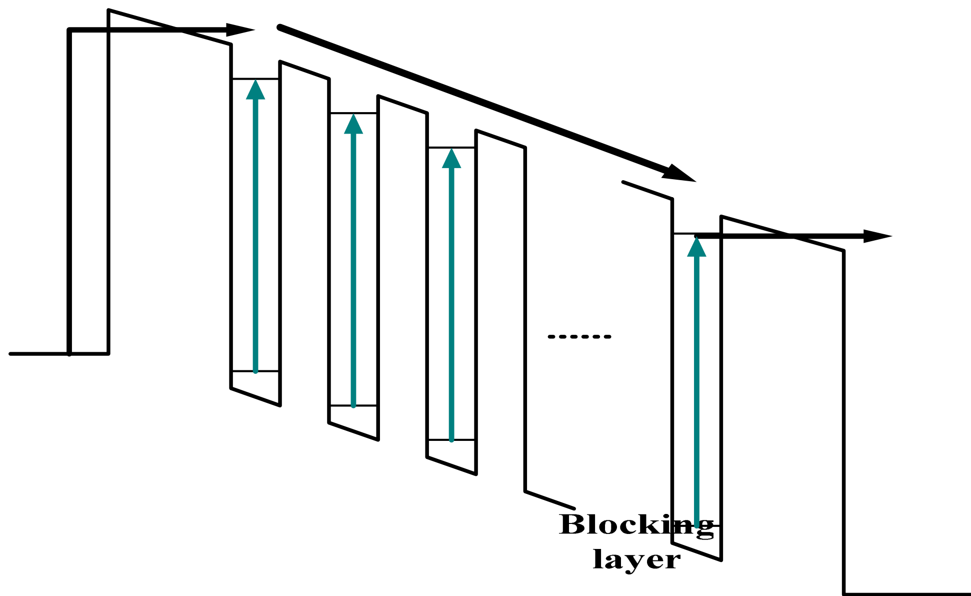

(a)

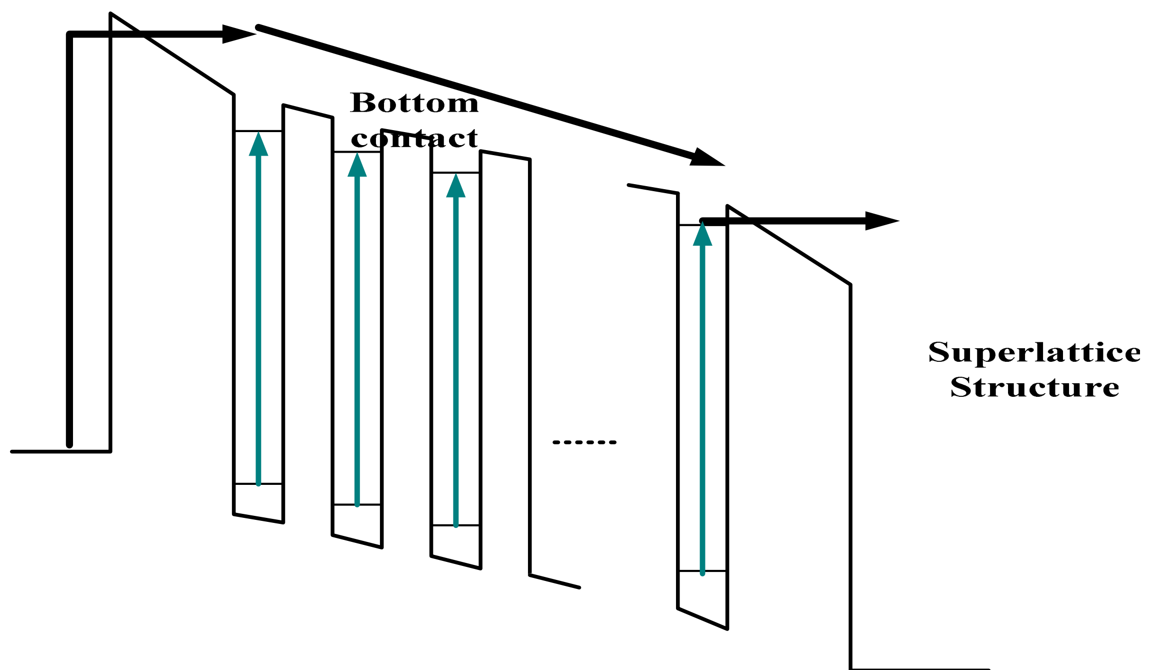

(b)

Fig. 9 The band diagrams under a positive bias : (a) At the low temperature. (b) At the high temperature, the voltage drop on the superlattice becomes lower, and the voltage drop on the blocking layers becomes higher.

2. SLIP with Doping Density 5×10^{16} in the Superlattice

(1) Sample Structure and Band Diagram

In order to see the effect of different doping density in the superlattice, the **Sample B** is designed as the same as **Sample A** except the doping density (5×10^{16} cm^{-3}) in the superlattice. Therefore, the band diagram of **Sample B** is also the same as **Sample A** (as shown in Fig. 5).

(2) Current-voltage Characteristic

The I-V curves of **Sample B** under different temperatures are shown in Fig. 10. The solid lines present the dark current at 40K to 100K, while the dash line is the photocurrent at 30K under the room temperature background radiation upon the detector. According to the I-V curves, we observe the background limited performance temperature T_{BLIP} is up to 70K. The dopant migration can also be observed in **Sample A**.

(3) Spectral Response

The spectral response of **Sample B** under several positive and negative biases is shown in Fig.11. The peak responsivity is about 45.4mA/W under +2.1V, at wavelength 9.15um and 40mA/W under -2.5V, at wavelength 9.21um.

Figure 12 shows the spectral response of **Sample B** under biases +1.2V and +1.4V at several temperatures. The reason that the responsivity of **Sample B** is increased with temperature is the same as **Sample A**. When the temperature increases, the external bias must be redistributed. The voltage drop on the blocking barriers is increased, and the response becomes larger than that at low temperature. We can also see that the FWHM of **Sample B** is increased with temperature.

With the responsivity taken as 45.4mA/W under +2.1V, and 40mA/W under -2.5V, we estimated the quantum efficiency to be 0.62% at the voltage +2.1V and 0.54% at the voltage -2.5V.

(4) Specific Detectivity

The peak detectivity D^* at 60K is $2.44 \times 10^9 cmHz^{1/2}/W$ under +1.2V at wavelength 9.19μm, and $9.44 \times 10^8 cmHz^{1/2}/W$ under +1.4V at wavelength 9.20μm at 80K. The detectivity will be descreased as the temperature increasing. This result is caused by the rapidly increasing dark current.

3. Comparison of Sample A and Sample B

In order to compare the performance of **Sample A** (high doping density $1 \times 10^{17} cm^{-3}$) and **Sample B** (low doping density $5 \times 10^{16} cm^{-3}$), we summarized those experimental results for analysis. Figure 13 shows the I-V curves under different temperatures. The solid lines are the dark current at 60K and 70K , while the dash line is the photocurrent at 30K. Because the doping density in the well in **Sample A** is higher than that in **Sample B**, the dark current and photocurrent of **Sample A** are higher than **Sample B**. However, the background limited

performance temperature T_{BLIP} of **Sample B** (70K) is larger than that of **Sample A** (60K).

We also show the responsivity comparison in Fig. 14. **Sample B** has better responsivity for both forward and reverse biases than **Sample A**. This may be due to the impurity scattering in the well. When the electrons are excited by the photons into the second miniband, and oscillate between two blocking layers, these electrons will be scattered by the impurities in the wells into the first miniband, and emit the LO phonons. It is expected that the absorption rate of photons and the scattering rate of electrons in the superlattice are both proportional to the doping density in the well. Their effects on the photocurrent will cancel each other. According to our experimental results, the device with low doping density is better than the high doping density one because of the decrease of impurity scattering.

The operational voltage of **Sample A** ranges from 1.3V to 2.0V, under forward bias and from -0.9V to -2.0V under reverse bias. The operational voltage of **Sample B** ranges from 1.3V to 2.2V under forward bias, and from -1.7V to -2.5V under reverse bias. Because the voltage drop in the superlattice of **Sample B** is higher than **Sample A**, the operational voltage of **Sample B** is higher than **Sample A**.

Sample B has better quantum efficiency under both forward and reverse biases than **Sample A**. The detectivity of **Sample A** and **B** under several positive biases at 60K and at 80K are shown as Fig. 15. The detectivity of **Sample A** is lower than **Sample B** at 60K and 80K.

As a consequence, **Sample B** (doping density $5x10^{16}cm^{-3}$) has better background limited performance temperature T_{BLIP}, responsivity, quantum efficiency, and detectivity.

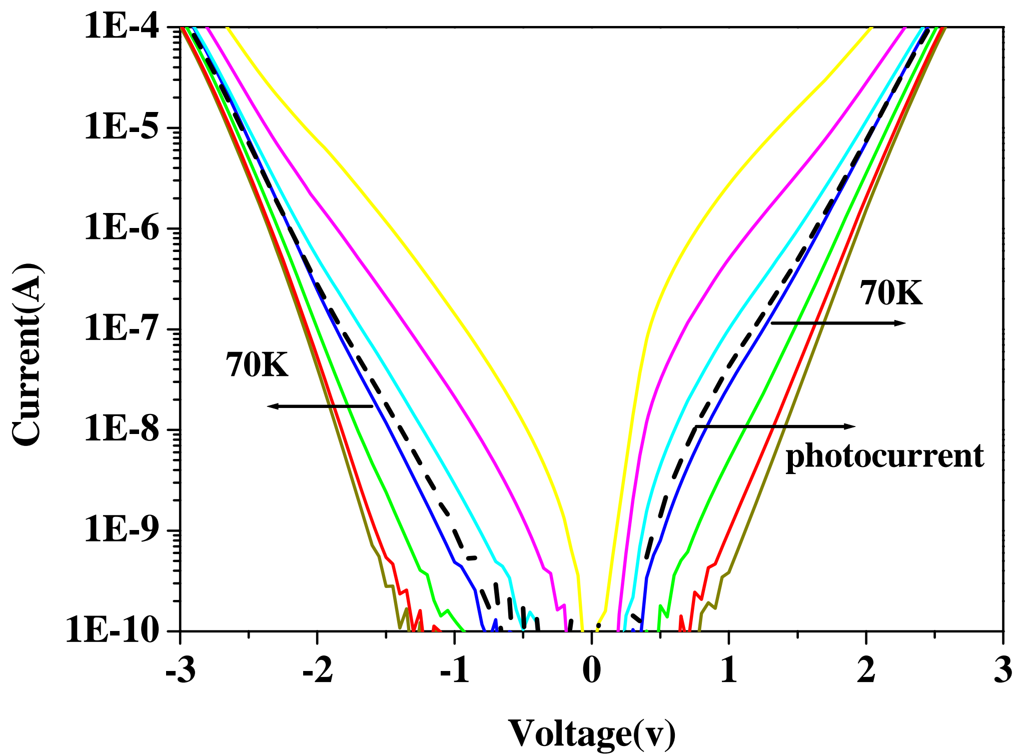

Fig. 10 The current-voltage curves of **Sample B**. The solid lines are the dark current at temperature 40K to 100K, while the dash line is the photocurrent at temperature 30K.

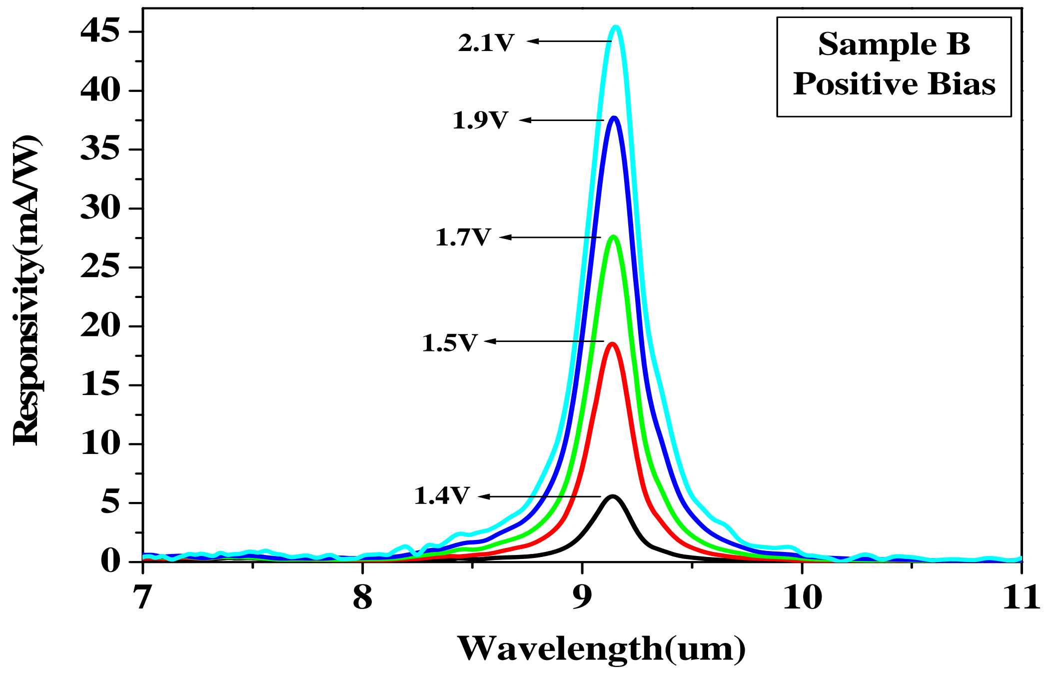

(a)

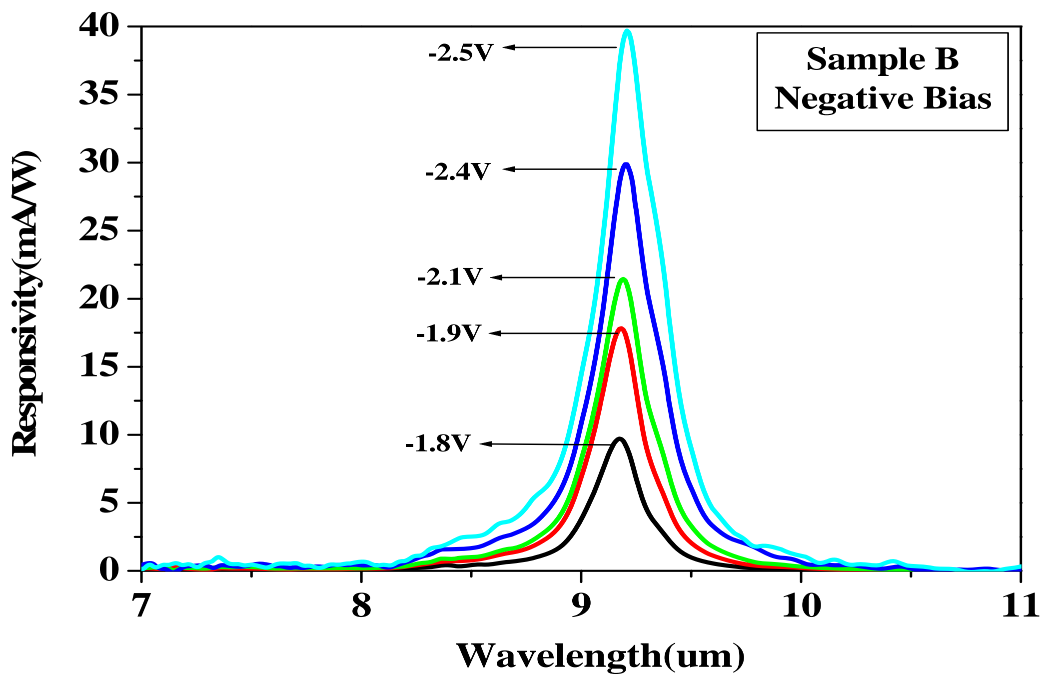

(b)

Fig. 11 The spectral response of **Sample B** measured (a) at several positive biases and (b) at several negative biases.

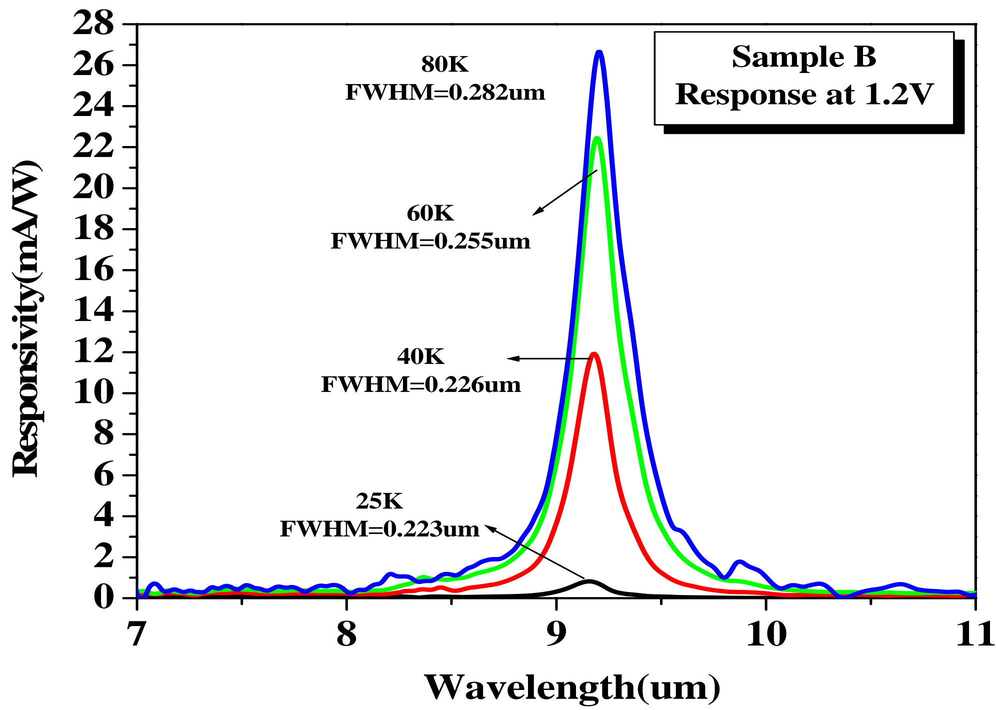

(a)

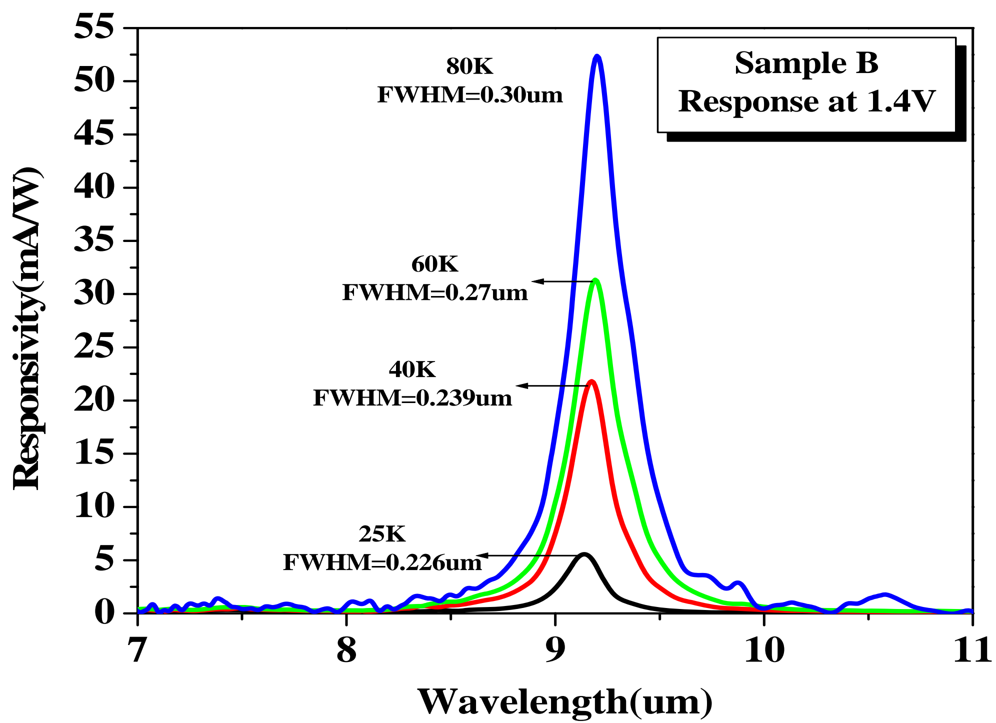

(b)

Fig. 12 The spectral response of **Sample B** (a) under bias +1.2V and (b) under bias +1.4V at several temperatures.

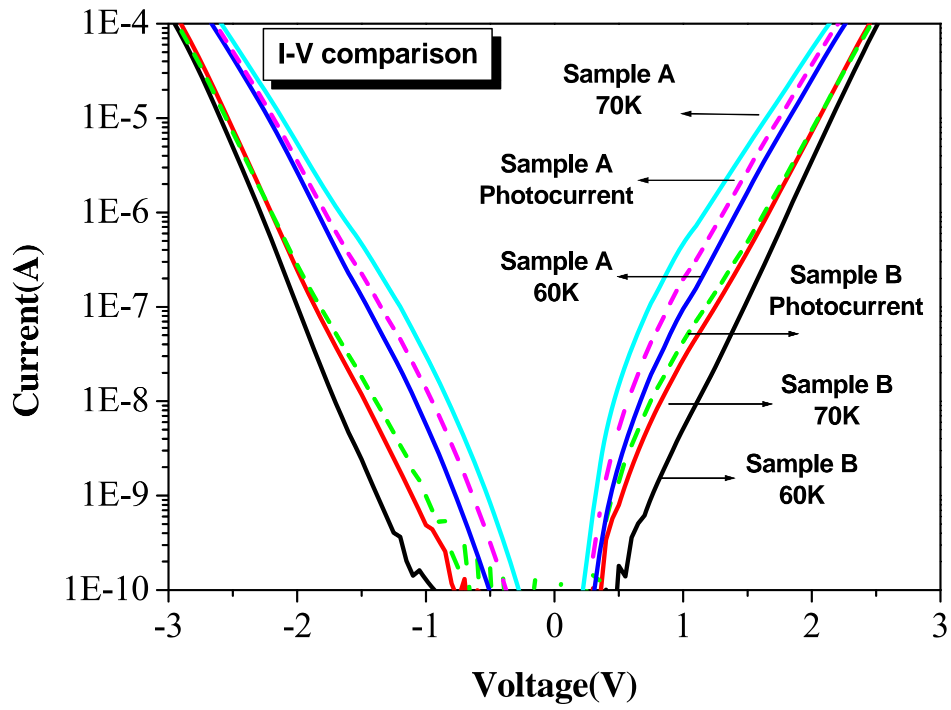

Fig. 13 The I-V curves of **Sample A** and **B**. The solid lines are the dark current at temperature 60K and 70K , while the dash line is the photocurrent at temperature 30K.

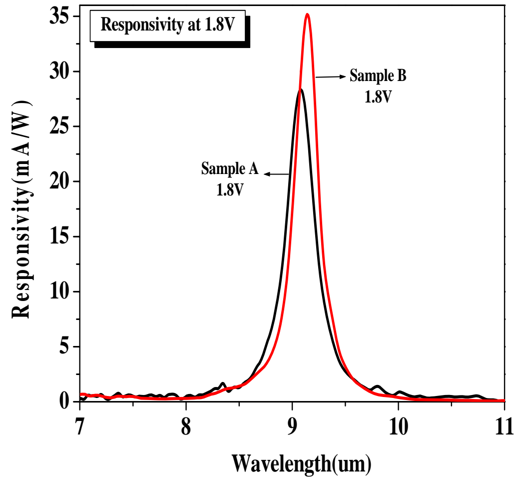

(a)

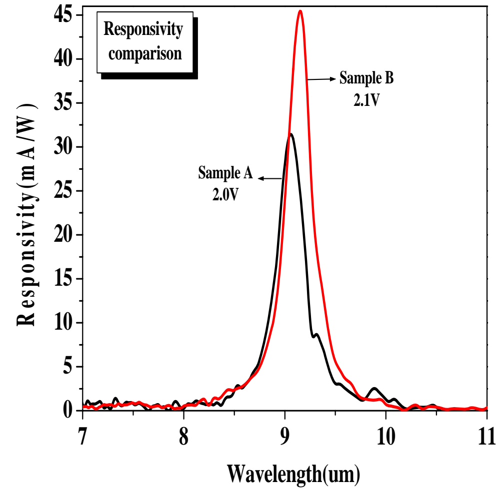

(b)

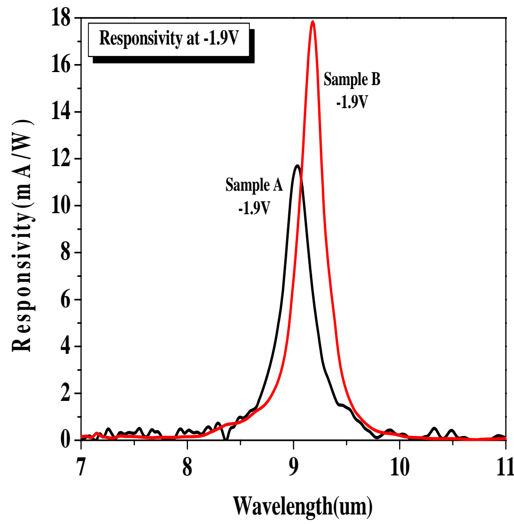

(c)

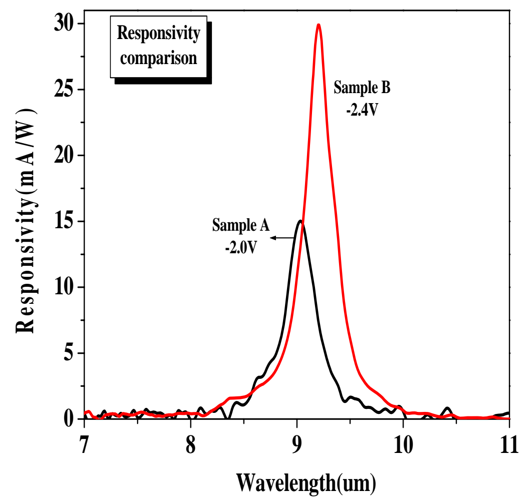

(d)

Fig. 14 The spectral response comparison. **Sample B** has better responsivity for both forward and reverse biases than **Sample A**.

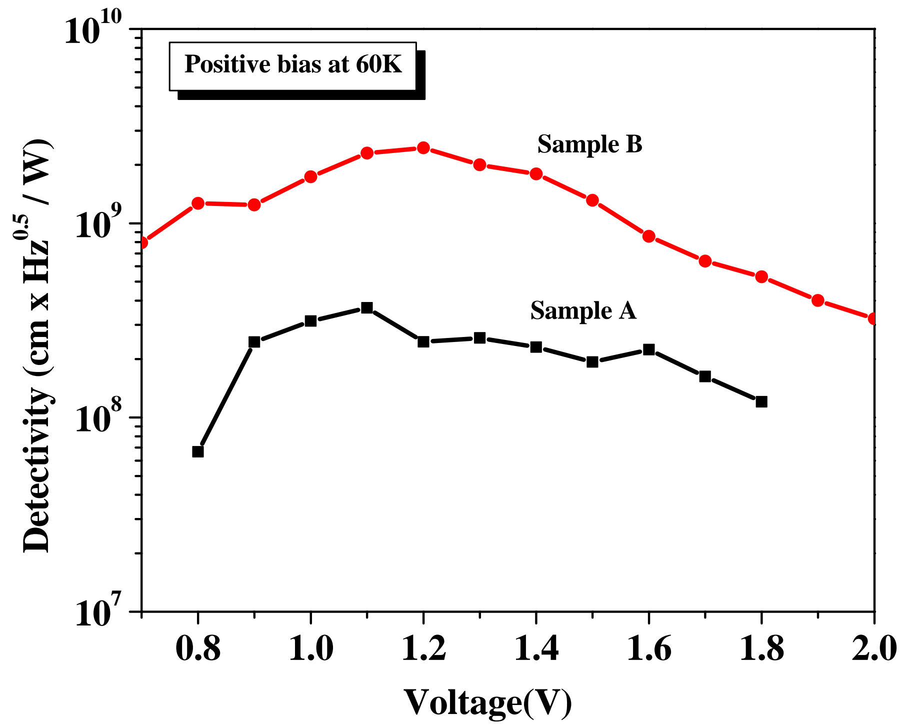

(a)

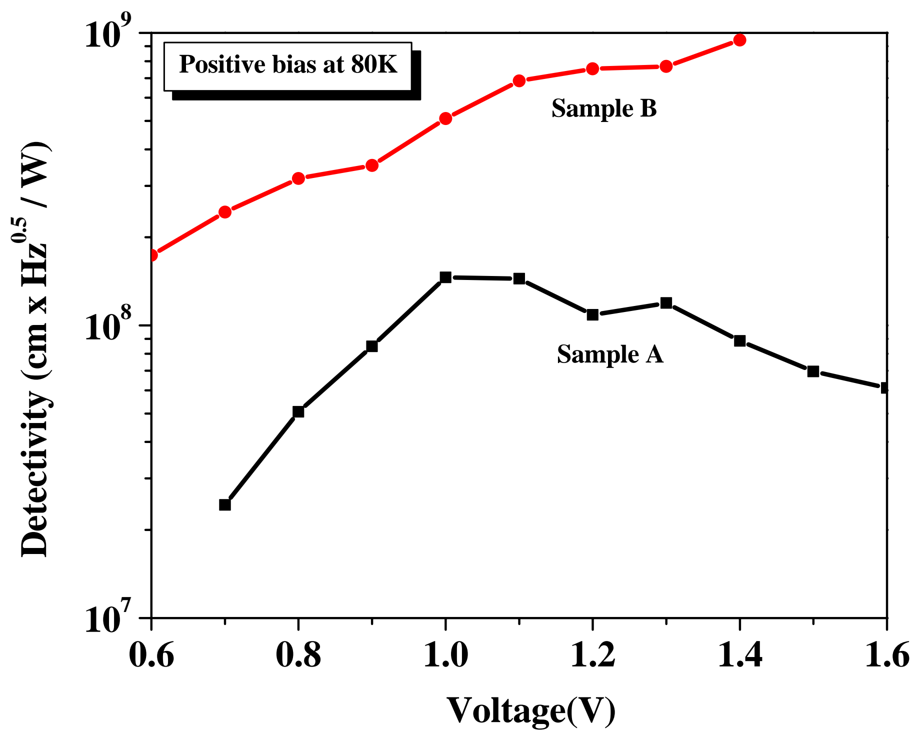

(b)

Fig. 15 The detectivities of **Sample A** and **B** under several positive biases (a) at 60K and (b) at 80K.

4. 1-D Detector Array

In the section, we will show some experimental results of 1-D detector array. The sample structure is the same as **Sample A** (as shown in Fig. 5). New process for 1-D array is used, so some fabrication results are proposed first.

(1) Fabrication Result

Figure 16 shows the SEM picture of the trench with the optical isolation structure which is fabricated by PECVD deposition silicon nitride (Si_3N_4) and sputtering titanium (Ti) on the wall of the trench. It is noted that the thicknesses of the Si_3N_4 and Ti on the wall are about 1500Å and 400Å when the deposition thickness is 2000Å on the top surface of the sample. Because the skin depth of Ti at the wavelength 9um is about 300Å, so we sputter thickness 5000Å on the top surface of the sample and thickness 1000Å on the wall of the trench to ensure that light would be reflected by the metal-insulator-semiconductor (MIS) structure.

In order to couple the normal incident light, the V-groove coupling scheme is fabricated. Figure 17 shows the AFM picture of several V-grooves, and the tilted angel is about 41°. These facets can direct the normal incident light into the device though refraction, as shown in Fig. 18 (a). In order to analyze the couple efficiency of different tilted angles, we assume the incident light is TM mode and calculate the electrical field ratio of the refraction component to the incident light versus the tilted angle. The result is shown in Fig. 18 (b). We can see that the electrical ratio is 34.3% when the tilted angle is 41°. The maximum is 39.5% if the tilted angle is 54°. Finally, the fabricated detector array is shown in Fig. 19.

(2) Current-voltage Characteristic

Fig. 20 shows the I-V curves of 1-D detector array under different temperatures. The solid lines present the dark current from 20K to 80K, while the dash line is the photocurrent at 25K under the room temperature background radiation upon the detector. The dark current begins to dominate when temperature is above 50K. The background limited performance temperature T_{BLIP} is up to 50K for the forward bias smaller than 1.4V, and reverse bias smaller than 1.3V.

(3) Spectral Response

The spectral response of 1-D detector array under several positive and negative biases is shown in Fig. 21. The peak responsivity is about 10.3mA/W under +2.6V, at wavelength 8.95um and 2.85mA/W under -2.2V, at wavelength 9.03um.

With the responsivity taken as 10.3mA/W under +2.6V, and 2.85mA/W under -2.2V, we estimated the quantum efficiency to be 0.14% at the voltage +2.1V and 0.04% at the voltage -2.5V.

(4) Specific Detectivity

The peak detectivity D^* at 60K is 8.02×10^8cm$Hz^{1/2}$/W under +1.5V at wavelength 9.02μm, and 2.15×10^8cm$Hz^{1/2}$/W under 1.4V at wavelength 9.04μm at 80K. The decrease of detectivity with

the increase of temperature is caused by the rapid increasing dark current.

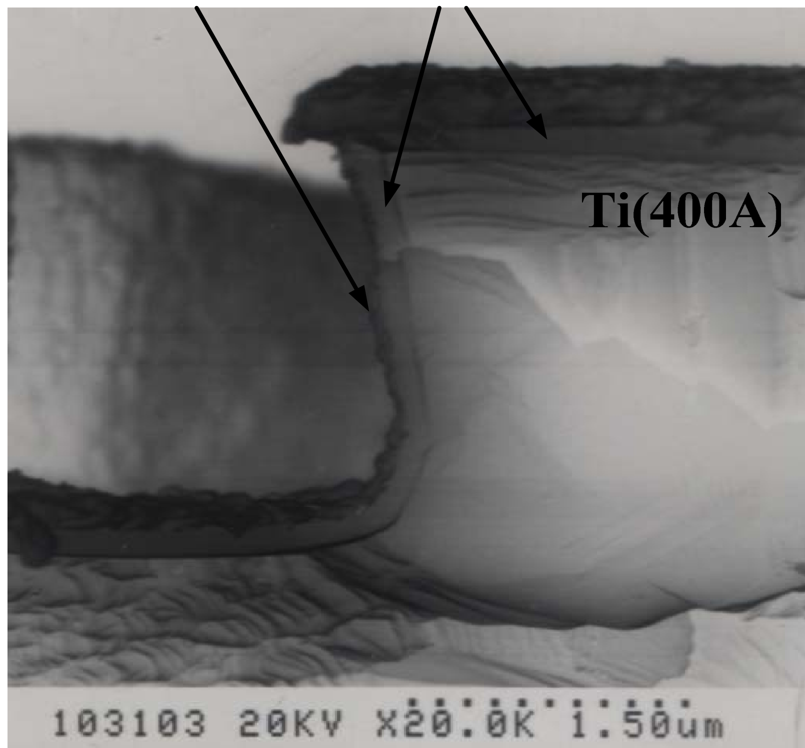

Fig. 16 The SEM picture of the trench with the PECVD deposition Si_3N_4 and sputtering Ti on the wall of the trench. The thicknesses of the Si_3N_4 and Ti on the wall are about 1500Å and 400Å when the deposition thickness is 2000Å on the top surface of the sample.

5. Comparison of Single Device and 1-D Detector Array

In order to analyze the performance of 1-D detector array, we summarized experimental results. Figure 22 shows the I-V curves under different temperatures. The solid lines are the dark current, while the dash line is the photocurrent at 30K. We can observe both the dark current and photocurrent of single device are higher than detector array. This may be contributed that the contact resistance of the detector array is much higher than the single device. As shown in Figure 18(c), the area of the detection pixel is $45x45um^2$, and the contact is a metal ring which thickness is about 1um. It may make the higher contact resistance and lower current density. In order to make sure that the contact area will affect the current density, we apply silver on the detection pixel to increase the contact area. Figure 23 shows the I-V curves of the device which have Ag on the detection pixel or not. We can see that the current density of the device with Ag is much larger than the device without Ag. As a consequence, the higher contact resistance is caused by the small contact area.

Next, we show the comparison of spectral response in Fig. 24. The single device has better responsivity for both forward and reverse biases than the 1-D detector array. Besides the higher contact resistance of the detector array, the efficiency of V-grooves coupling scheme is another factor that affects the spectral response.

The detectivities of single device and 1-D array under several positive biases at 60K and 80K is shown in Fig. 25. Although the response of single device is larger than detector array, the detectivity of the single device is lower than detector array at 60K and 80K. This is because the dark current of single device is much higher than that of the detector array.

(a)

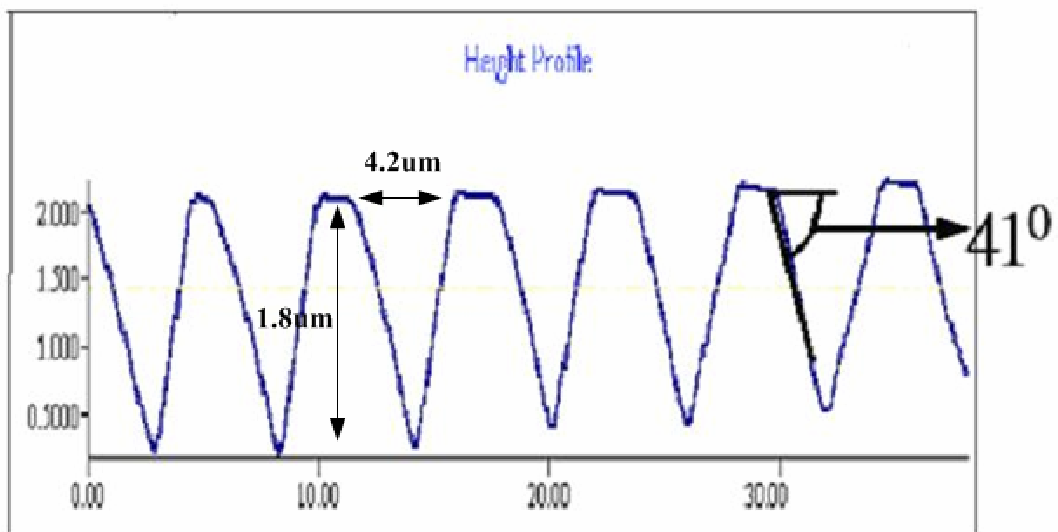

(b)

Fig. 17 The AFM picture of several V-grooves : (a) the original pattern, and (b) the profile of the AA' direction. The tilted angel is about 41°.

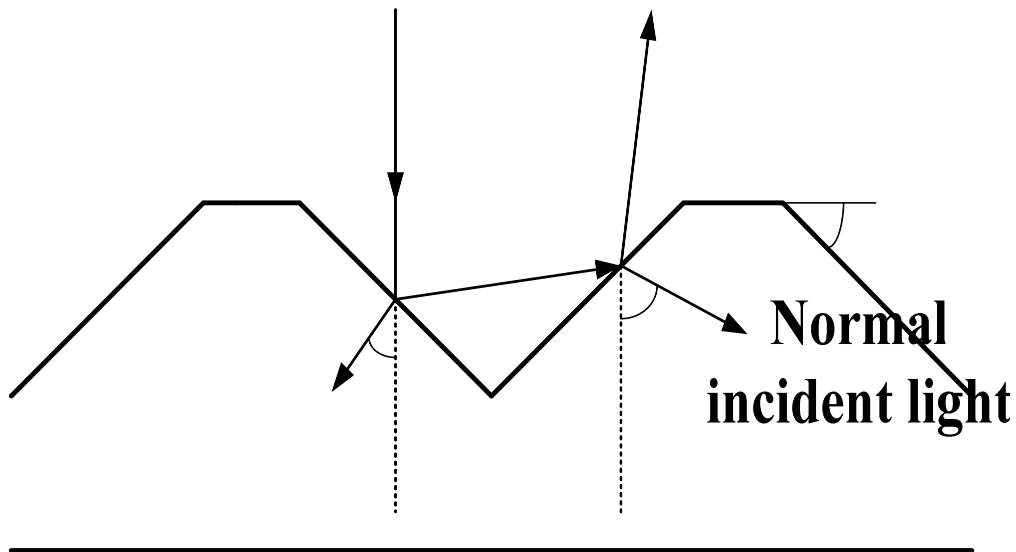

(a)

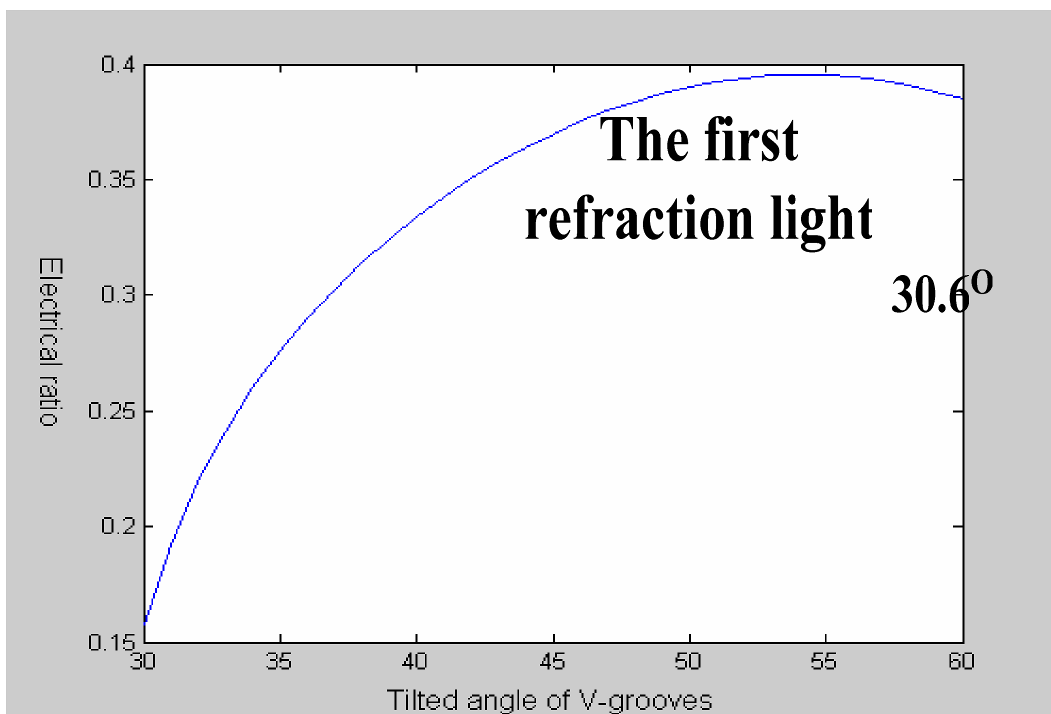

(b)

Fig. 18 (a) The optical path of normal incident light into the device though refraction (b) The electrical field ratio of the refraction component to the normal incident light versus the tilted angle.

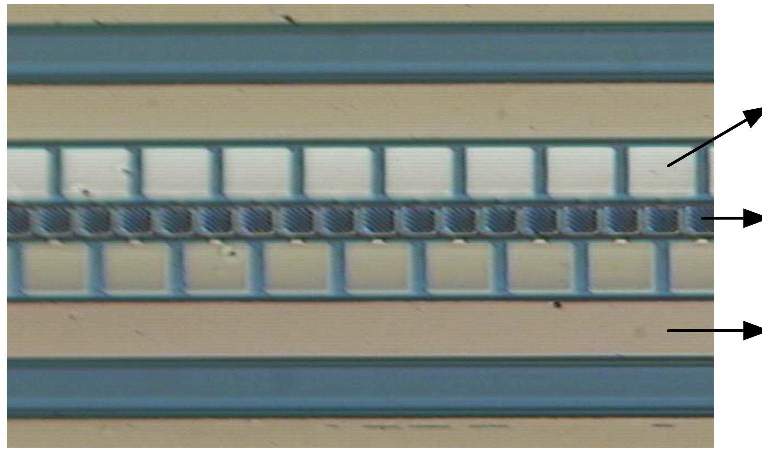

(a)

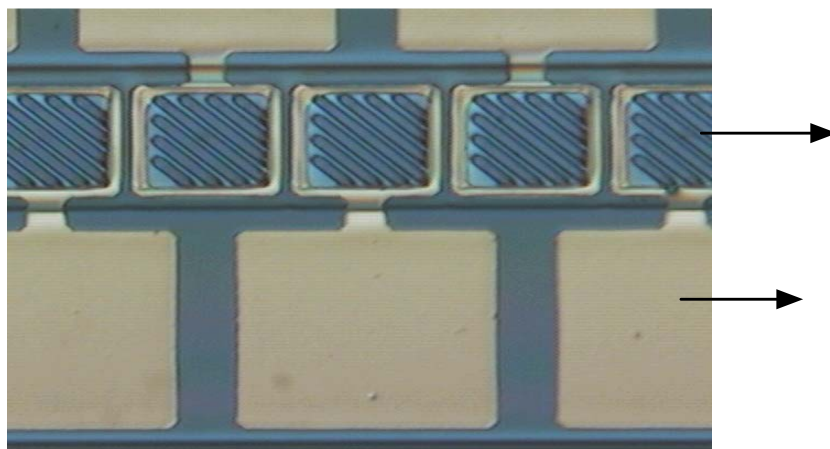

(b)

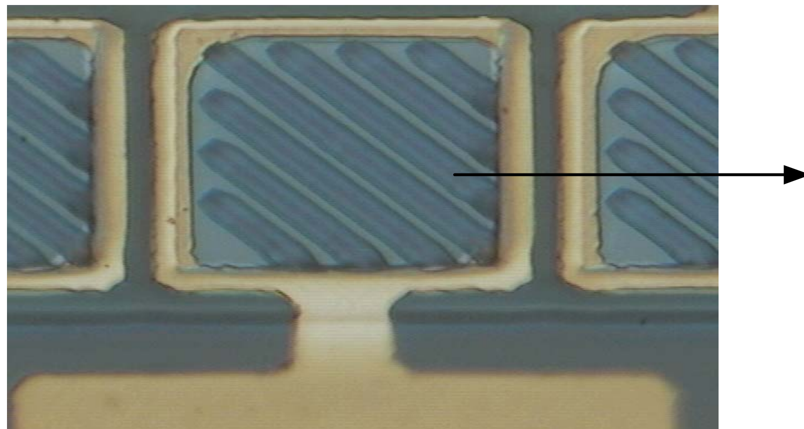

(c)

Fig. 19 The fabricated 1-D detector array : (a) original size X 50 (b) X 200 (c) X 500

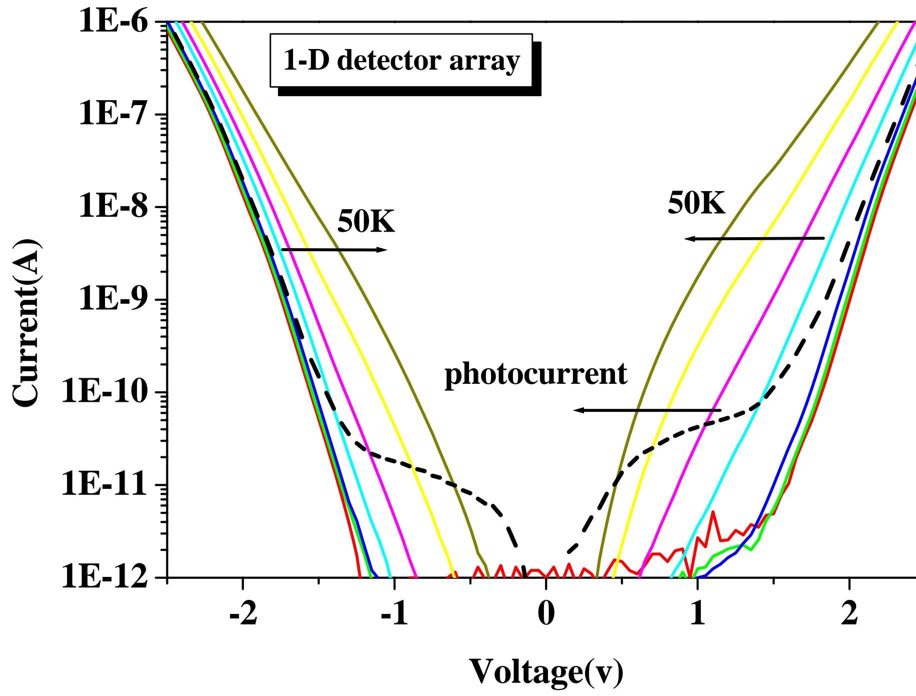

Fig. 20 The current-voltage curves of 1-D detector array. The solid lines are the dark current at temperature 20K to 80K, while the dash line is the photocurrent at 25K.

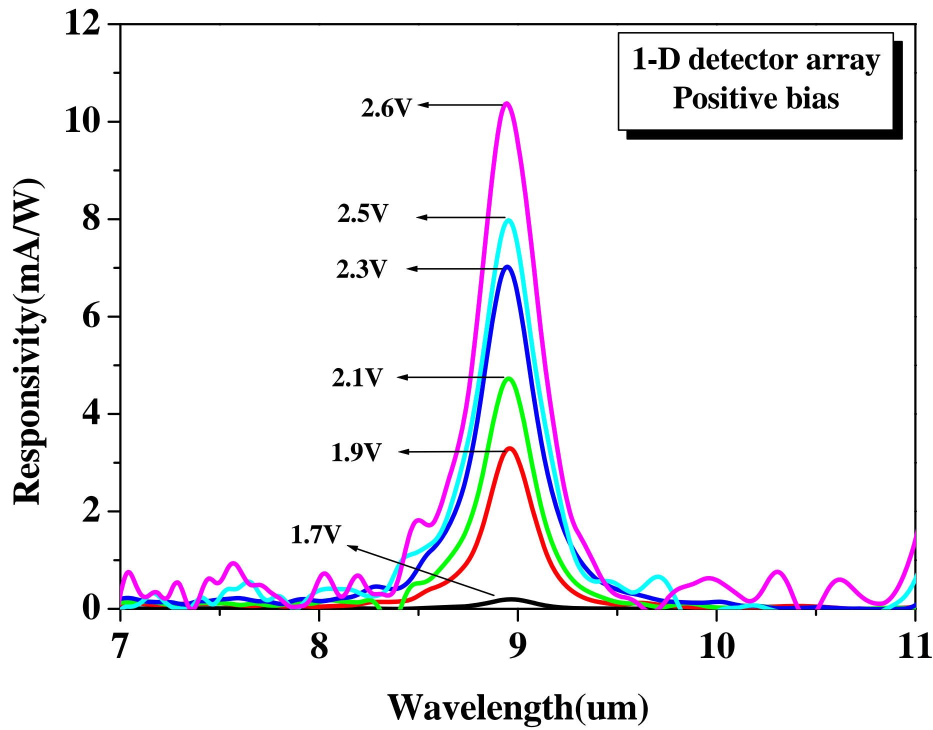

(a)

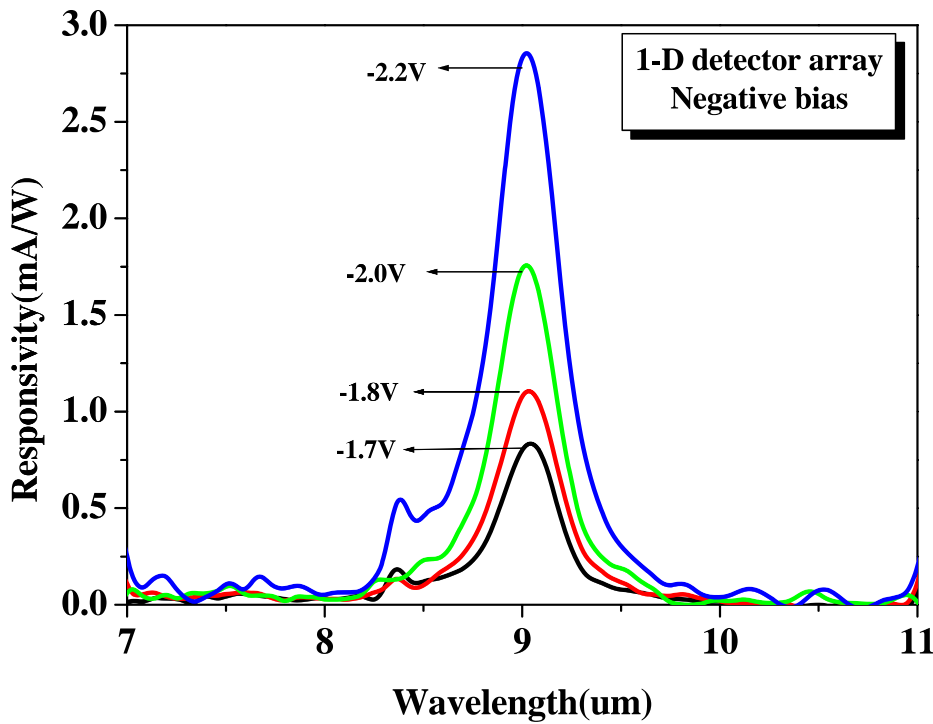

(b)

Fig. 21 The spectral responsivity of 1-D detector array measured (a) at several positive biases and (b) at several negative biases.

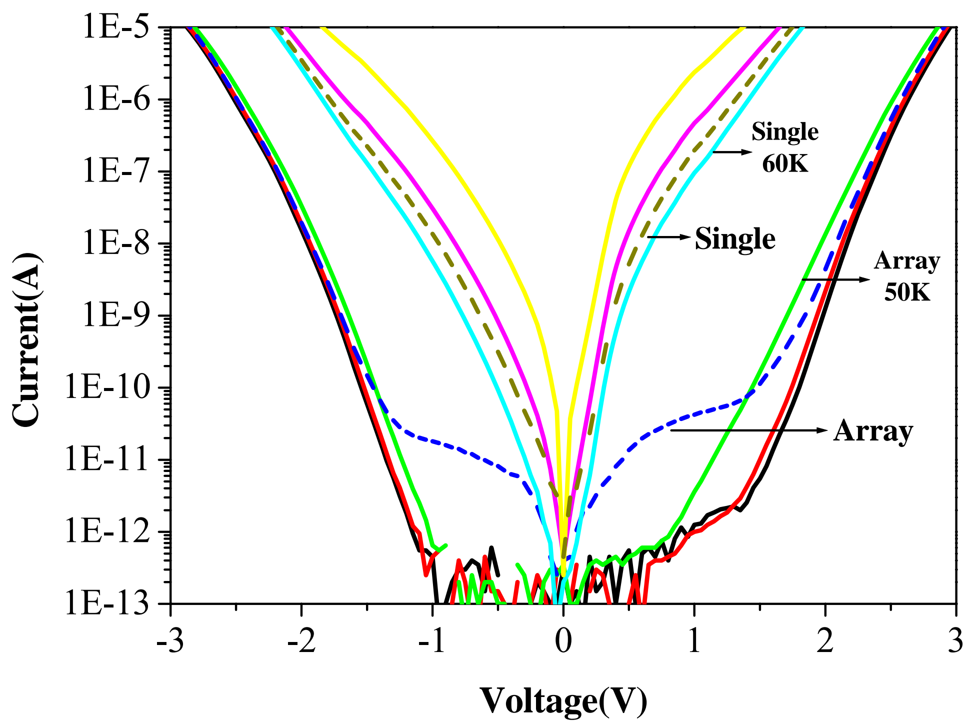

Fig. 22 The I-V curves of single device and 1-D detector array. The solid lines are the dark current , while the dash line is the photocurrent at temperature 30K.

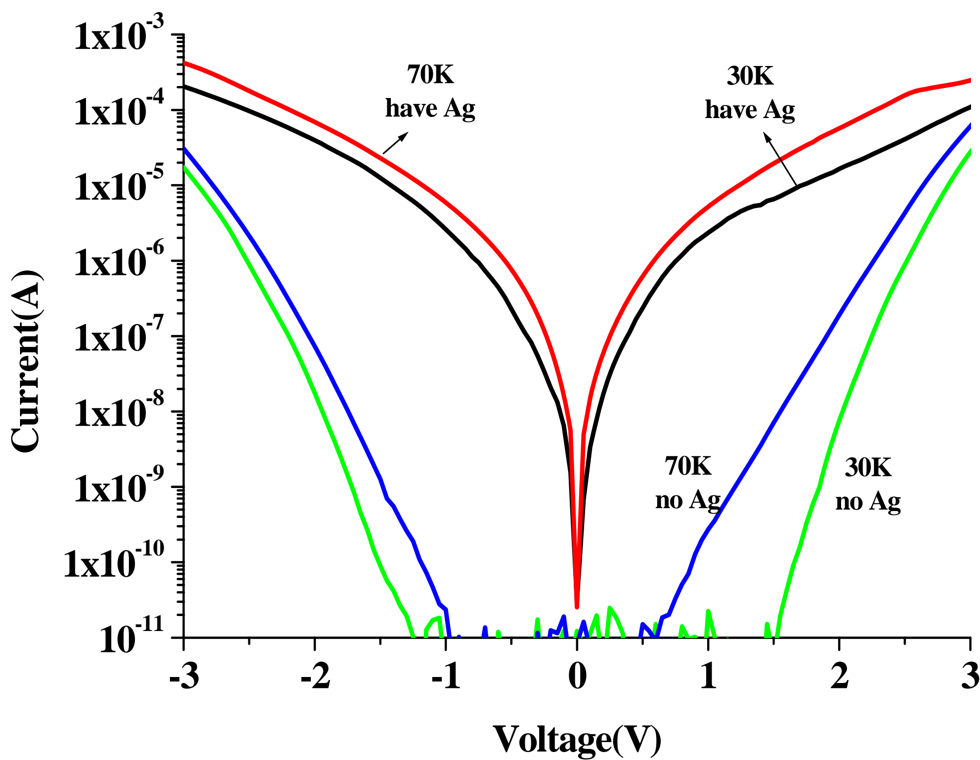

Fig. 23 The dark currents of 1-D detector array which have Ag on the detection pixel or not. The current density of the device with Ag is much larger than the device without Ag.

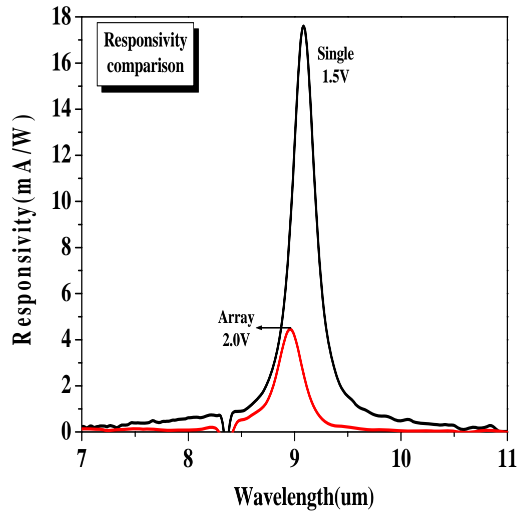

(a)

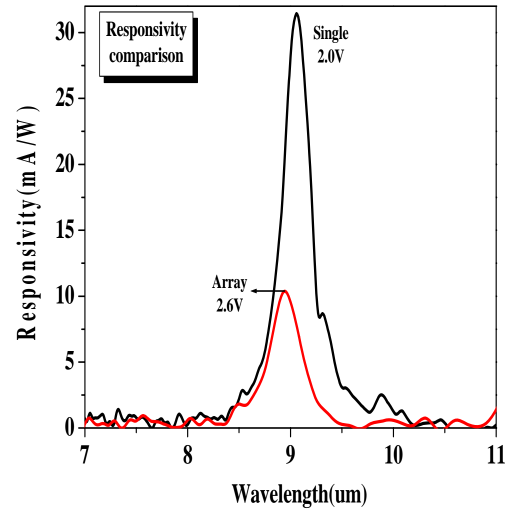

(b)

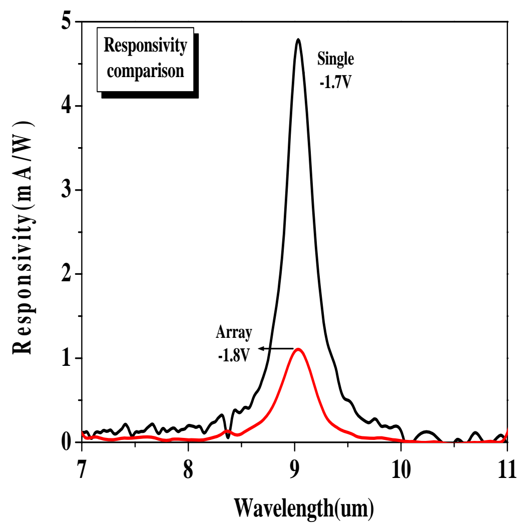

(c)

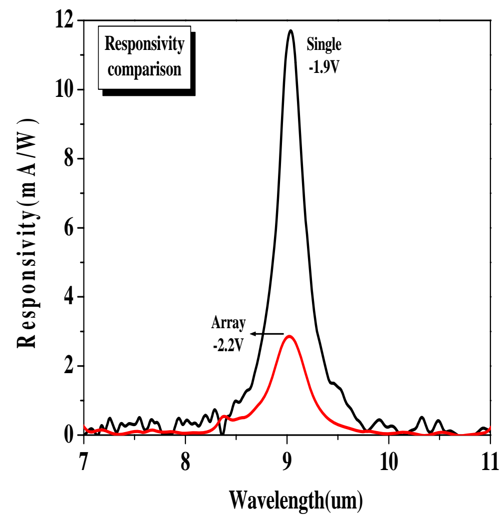

(d)

Fig. 24 The spectral response comparison. Single device has better responsivity for both forward and reverse biases than 1-D detector array.

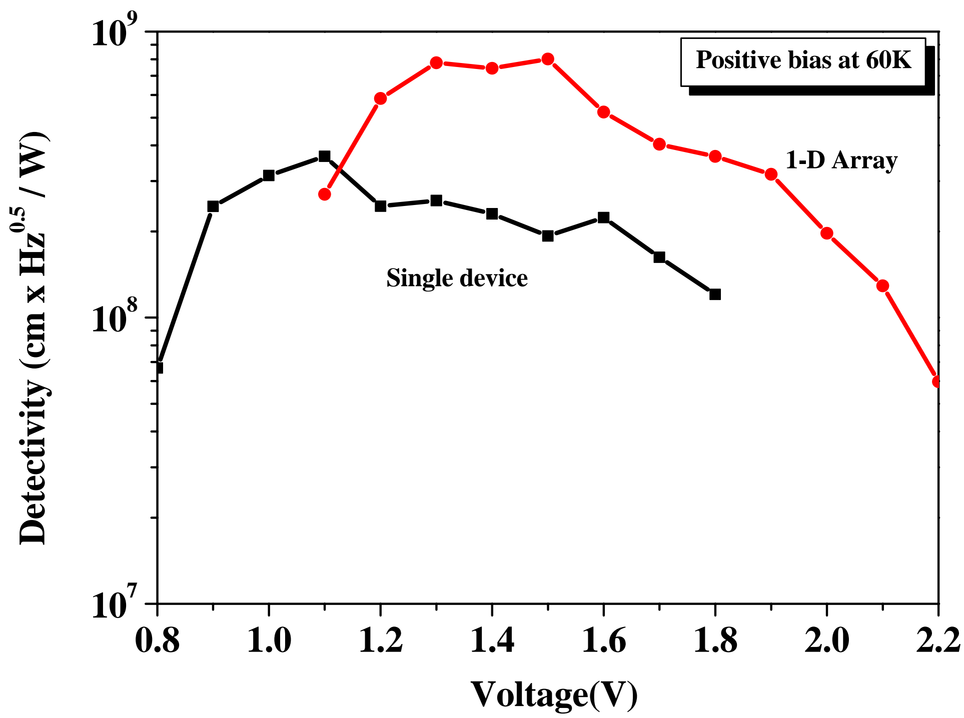

(a)

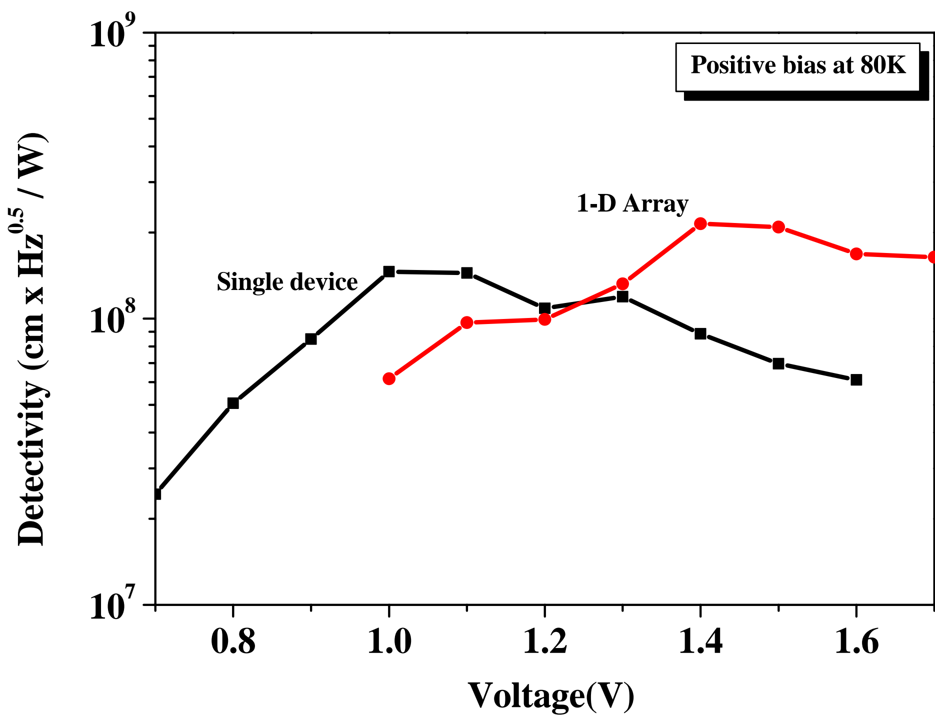

(b)

Fig. 25 The detectivities of single device and 1-D array under several positive biases (a) at 60K and (b) at 80K.

D. 結論與計畫自評

In the report, we discuss the effect of doping density in the superlattice with the comparison of the experimental results of **Sample A** (high doping density 1×10^{17}) and **Sample B** (low doping density 5×10^{16}). Besides, we also develop a fabrication process of 1-D detector array for the thermal imaging application.

From the I-V curves, the dark current and photocurrent of **Sample A** are larger than those of **Sample B**, and the background limited performance temperature T_{BLIP} of **Sample B** (70K) is higher than **Sample A** (60K).

Next, we summarize the spectral response. **Sample B** has better responsivity for both forward and reverse biases than **Sample A**. It may be attributed to the impurity scattering in the well. The absorption rate of photons and the scattering rate of electrons are both proportional to the doping density in the well, and their effects on the photocurrent cancel each other. As a result, **Sample B** has better responsivity, and quantum efficiency. It is concluded that the performance of **Sample B** (low doping density 5×10^{16}) is better than **Sample A** (high doping density 1×10^{17}) due to the decrease of the impurity scattering.

The fabrication process of 1-D detector array is illustrated and investigated. In the process, the V-groove couple scheme is used instead of the edge couple one, and the optical isolation formed by metal-insulator-semiconductor (MIS) structure is used to prevent the crosstalk between the detection pixels. Each step of the process is investigated and then integrated into the complete fabrication process. The experimental results of the fabricated 1-D detector array are also proposed to analyze the performance.

The peak responsivity of 1-D detector array is 10.3mA/W at the voltage +2.6V, which is smaller than sample A (31mA/W under bias +2.0V). The dark current of detector array is much smaller than single device. This may be due to the higher contact resistance of detector array.

In the future, we will improve the process of 1-D detector to increase the contact area of metal ring for lower contact resistance and larger tilted angle for better couple efficiency. It will be a new method to fabricate 1-D detector for thermal imaging applications.

E. 參考文獻

[1] Ralph E. Williams, “*Gallium Arsenide Processing Techniques*,” published by the Artech House Microwave Library, copyright 1984.

[2] “*Gallium Arsenide Materials, Devices, and Circuits*,” edited by M. J. Howes and D.V. Morgan (1985).

[3] D.W. Shaw, J. electrochem. Soc., Vol. 128, No.4, 874-880, 1981.

[4] C. J. Chen, K. K. Choi, M. Z. Tidrow, and D. C. Tsui, *Appl. Phys. Lett*. 68, 1446, 1996.

[5] K.K. Choi *“The Physics of Quantum Well Infrared Photodetectors”*, Published by World Scientific.

[6] S. Iada, K. Ito, J. electrochem. Soc., Vol. 118, No.5, 768-771, 1971.

[7] K. K. Choi, S. V. Bandara, S. S. Gunapala, W. K. Liu, and J. M. Fastenau, *J. Appl. Phys.* **91**, 2, pp.551
[8] *The Physics of Quantum Well Infrared Photodetectors*, edited by K. K. Choi (1997)
[9] W. H. Hsieh, C. C. Chen, J. M. Chen, Y. W. Suen and C. H. Kuan, Proceedings of Photonics West 2001.
[10] C. C. Chen, H. C. Chen, M. C. Hsu, W. H. Hsieh, C. H. Kuan, S. Y. Wang, and C. P. Lee, *J. Appl. Phys.* **91**,3,943 (2001)

3. Superlattice Infrared Photodetector with Grating Structure for Normal Incident Light Coupling

A. 前言

QWIPs do not absorb radiation incident normal to the surface since the light polarization must have an electric field component normal to the growth direction to be absorbed by the confined carriers. When the incoming light contains no polarization component along the growth direction, the matrix element of the interaction vanishes. As a consequence, these detectors have to be illuminated through a 45^0 polished facet. However, this illumination scheme limits the configuration of detectors to linear arrays and single elements. For imaging, it is necessary to couple light to two-dimension arrays of these detectors uniformly.

Some different methods can to deflect the incoming light away from the direction normal to the surface, enabling intersubband absorption, such as random reflectors, two-dimension periodic gratings, corrugated structure, microlenses and so on. In the thesis, normal light incident is successful by using periodic gratings

Surface plasmon at the interface between a metal and a dielectric material have a combined electromagnetic wave and surface charge character as shown in Fig. 1. They are transverse magnetic in character (H is in the y direction), and the generation of surface charge requires an electric field normal to the surface. This combined character also leads to the field component perpendicular to the surface being enhanced near the surface and decaying exponentially with distance away from it. The field in this perpendicular direction is said to be evanescent, reflecting the bond, non-radiative nature of surface plasmon, and prevents power from propagating away from the surface. The surface plasmon mode has the momentum mismatch problem that must be overcome in order to coupling light and surface plasmon modes together, with the surface plasmon mode always lying beyond the light line, this is, it has greater momentum than a free space photon of the same frequency.

The enhanced transmission through periodic arrays of subwavelength holes in optically thick metallic films has demonstrated. Not only is the transmission much higher than expected from classic diffraction theory, it can be greater than the percentage area occupied by the holes, implying that even the light impinging on the metal between the holes can be transmitted. For a square array of period a_0 the peaks λ_{max} the normal incidence transmittance spectral can be identified approximately from the dispersion relation, and they are given by :

$$\lambda_{\max}\sqrt{i^2 + j^2} \approx a_0\sqrt{\frac{\varepsilon_m\varepsilon_d}{\varepsilon_m + \varepsilon_d}} \qquad (2.3)$$

where indices i and j are the scattering orders from the array.

In order to apply surface plasmon in our device, we make the grating structure on our mesa. We will discuss the phenomenon in following sections. Fig. 2 shows an accomplished surface

structure by using Scanning Electron Microscope (SEM).

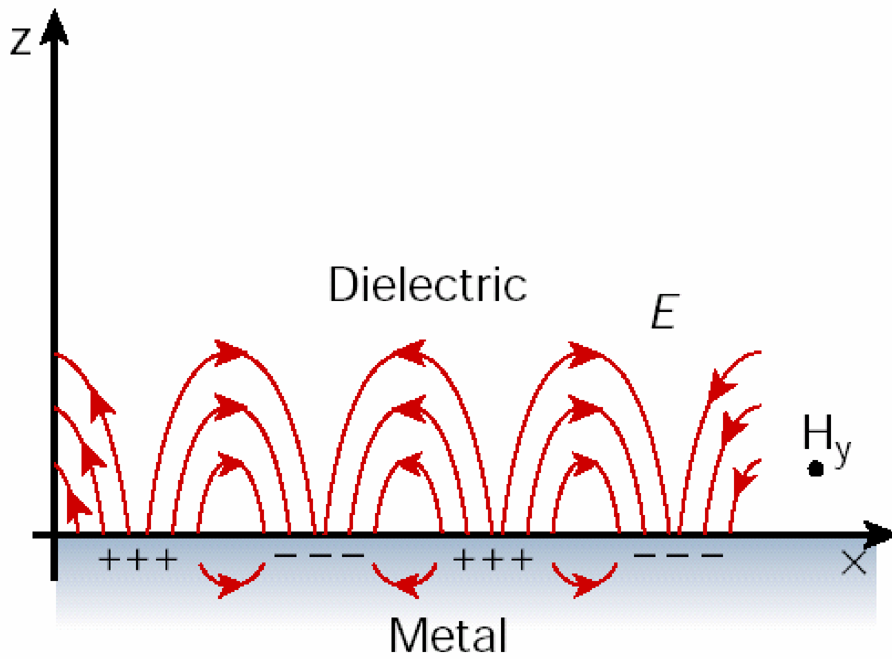

Fig. 1 The surface plasmons between a metal and a dielectric material.

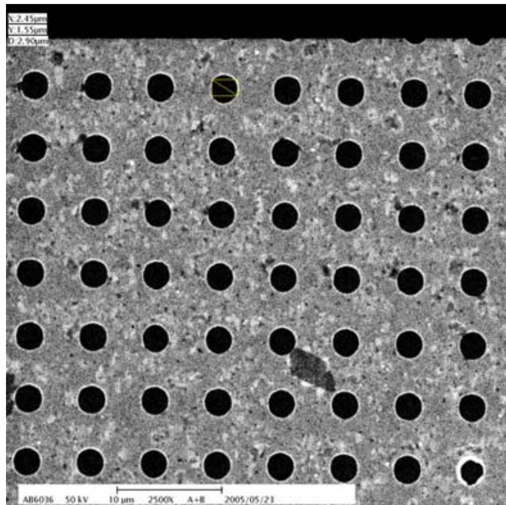

(a)

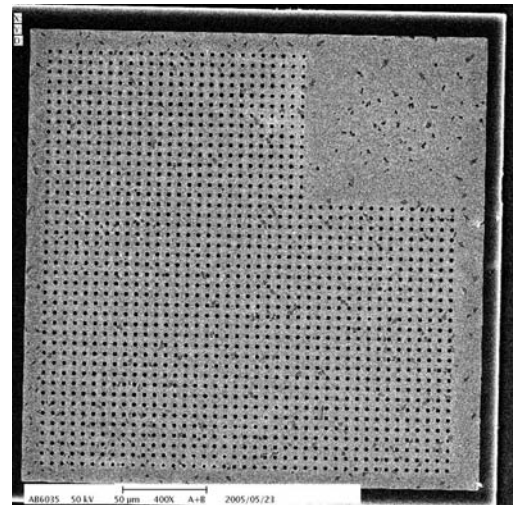

(b)

Fig. 2 The top view of the mesa surface pattern (a) and (b) are 3 μm apertures with 6 μm period.

B. 研究方法

We will divide detector structure into two parts in this section. One is the structure of wafer. The other is the surface structure on the mesa.

The sample was grown by molecular beam epitaxy on a semi-insulating GaAs substrate. The sample structure has a 10000 Å bottom contact, a 3-period superlattice on the bottom layer, a

3000 Å barrier layer ($Al_{0.28}Ga_{0.72}As$), another 45-period on the top layer, and a 8500 Å $Al_{0.32}Ga_{0.28}As$ on the top contact layer. Each period of the bottom superlattice consists of 65 Å GaAs well and 35 Å undoped $Al_{0.32}Ga_{0.28}As$ barrier, but the well is modulated doped with 1×10^{18} $cm^{-3}$of Si in sample. We only doped in the middle well in each three quantum well.

In order to show the design principles, we have to know the operation mechanism on our sample. Figure 3 shows the theoretical band structure of our sample. The band structure is estimated by the transfer matrix method with taking into account the band-nonparabolicity.

In our sample, the top superlattice has two minibands. The first miniband is estimated to range between 48 *meV* and 60 *meV*. The second miniband is estimated to range between 182 *meV* and 242 *meV*. Therefore, the corresponding absorption wavelengths are 6.39 μm to 10.16 μm. The bottom superlattice also has two minibands. The first miniband is estimated from 50 *meV* to 58 *meV*. The second miniband is estimated to range from 189 *meV* to 230 *meV*. Consequently, the corresponding absorption wavelengths are 6.89 μm to 9.46 μm.

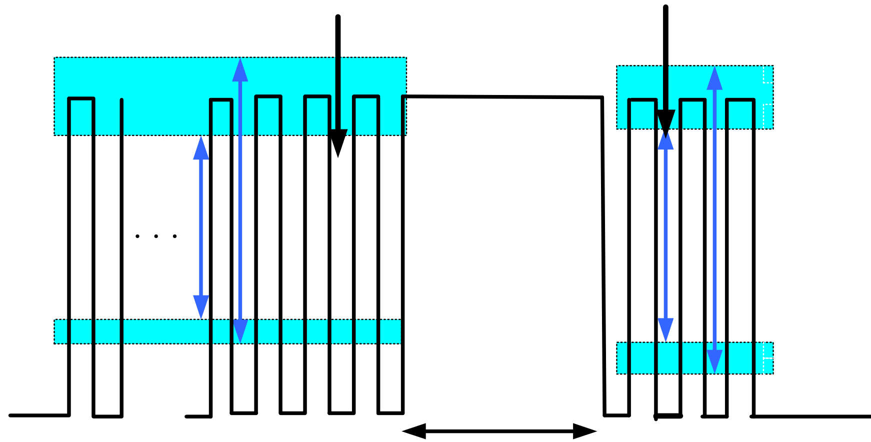

Fig. 3 The band diagram of our sample

In order to achieve optical coupling for normal incidence, we design some grating structures on the mesa. Figure 4 shows SEM image of the grating structure on the mesa. The gratings and contact consist of Au. We manufacture three different period grating structures, including 6 μm, 9 μm, and 12 μm. The trench width in all samples is 3 μm.

Doped with 1×10^{18} cm^{-3} (
period of each three perio

The operational mechanisms are shown in Figure 5. Under positive bias voltage, the photoresponse corresponds to the miniband transition in the bottom SL. The photoelectrons in the second miniband of bottom SL can tunnel through the barrier due to the applied voltage on the blocking layer. Those escaped photoelectrons leave a positive field to attract electrons from bottom contact and therefore the photocurrent in the external circuit is formed. On the contrary, the photoelectrons in the top SL are drawn to top contact, and the left positive field attracts electrons from top contact. This is an internal current circulation which can not be metered by

242meV

182meV

6.39~10.16
um

external circuit. On the other hand, the photoresponse under negative voltage is attributed to front SL.

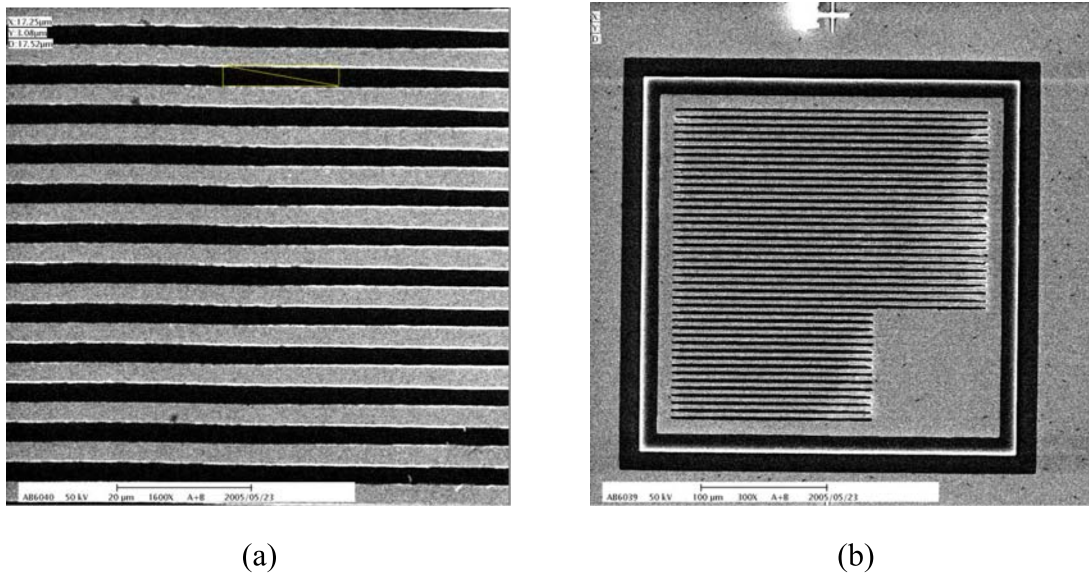

(a) (b)

Fig. 4 The top view of the mesa surface pattern : (a) and (b) are 3 μm trenches with 6 μm period..

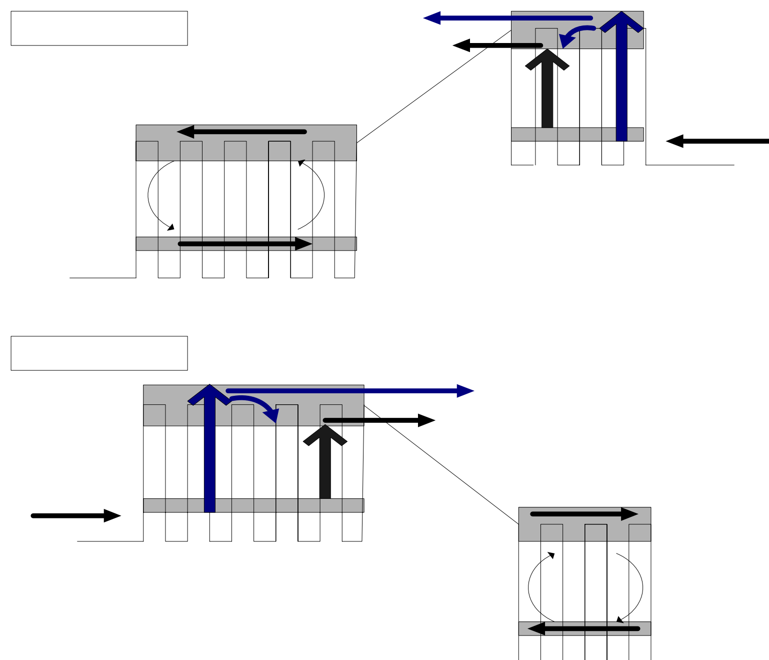

Fig. 5 Schematic illustrations of operational mechanisms at positive and negative bias.

In order to have the electric field for perpendicular direction, the gratings on the mesa deflect the incoming light away from the direction normal to the surface. Figure 6 shows the diagram. The samples have different open air fraction on the mesa. Their open air fractions are 25%, 33%, and 50% individually. We will discuss the three cases later.

Positive Bias

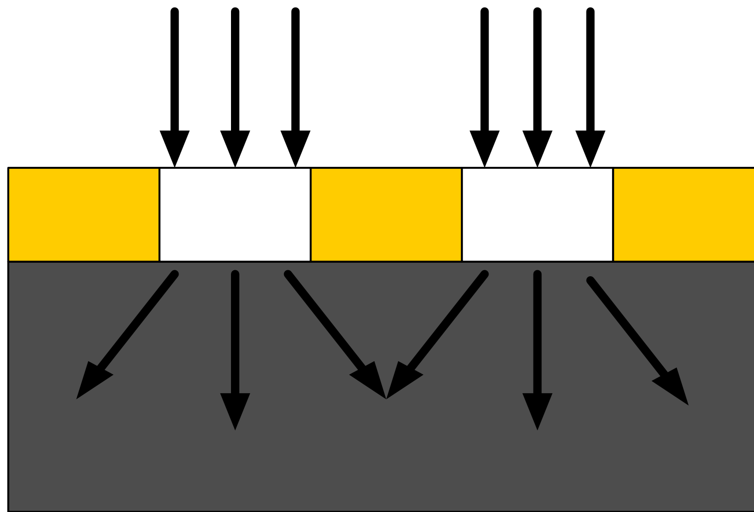

Fig. 6　The gratings deflect the incoming light away from the direction normal to the surface.

C. 結果與討論

1. Sample with 45-degree facet coupling

The photoresponse of sample without grating under high bias is shown in Figure 7 and Figure 8. The operational mechanisms are described above as shown in Figure 5. The response is dominated by short wavelength transition at low bias voltage and shifts to long wavelength as voltage increasing. The long wavelength responsivity is suppressed when the detector is operated at low bias condition. It is because the energy barrier of blocking layer is higher than the bottom state of second miniband minimum and therefore the photoelectrons in the bottom state of second miniband minimum cannot tunnel through the barrier at low bias level.

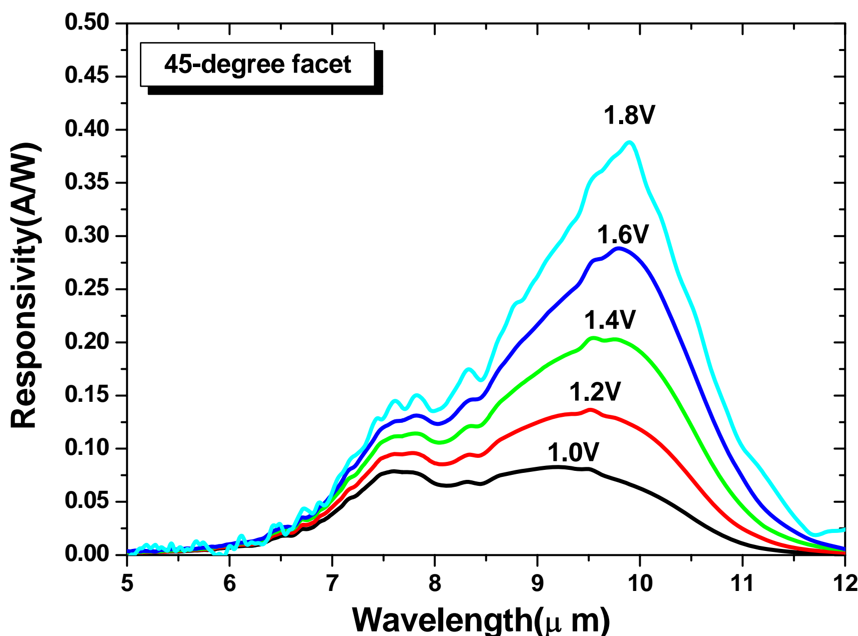

Fig. 7　The spectral response of sample with 45-degree facet coupling under high positive bias at 12K.

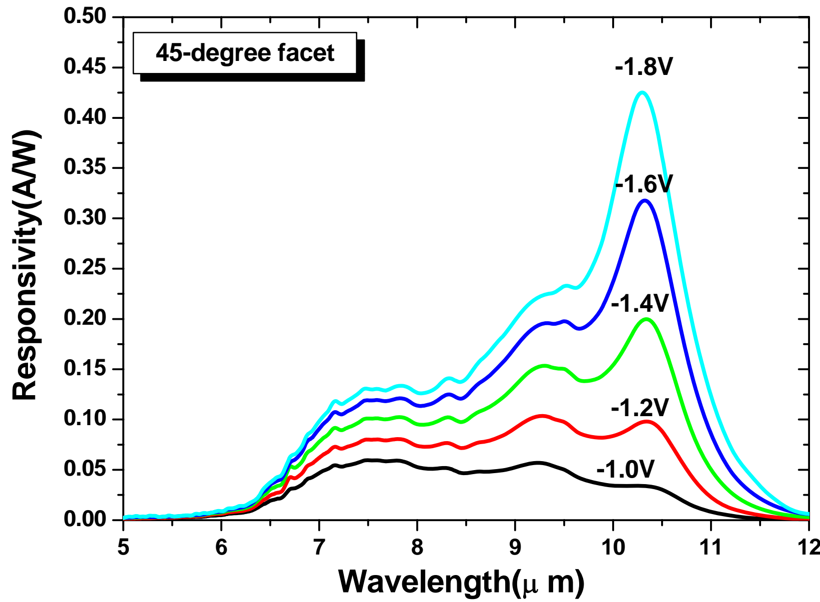

Fig. 8 The spectral response of sample with 45-degree facet coupling under high negative bias at 12K.

2. Samples with grating structure

The photoresponse of different surface period structure will be shown in this section. The light is normal incident on our samples. First, we introduce the sample which trench width is 3 μm and period is 6 μm. In the following section, we will call the sample L33 for short. Figure 9 and Figure 10 show the responsivity of L33. In Figure 9, the peak positions are at 7.6 μm, 8.3 μm, 8.65 μm, 9.3 μm, and 10 μm. The main peak of 10 μm is due to 3-period superlattice. In Figure 10, the peak positions are at 7.6 μm, 8.3 μm, 8.65 μm, 9.3 μm, and 10.3 μm. The main peak of 10.3 μm is due to 15-period superlattice. In the Figure 11, the responsivity varies from different polarization light. The TE (electrical field is perpendicular to trench) responsivity is larger than TM (electrical field is parallel to trench) responsivity. This is because TE light has larger electrical field fraction in perpendicular direction after the light is diffracted by gratings. Owing to the selection rule, the TE light has better performance than TM light.

The sample of trench width 3 μm and period 9 μm is called L36 for short. Figure 12 and Figure 13 show the responsivity of L36 under high bias. The peaks of L36 and L33 are at the same position. In the Figure 14, the TE responsivity is also larger than TM response. Finally, the sample which trench width is 3 μm and period is 12 μm is called L39 for short. The performance of L39 is similar to L33 and L36. Figure 15 and Fig. 16 show the responsivity of L39. Figure 17 shows the difference between the TE light and TM light. Although TE response is lager than TM response in all sample, the different value between the TE light and TM light vary with period. We will discuss the phenomenon in next section.

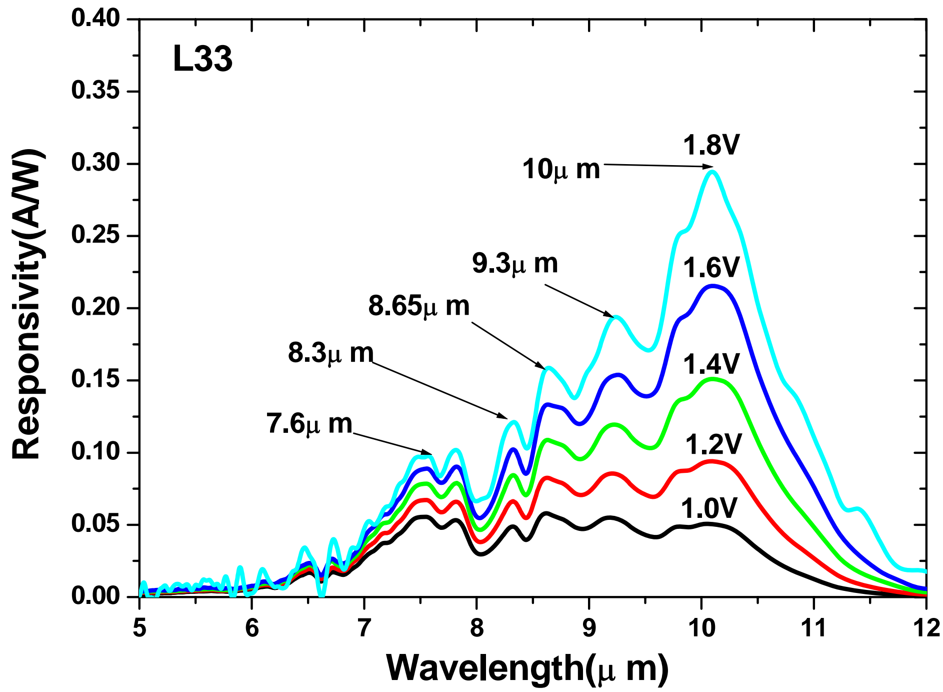

Fig. 9 The spectral response of L33 under high positive bias at 12K.

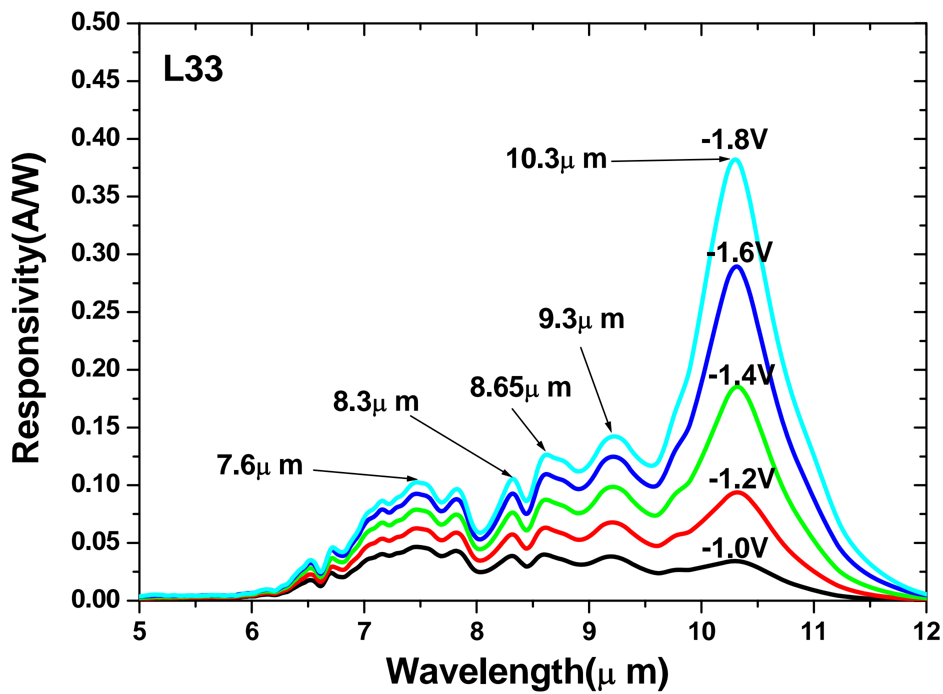

Fig. 10 The spectral response of L33 under high negative bias at 12K.

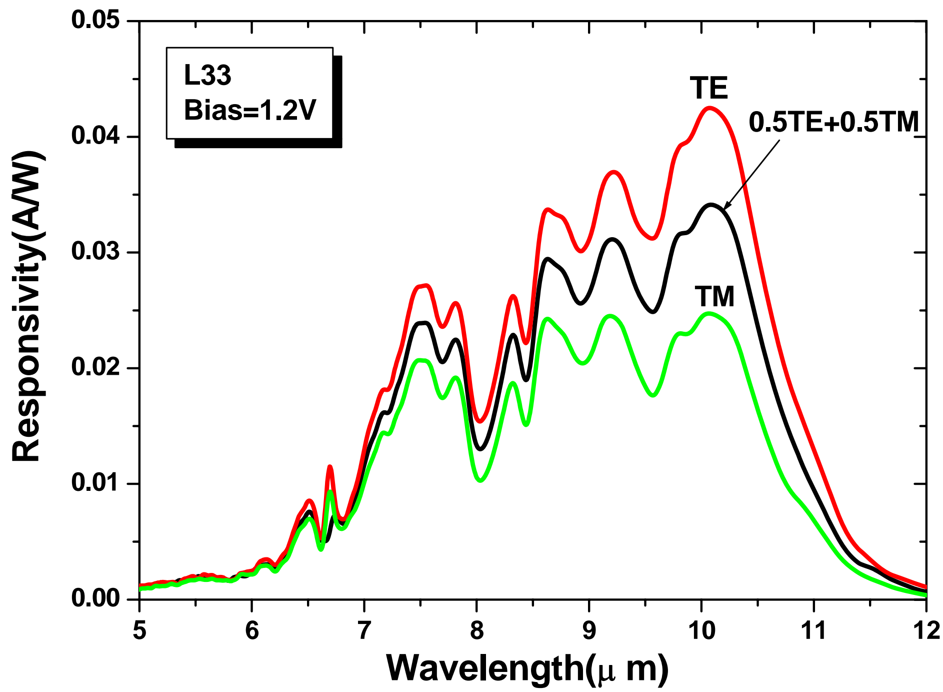

Fig. 11 The spectral response of L33 under TE and TM polarization.

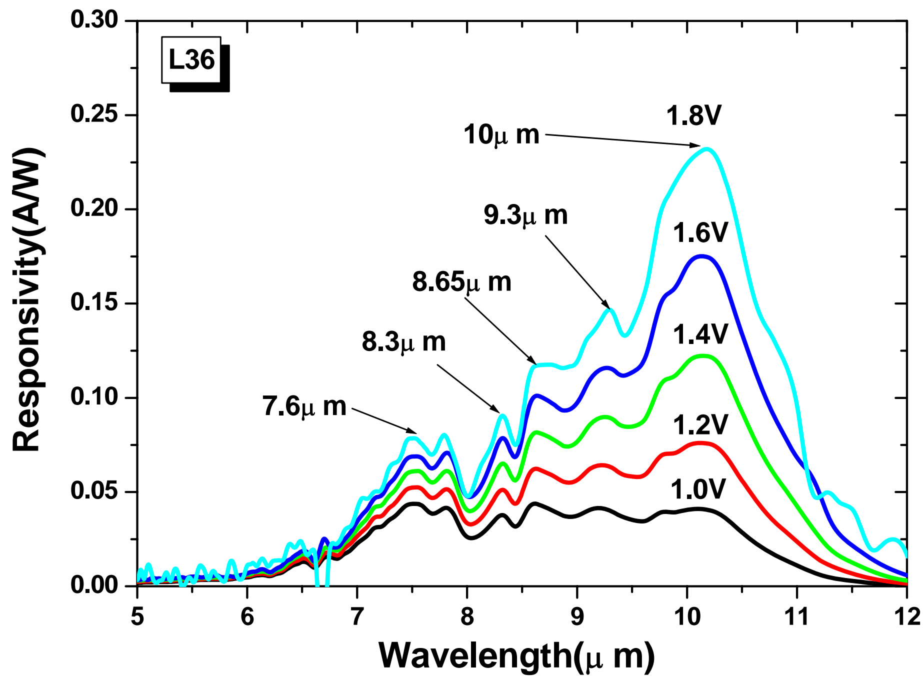

Fig. 12 The spectral response of L36 under high positive bias at 12K.

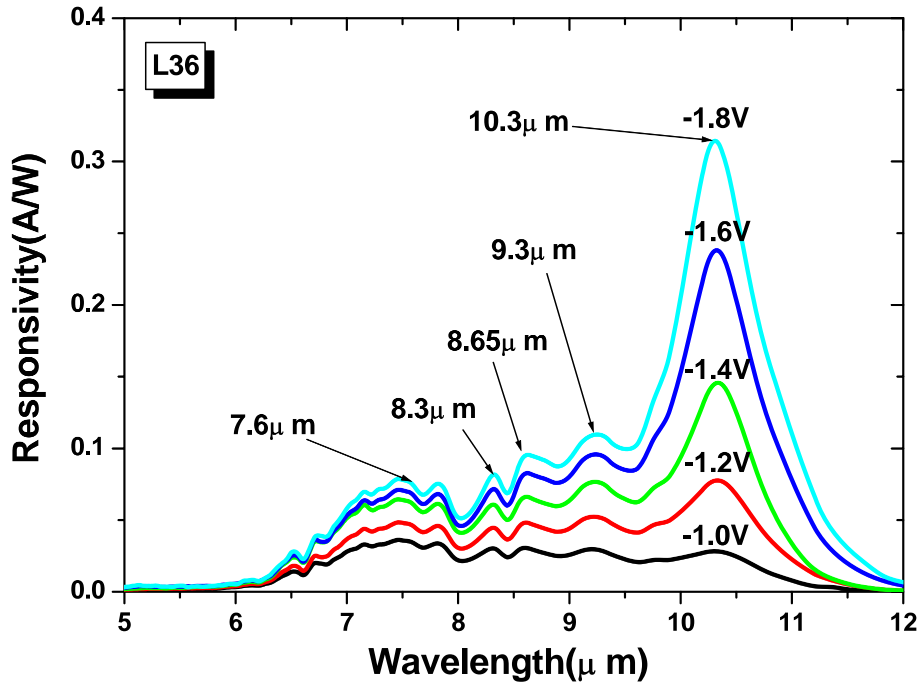

Fig. 13 The spectral response of L36 under high negative bias at 12K.

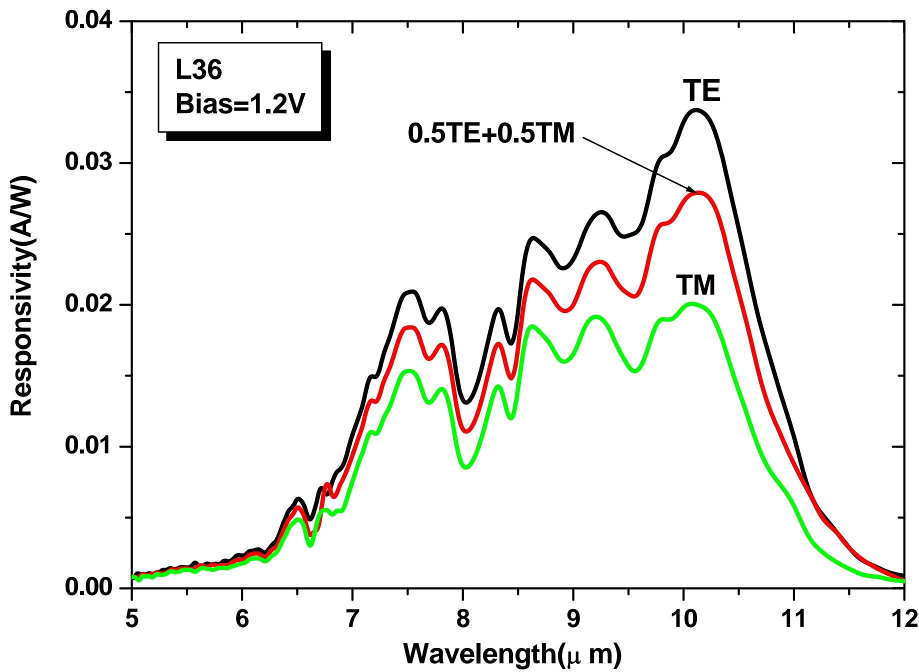

Fig. 14 The spectral response of L36 under TE and TM polarization.

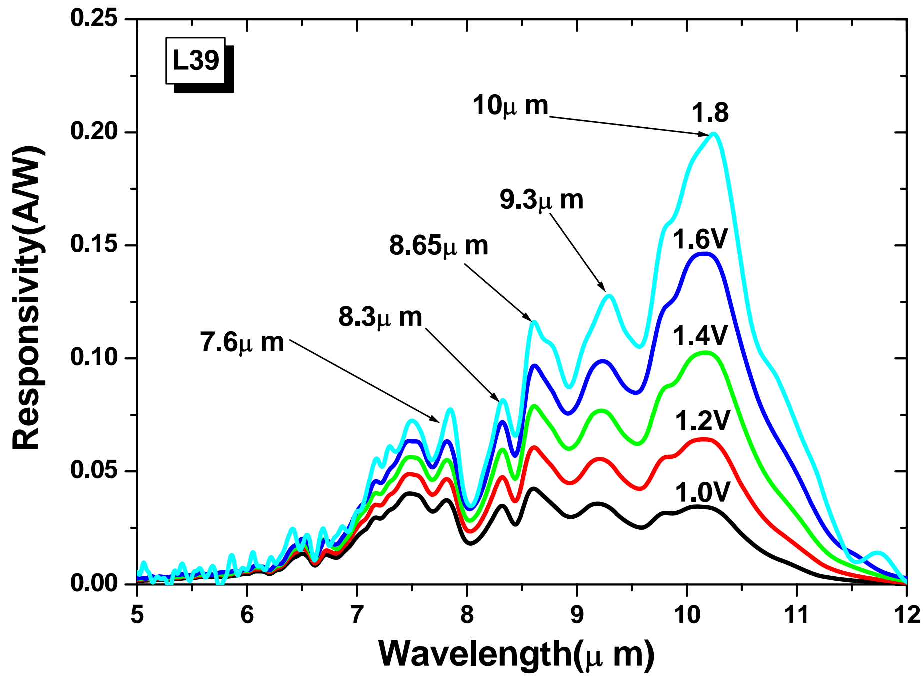

Fig. 15 The spectral response of L39 under high positive bias at 12K.

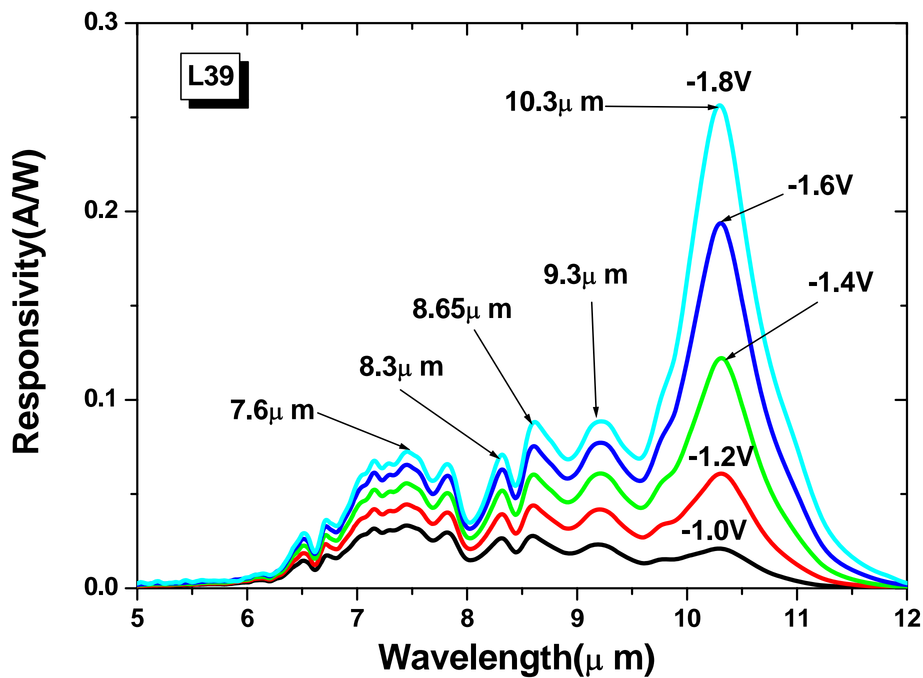

Fig. 16 The spectral response of L39 under high negative bias at 12K.

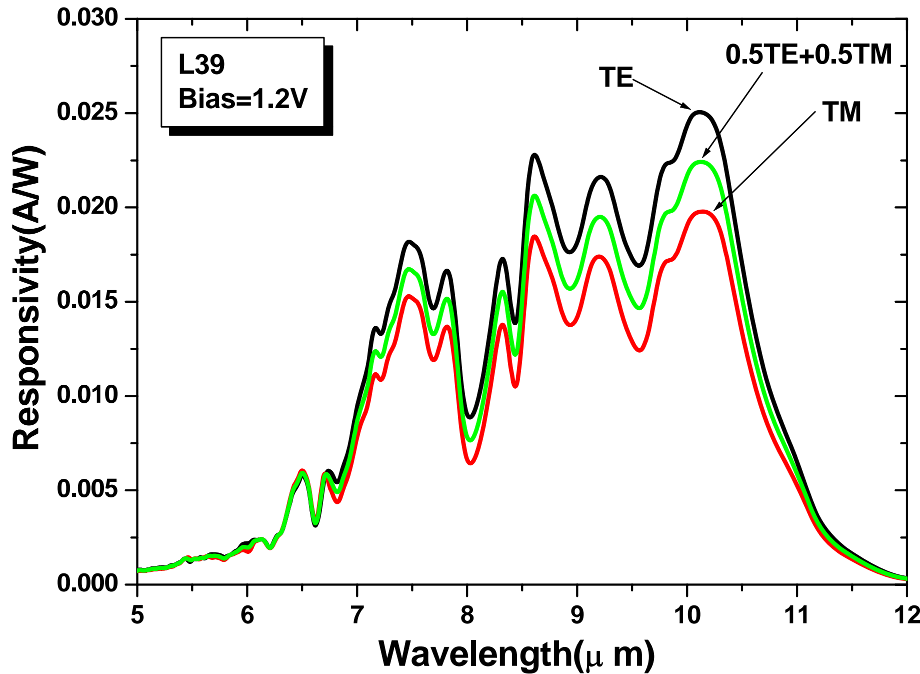

Fig. 17 The spectral response of L39 under TE and TM polarization.

3. Discussion

(1) Polarization

In the Figure 18, the response of TM light should be zero theoretically, because the TM light which is diffracted by gratings has the electric field always paralleled with the surface. However, no matter how we change the direction of polarization, the response of TM light is not zero. Figure 19 shows the spectral response of L36 under different polarization. When polarization is 45-degree, the responsivity reaches maximum. Therefore, the light with 45-degree is called TE mode. On the other hand, the light with 135-degree is called TM mode. Although TM response is minimum, it is not zero. This is because edge light coupling produces response of TM mode, and we will discuss this phenomenon in the next section.

(2) Edge Light Coupling

The TM light absorption comes from edge light coupling. The device without any surface structure is measured in two different ways. One is the 45-degree facet light coupling and the other is normal light incident. The experiment of edge light coupling is shown in Figure 20. In the Figure 21, the response of edge light coupling for normal incident is about half of 45-degree facet coupling. By experimental data in Figure 21, we realize that the edge light coupling has great influence on our sample.

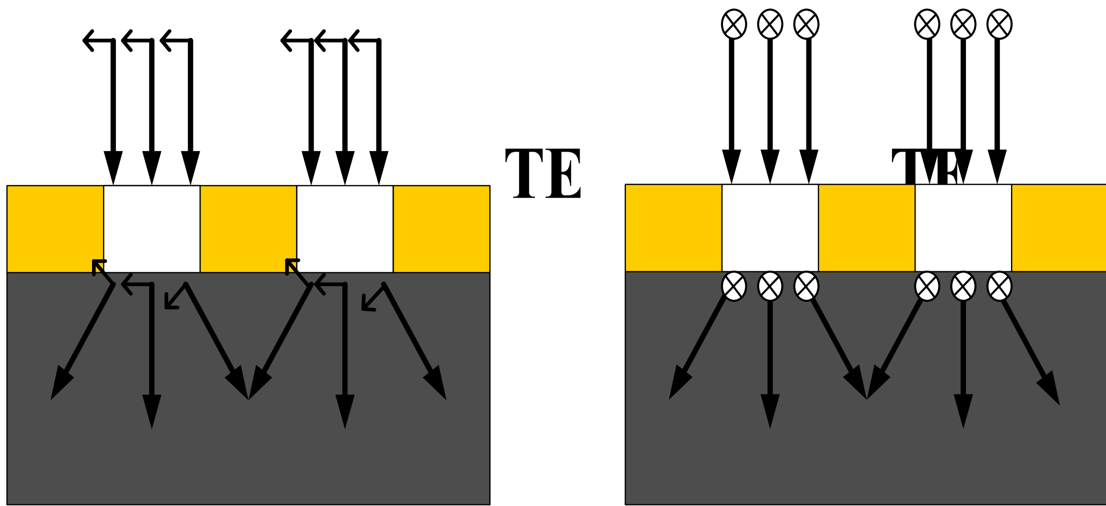

Fig. 18 The refraction of TE and TM light

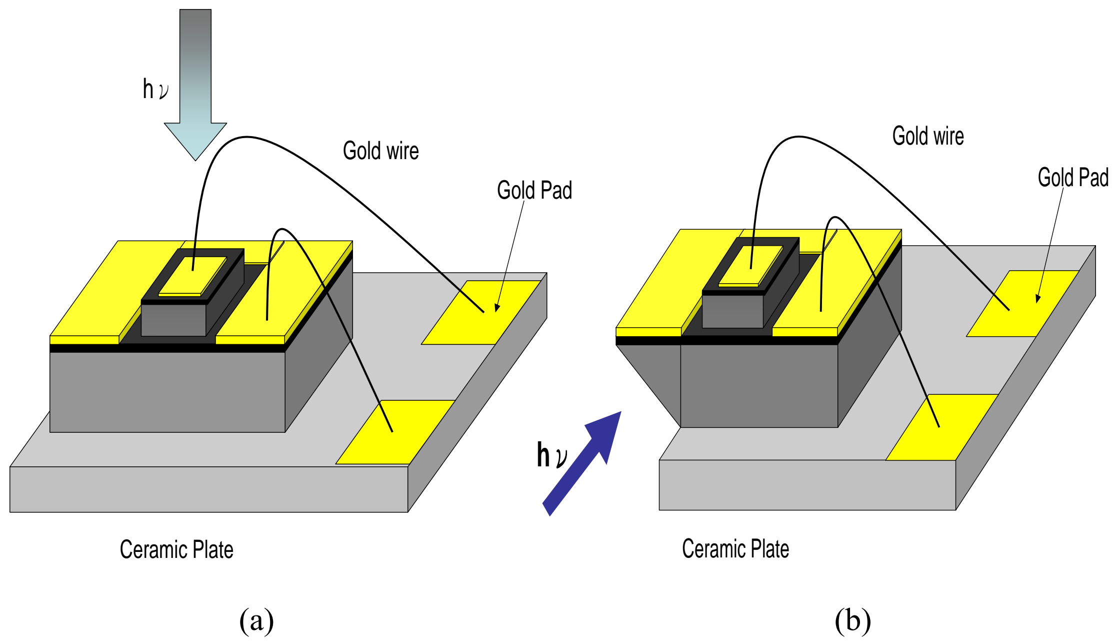

(a) (b)

Fig. 19 Experiment of edge light coupling (a) edge light coupling for normal light incident (b) 45-degree facet coupling

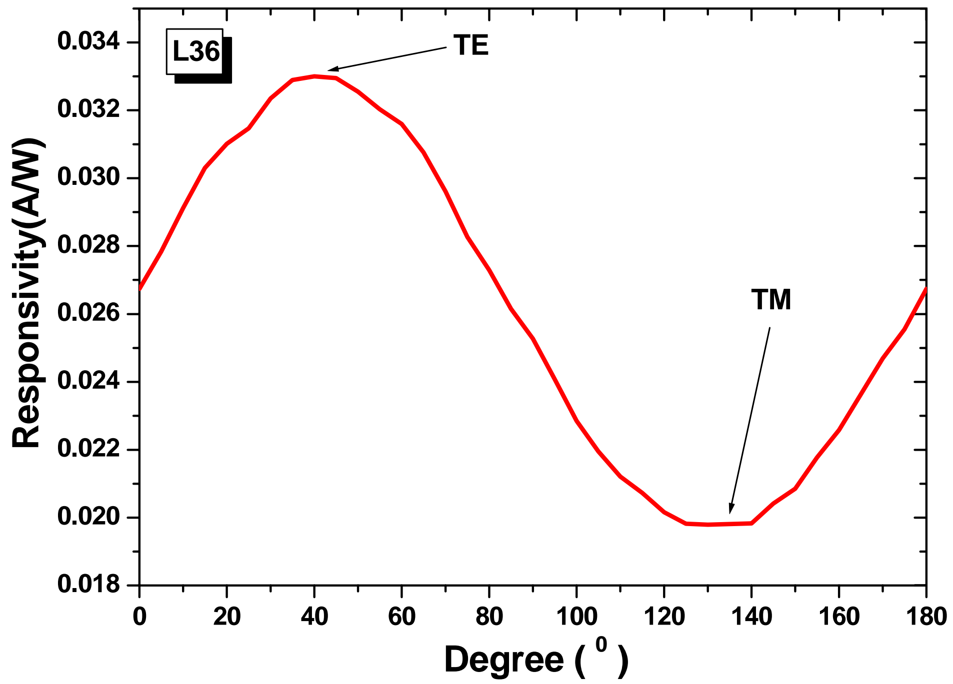

Fig. 20 The spectral response of L36 under different polarization.

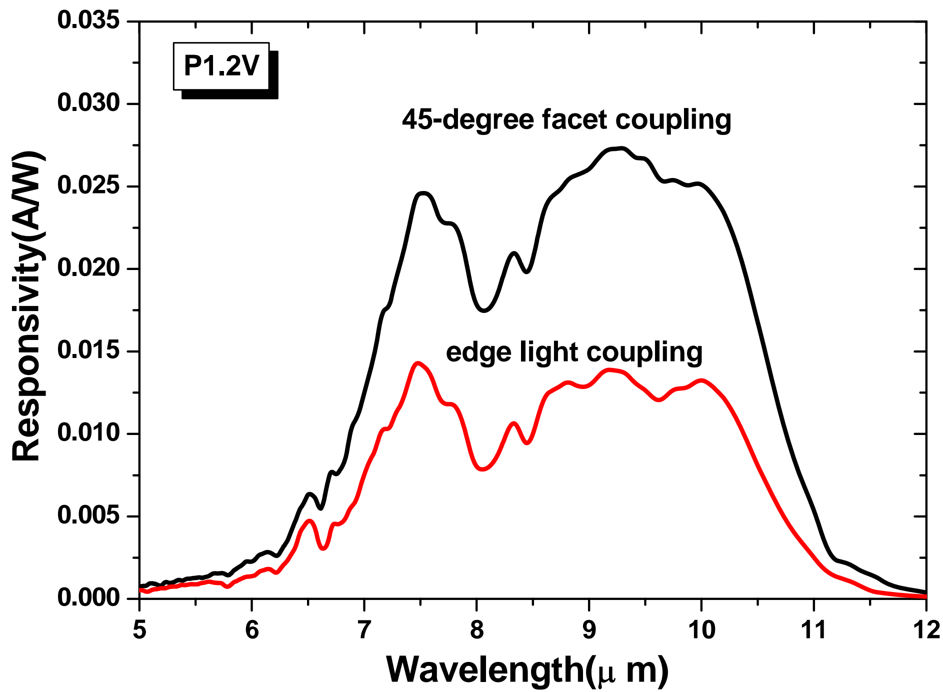

Fig. 21 The response of 45-degree facet coupling and edge light coupling.

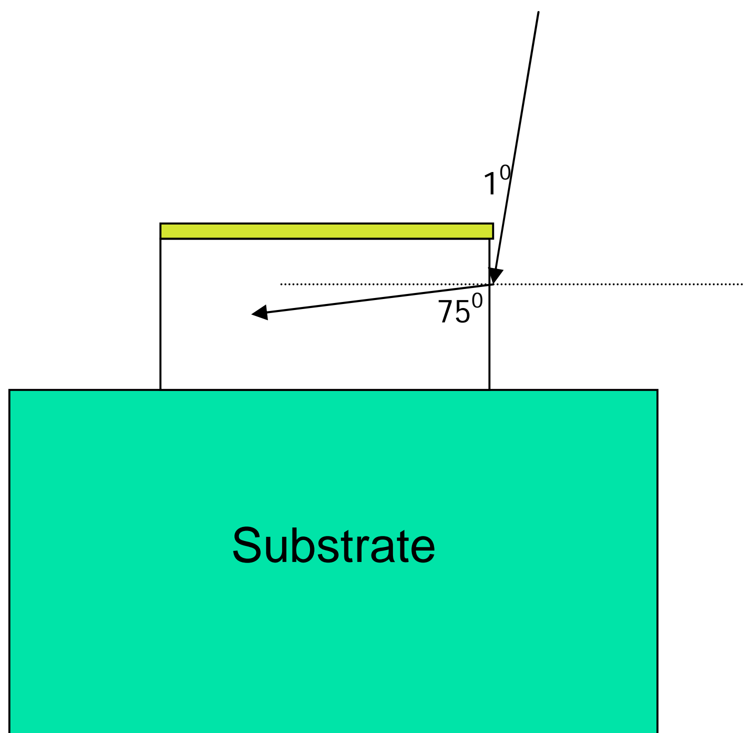

Fig. 22 The edge light coupling scheme.

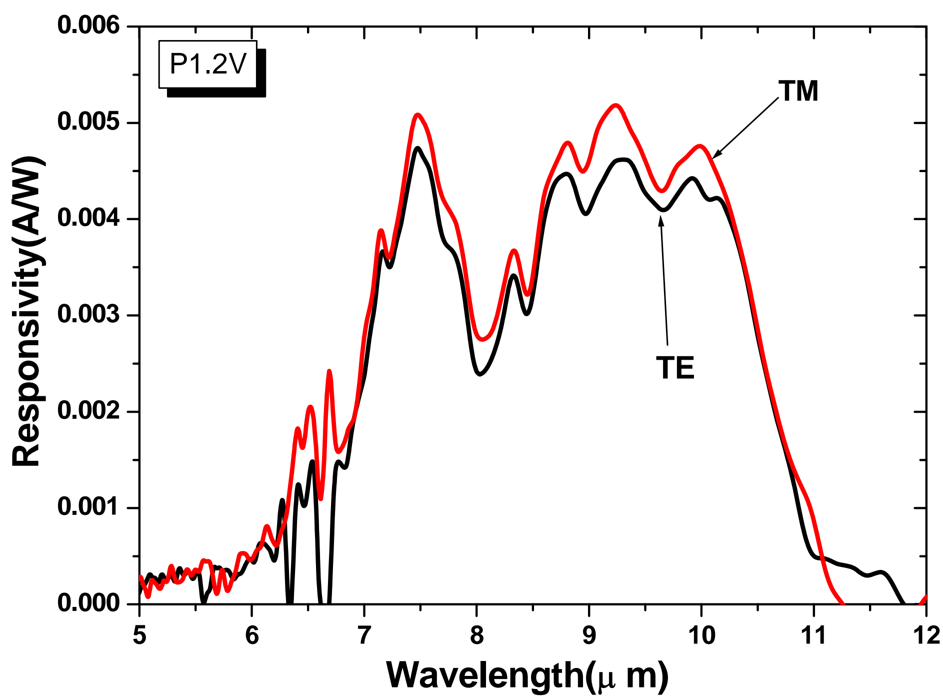

Fig. 23 The spectral response of edge light coupling under different polarization.

Figure 22 shows the edge light coupling scheme. When the light is incident with 1-degree, the refraction angle can be calculated by Snell's Law.

$$n_1 \sin\theta_1 = n_2 \sin\theta_2 \qquad (1)$$

The refraction angle is 15-degree. Therefore, the refraction light has large fraction of electrical field which is perpendicular to the superlattice plane. This is why the TM light can be absorbed by our device. In Figure 23, the response does not change too much no matter what the polarization light is incident. This is because the photoresponse is from edge coupling light of the mesa edge. Consequently, the light coupling efficiency depend on mesa height and mesa shape. As the mesa height is deeper, the response can be observed more obviously.

(3) Response with different period grating

The introduction of surface plasmon is discussed previously. Figure 24 shows the transmission of our sample. Because the wavelength is longer than trench width, the transmission decays as the wavelength increase theoretically. However, there is a 9 μm peak in L33 device. It is attributed to the surface plasmon between the *GaAs* and metal. The peak in L36 device is at 13.5 μm, and it is not in the detection region. The plamon peak is not as sharp as other papers. This is because the mesa size is only 300 μm× 300 μm. There are only twenty five slips on the mesa of L33. Therefore, the transmission enhancement by surface plasmon is not obvious.

The TM response is due to edge light coupling and the TE response is caused by edge light coupling and grating structure. In above section, we have described that TE response is equal to TM response in the edge coupling part. Therefore, the total TE response minus the total TM response leaves response of grating structure. Figure 25 shows the response of grating structure. The shape of L39 in Figure 25 is similar to the P1.2V response in Figure 7. This result is expected by transmission in Figure 24, because the transmission spectrum of L39 in long wavelength is flat. In L36 case, the transmission rises when wavelength is longer than 8 μm. Therefore, the response of L36 is sharper than L39 at long wavelength. There is a 9 μm peak in L33 case. We can observe the phenomenon in Figure 25. The response of L33 is larger than L36 in 8.5 μm ~ 9.5 μm region in Figure 25. Figure 26 shows the diagram of responsivity vs. open air fraction at different wavelength. The short wavelength response does not match with the transmission spectrum, because of the low group velocity and relaxation. By dispersion relation, the group velocity of short wavelength is slow, and the relaxation effect will be serious. Therefore, the responsivity saturates under high open air fraction.

(4) Quantum efficiency and diffraction angle

The internal quantum efficiency for unpolarized light is given by

$$\eta_i = \frac{1}{2}\{1 - \exp(-1.62910^{-4} \times N_d \times W \times s \times N \times Sin^2\theta)\} \qquad (2)$$

where $\boldsymbol{N_d}$ is doping density, $\boldsymbol{W}$ is well width, $\boldsymbol{S}$ is number passes, θ is incident angle.

Therefore, the internal quantum efficiency calculated from Eq. (2) is 0.03.
The external quantum efficiency is given by

$$\frac{0.738}{A_{eff}}\eta_i = \eta_{ext} \tag{3}$$

The external quantum efficiency of 45-degree facet coupling is 0.01566. Because the response is proportional to external quantum efficiency, we can obtain the external quantum efficiency of L39. The external quantum efficiency of L39 is 0.02. The internal quantum efficiency of L39 calculated from Eq. (3) is 0.027. Therefore, the diffraction angle is derived by using Eq. (2). The diffraction angle of L39 is 67-degree. By the same method, the diffraction angle of L33 and L36 are 68-degree and 67-degree.

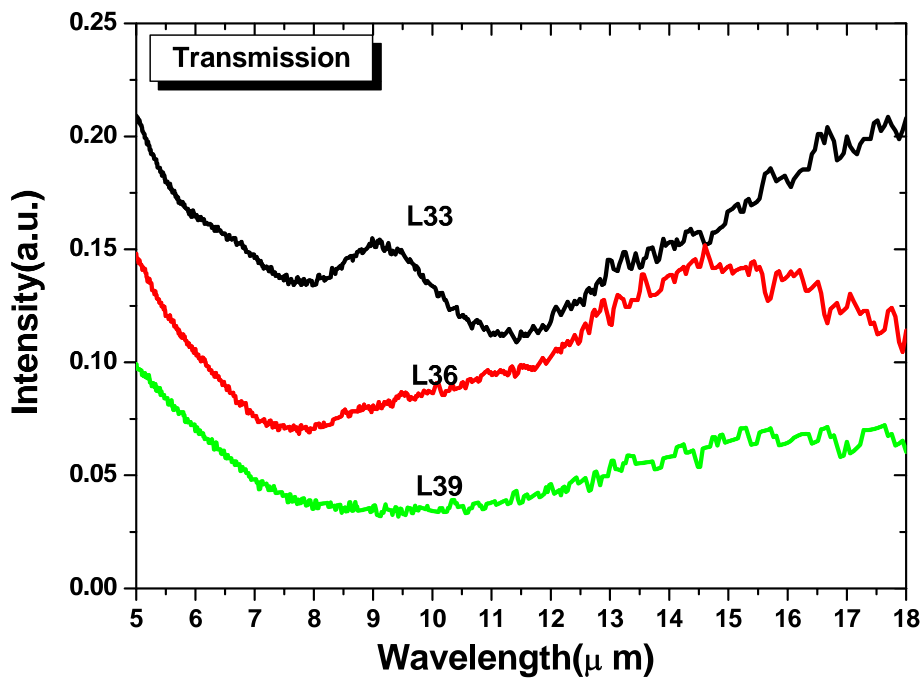

Fig. 24 The transmission of L33, L36, and L39

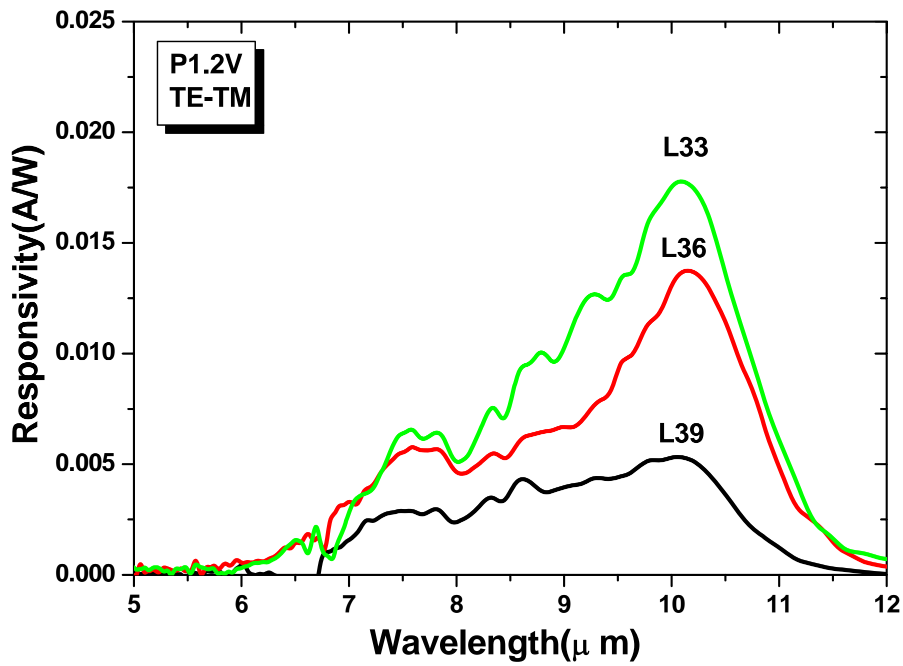

Fig. 25 The response come from grating structure.

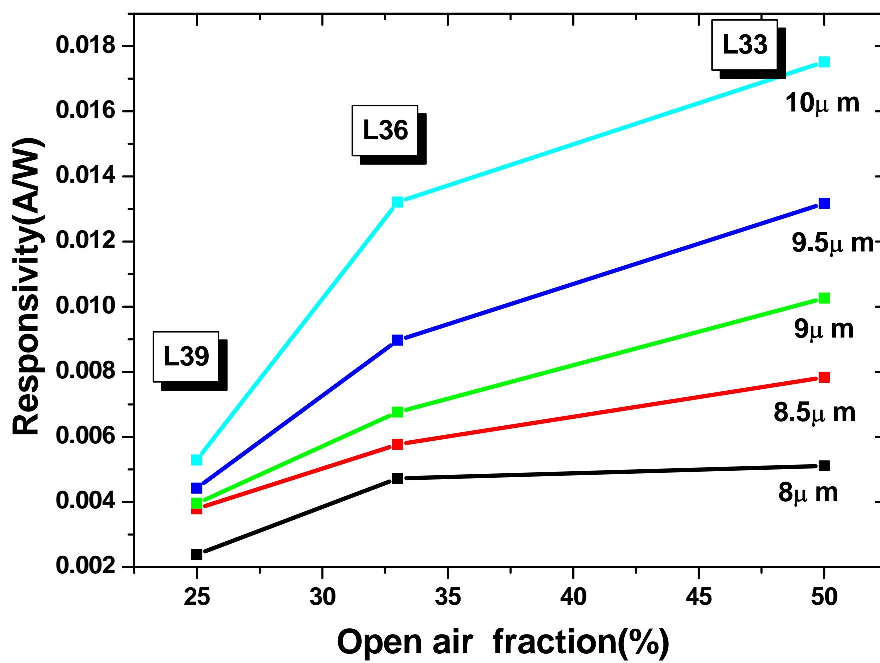

Fig. 26 The responsivity vs. open air fraction

D. 結論與計畫自評

In this project, superlattice infrared photodetectors with gratings for coupling the normal incident light are fabricated and studied. Base on this structure, response shape is tunable due to surface plasmon. We focus on the response of different open air fraction and compare the response with transmission.

The experiment results show that grating structure can effectively couple the normal incident light for topside-illumination and the response is affected by surface plasmon in L33 structure. By means of the experiment demonstration, the TM response is due to edge light coupling and the TE response is caused by edge light coupling and grating structure. The detectors with grating have good IR absorption spectrum of TE polarization. The transmission is enhanced by surface plasmon. There is a plasmon peak in the detection region. This is why the response shape is tunable. Thus, the applicability of the grating structure coupling is verified.

There are some options to improve the present work:

(1) In order to achieve the plasmon peak in our detection region, we can try to use different trench width or period of grating structure.

(2) The metal thickness can be optimized to enhance the plasmon peak.

(3) We can change the mesa size to increase the amount of trenches on the mesa.

(4) The diffraction effect caused by the grating should be studied further to enhance the coupling efficiency.

E. 參考文獻

[1] 1 J.A. Porto, F.T. Garcia-Vidal, and J.B. Pendry, *Phys. Rev. Lett.* **83**, 2845 (1999).

[2] L. Martin-Moreno, F.J. Garcia-Vidal, H.J. Lezec, K.M. Pellerin, T. Thio, J.B. Pendry, and T.W. Ebbesen, *Phys. Rev. Lett.* **86**, 1114 (2001).

[3] Q. Cao and P. Lalanne, *Phys. Rev. Lett.* **88**, 057403 (2002).

[4] U. Schröter and D. Heitmann, *Phys. Rev. B* **58**, 15 419 (1998).

[5] E. Popov, M. Nevière, S. Enoch, and R. Reinisch, *Phys. Rev. B* **62**, 16100 (2000).

[6] H. Räther, *Surface Plasmons on Smooth and Rough Surfaces and on Gratings* (Springer-Verlag, Berlin, 1988).

二、參考文獻

詳見各部分後面所附

三、計畫自評

由於計畫之中包含數個子計畫，計畫自評的段落安排在各個子題目的討論及自評之中，以利於作各個子題目之自評與討論，在此不再撰寫。

附件一：出席國際會議心得

會議名稱：2005 雷射與光電研討會

Conference on Lasers and Electro-Optics 2005 (CLEO 2005)

一、 參加會議經過

CLEO 2005 是每一年都會舉行的光電領域的研討會，今年是在巴爾的摩舉辦，會議的主題包含所有與光電相關的議題，包含：雷射應用，固態雷射，半導體雷射，光儲存技術，非線性光學應用，光學材料與薄膜，超快光學，高場物理，光學元件，生醫應用，先進光學感測，光纖與導波雷射，發光二極體以及量子電子的應用。與會的人士除了包含論文發表者，相關領域研究人員還有全美所有重要的光電廠商。會議進行除了一般的邀請演講，口頭及壁報論文的發表，還有就是以廠商展示新商品為主的類似光電展的盛會。

會議一共進行六天的時間，參加的人數有四，五千人之多，參與的廠商也有三百多家，發表的論文超過兩千篇，所以每天都有不同主題的論文發表，和大會安排的邀請演講。中間三天有大會安排的廠商光電商品展，是我覺得整個會議最有看頭的部分，偌大的會場擠滿了各式各樣的光電產品，處處都有令人驚奇的發現。

這次大會特別為學生安排了一系列的活動，我覺得也是相當值得參加的。包括了學生論壇，請一些學者參與學生的早餐或午餐會分享經驗，還有教學生一些發表科學論文的方法，以及提供了許多工作或實習的機會讓大家參與等等。

我的壁報論文被安排在第四天的中午發表，我的研究主題是以超晶格紅外線偵測器為主，並向大家介紹我們在低電壓操作下的努力成果，在發表的過程中也結識了一些與自己領域相關的學者專家，互相討論的結果深深讓我覺得受用無窮。其他的時間我則是選擇一些有興趣的主題論文發表參與或參加上述的學生專屬活動。

二、 與會心得

由於是國際性的光電盛會，所以在參加會議的過程中，可以不斷的吸收有關光電領域的最新發展與最新知識。我這次有幸以壁報論文被接受而參與此次盛會，得以站在這個國際性的殿堂與全世界的光電工作者一起參與其中，感到十分榮幸。除了一般會議都有的邀請演講，請到的都是各領域大師級的人物外，其餘的論文發表也讓我對於光電領域的深度與廣度有了新的一番認識。

雖然大多數的主題和我所做的題目並不相關，但可以藉此瞭解各領域的發展，並得知科技進步的程度，也是令人難忘的經驗。尤其是來自世界各地的廠商無不卯足全勁讓大家看到自己公司的最新發展，各式各樣意想不到的雷射產品，光電元件，讓人看的目不暇給，對於科技的發展的進步又有了新的體認。

這次參與會議，對於許多研究團隊都是跨校或甚至跨國際的研究計畫感到驚訝，尤其是看到全世界許多的頂尖學者的合作研究得到了驚人的成果，讓我深深覺得台灣應該要努力走向國際化，才能將視野提升到國際級的水準，雖然台灣現在的研究成果已經在世界上佔有

了一席之地，不過相對來說，我們的國際合作機會並不普遍，也許這是我們以後應該努力的目標，做出更好的研究成果以吸引國際上一流的研究團隊與我們合作。

三、 建　議

相對於我們一般在國內參與的所謂國際性的研討會大多都是台灣研究團隊參加，國外的研討會所提供的深度與廣度確實不是國內研討會可以相提並論的。在這樣國際性的舞台之上，雖然也看到了不少台灣人參與其中，可是也希望有朝一日台灣可以自行舉辦類似規模的研討會，一方面可以讓我們參與會議者可以免除舟車勞頓之苦，也可以提升台灣的國際能見度。

現今國家政府財政並不寬裕，所以補助學生的款項並不充足，雖然我此次有幸承蒙教育部補助，但金額連機票都不夠，對我們這些參與會議的學生而言，出過開會不啻為沈重的經濟負擔，也許以後學校可以以類似助學貸款的方式先行補助學生的出國費用，待以後再慢慢償還。出國開會對學生與國際學者接觸是很重要的，除了可以加強自己的外語能力，也可以證明自己的研究成果足以站在世界的舞台，對自己也是一種肯定。如果可能的話，希望能將補助金額提高，或尋求相關的解決方式，以減輕學生的經濟壓力。

四、 攜回資料名稱及內容

大會會議相關資訊，所有發表論文的光碟，光電廠商具參考價值之廣告文宣，與相關研究者之通訊資料等。

五、 其　他

無

附件二：出席國際發表論文

Low-Voltage Operation Photodetector Made by Coupling Superlattice and Quantum Wells

J. H. Lu[1], **Y. C. Wang, C. L. Wang, C. H. Kuan**[2]

Graduate Institute of Electronics Engineering and Department of electrical engineering, National Taiwan University

No.1, Sec. 4, Roosevelt Road, Taipei, Taiwan, Republic of China 10617

[1] *d91943025@ntu.edu.tw* [2] *kuan@cc.ee.ntu.edu.tw*

C. W. Yang, S. L. Tu

Opto Tech Corporation, 1, Li-hsin Rd. V, Hsinchu Science-based industrial Park, Hsinchu, Taiwan, Republic of China

Abstract : We have investigated a novel photodetector structure of coupling superlattice and quantum wells. This device can be operated at low bias range and even the photovoltaic mode. The broadband response is achieved by this structure.

© 2005 Optical Society of America

OCIS codes: (040.3060) Infrared ; (230.5590) Quantum-well devices

1. Introduction

In recent years, the applications such as the focal plane array (FPA) and remote temperature sensing drive the research of novel intersubband transition devices. Some useful characteristics of quantum well infrared photodetector (QWIP) including multicolor, photovoltaic are also investigated [1-3]. In addition to QWIP, the superlattice infrared photodetector (SLIP) is another promising structure to achieve those applications. Compared with the quantum well, superlattice has the properties including low power consumption, broadband photoresponse and voltage-tunable. The performance of SLIP has been proved by our group [4-6]. The perspective of our detector is to operate at low bias, therefore, low power consumption and low dark current are expected. We also hope the operation temperature can be higher and the broadband and flatband spectrum can be observed. Based on our perspective, a new structure of superlattice coupled to quantum wells is designed.

Figures 1(a) and (b) show the band diagrams of our sample under photovoltaic and photoconductive mode, respectively. Under zero bias, the photovoltaic mode, electrons in superlattice excited to the second miniband will go through the barrier by group velocity and captured by some quantum wells. Because of those captured electrons, the potential on superlattice side is relatively positive and the quantum well is negative. Therefore, a built-in potential will exist and the energy band will be bended as shown in Fig. 1(a). On the other hand, due to the dopant migration during the growth process, a built-in electric field is created at the barrier in quantum well structure. Then, electrons in quantum well excited to the bound state or the continuum band can tunnel through the barrier and become the photocurrent. Hence, under zero bias, the photocurrent from superlattice and quantum wells can be measured simultaneously.

For the photoconductive mode, Fig. 1(b) shows our sample operated under negative bias. When operated under

negative bias, this structure works just as the general photodetector. Electrons in superlattice excited by infrared radiation will go through the barrier and be accelerated by the electrical field on the quantum well structure. At the same time, electrons in quantum well can also overcome the barrier and then become the photocurrent. On the other hand, under positive bias, electrons will be attracted to top contact. In the superlattice, the electrons transport to top contact and leave the superlattice a positive electric field. Therefore, electrons will be attracted back to superlattice and become an internal circulation which cannot be detected. So we can measure both the superlattice and quantum well response under negative bias, but under positive bias we can only observe the QWIP response.

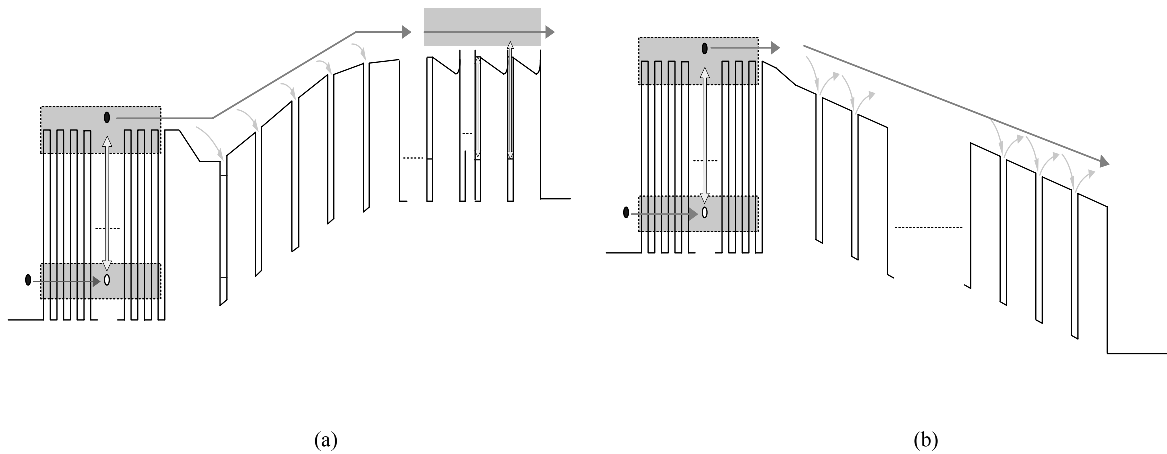

(a) (b)

Fig. 1. The band diagram under (a)photovoltaic (PV) mode and (b)photoconductive (PV) mode of negative bias.

2. Sample Structure

Our sample structure contains a 15-period superlattice, a 60 nm graded barrier and a 50-period quantum well. Each period of the quantum well consists of 6nm GaAs well and 50nm undoped $Al_{0.21}Ga_{0.79}As$ barrier and each period of superlattice consists of 6nm GaAs well and 4nm undoped $Al_{0.29}Ga_{0.71}As$ barrier. The superlattice and quantum well structure are both doped with Si for $4x10^{17}$ cm^{-3}. The absorption wavelength of superlattice we designed is 6~10 μm, and the transition type for quantum well is bound to continuum and the longest absorption wavelength is 11.7 μm.

3. Experimental Results and Discussions

Figures 2(a) and (b) are the photoresponse under photovoltaic mode at low temperature and high temperature, respectively. The cause of the photovoltaic response from superlattice and quantum well are group velocity and the dopant migration, respectively. Because the photovoltaic spectrums are measured under open-circuit condition by voltage amplifier, the vertical axis in both figures is the relative voltage amplitude. Three peaks can be distinguished from the spectrum. One short wavelength peak is at 6.5 μm from superlattice and the other two attributed to the quantum wells are located at 9.2 μm and 11.5 μm. As temperature rising, the superlattice response is steady enhanced, while the quantum well response is gradually diminished. From Fig. 2(b), the superlattice response reaches the maximum at 60K. At high temperature, due to the phonon scattering increases, the relaxation process in quantum wells becomes more serious, so the quantum well response is almost disappeared. The arrows in both figures show the trend of the superlattice response.

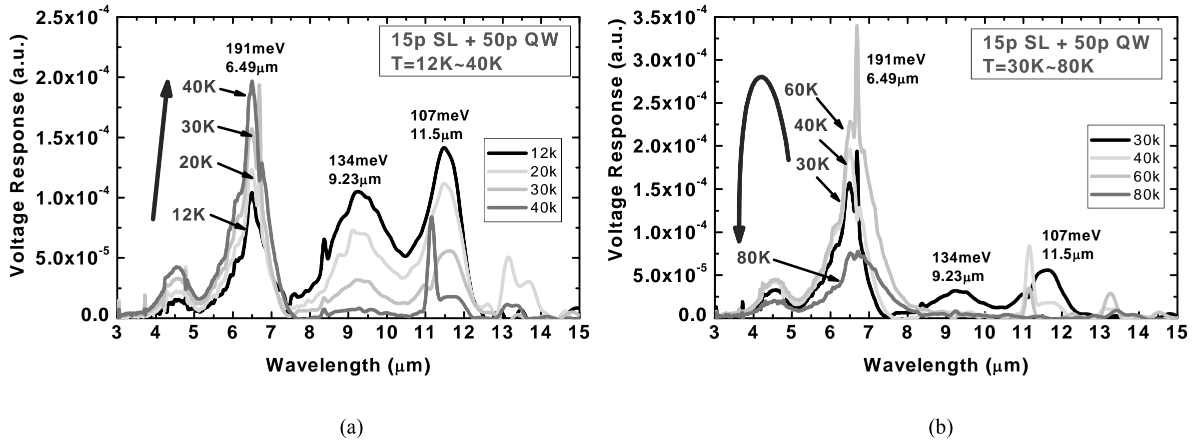

(a) (b)

Fig. 2. The photovoltaic response under (a)low and (b)high temperature. The arrow shows the trend of the superlattice response as temperature changing. The response from QWIP is gradually reduced as temperature rising.

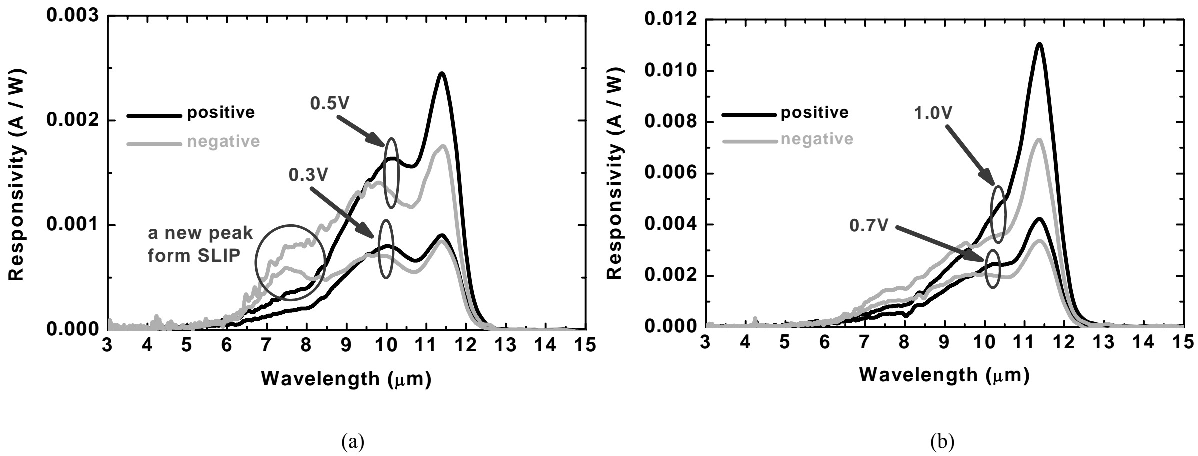

(a) (b)

Fig. 3. The comparison of responses at 12K under negative bias to those under positive bias at (a)0.3V and 0.5V, (b)0.7V and 1.0V. The short wavelength peak from SLIP can be clearly distinguished under negative bias, hence the response under negative bias is more broadband than the positive one.

Figures 3(a) and (b) are the comparison of the responses under negative bias to those under positive bias at different bias magnitude. From Fig. 3(a), the photoresponse under positive bias from only quantum wells can be divided into two parts. The first part is the response at short wavelength side including a peak at 10.1 μm and a tail at shorter wavelength. The other part is the peak at 11.4 μm. Because the transition type of quantum wells is bound-to-continuum, we consider the short wavelength part is from the bound-to-continuum and the 11.4 μm peak is from bound-to-bound transition. For bias higher than 1.0V, as Fig. 3(b) shown, only the bound-to-bound peak can be observed.

For a bound-to-continuum QWIP, a broadband detector can also be achieved. However, the intensity of the short wavelength tail is relatively weak. Therefore, our perspective of broadband and flatband response can be achieved by adding the SLIP designed for short wavelength detection into the structure.

Under negative bias, the spectrum is the combination of the response from superlattice and quantum wells, and a new peak at short wavelength side from superlattice can be clearly distinguished when compared to spectrum under positive bias. For the response under 0.3V, the response under negative bias is more broadband than that under

positive bias. The additional spectrum located around 7 μm is from superlattice as our design and the other two peaks from quantum wells are just like the response under positive bias. As bias increases, the broadband response under negative bias can still be observed but less apparent. Since most of the sample structure is quantum wells, at high negative bias, only one peak from bound-to-bound transition in quantum wells exists like the response under positive bias. The above described photovoltaic and voltage-tunable characteristics can be observed until 80K.

The detectivity of our sample at three different temperature is shown in Fig.4. Here we choose two different wavelengths for the detectivity under positive and negative bias. For positive bias, the origin of response is quantum wells, so detectivity at 11.4 μm is shown. For low negative bias range, the response is mainly from the superlattice. Hence, the wavelength of the negative bias detectivity is chosen as 7.4 μm. From Fig.4, we observe the maximum detectivity occurred at low negative bias. At different temperature, the peak value of negative bias detectivity from superlattice is comparable to the detectivity from quantum wells even the bias at 2V. It is the evidence the superlattice suits for the low bias operation. Besides, this phenomenon is observed even at high temperature as 90K. Therefore, the superlattice is also ideal for high temperature operation.

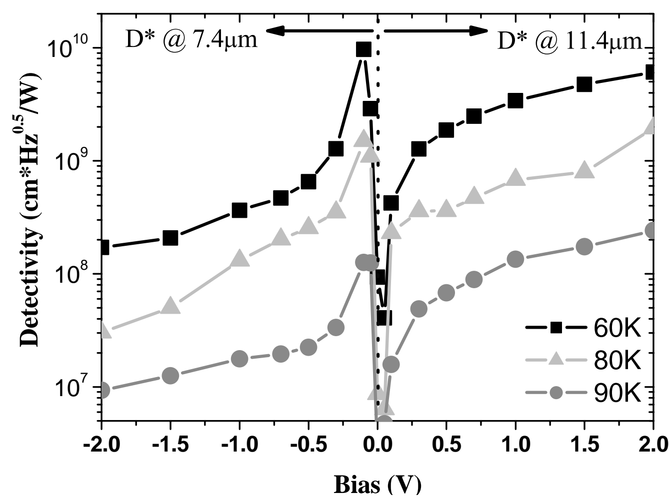

Fig. 4. The detectivity (D*) of our sample at 60K, 80K and 90K. The detectivity under positive and negative bias are at 11.4 and 7.4 μm, respectively.

4. Conclusion

In conclusion, a new structure of SLIP coupled to QWIP is investigated. By using this structure, the photovoltaic operation mode is achieved because the dopant migration effect in quantum wells and group velocity in superlattice. For photoconductive mode, only QWIP response exists at positive bias. Under low negative bias, the photoresponse from both SLIP and QWIP can be observed. By using this structure, under low bias range, the detector is not only with low dark current for lower power consumption but also the broadband and flatband photoresponse. This structure also makes the high temperature operation possible. Therefore, another choice is provided to implement the focal plane array.

References

[1] L. C. Lenchyshyn, H. C. Liu, M. Bunchanan and Z. R. Wasilewski, "Voltage-tuning in multi-color quantum well infrared photodetector stacks," *J. Appl. Phys.* **79**, 8091 (1996)

[2] K. L. Tsai, K. H. Chang, C. P. Lee, K. F. Huang, J. S. Tsang and H. R. Chen, "Two-color infrared photodetector using GaAs/AlGaAs and

strained InGaAs/AlGaAs multiquantum wells," *Appl. Phys. Lett.* **62**, 3504-3506 (1993)

[3] Yaohui Zhang, D. S. Jiang, J. B. Xia, L. Q. Cui, C. Y. Song, Z. Q. Zhou and W. K. Ge, "A voltage-controlled tunable two-color infrared photodetector using GaAs/AlAs/GaAlAs and GaAs/GaAlAs stacked multiquantum wells," *Appl. Phys. Lett.* **68**, 2114-2116 (1996)

[4] C. C. Chen, H. C. Chen, M. C. Hsu, W. H. Hsieh, C. H. Kuan, S. Y. Wang and C. P. Lee, "Performance and application of a superlattice infrared photodetector with a blocking barrier," *J. Appl. Phys.* **91**, 943-948 (2003)

[5] C. C. Chen, H. C. Chen, C. H. Kuan, S. D. Lin and C. P. Lee, "Multicolor infrared detection realized with two distinct superlattices separated by a blocking barrier," *Appl. Phys. Lett.* **80**, 2252-2254 (2002)

[6] J. H. Lu, Y. Y. Yang, C. C. Chen, C. H. Kuan, H. T. Chen and S. C. Lee, "Study of period number effect in the superlattice infrared photodetector," *Infra. Phys. & Technol.* **44**, 399-409 (2003)